Preparation and Electronic-Property Control of Low-Dimensional
Semiconductor Systems Using Methods of Interface Chemistry

界面化学的手法を用いた半導体低次元系の構築と
電子物性制御に関する研究

Tetsuya YAMAKI

Ph. D. Dissertation

Preparation and Electronic-Property Control of Low-Dimensional Semiconductor Systems Using Methods of Interface Chemistry

（和訳　界面化学的手法を用いた半導体低次元系の構築と
電子物性制御に関する研究）

Tetsuya YAMAKI
（八　巻　徹　也）

December, 1998

Department of Quantum Engineering and Systems Science,
Graduate School of Engineering,
The University of Tokyo

Acknowledgments

His thanks are due to all the members of "Ishigure-Katsumura" or "Ishigure" Laboratory and to the staffs of the executive office of the Department of Quantum Engineering and Systems Science, the University of Tokyo, for the completion of this thesis.

The author is very thankful to Ms. S. Hiratsuka, Mr. Y. Sugaya, Mr. T. Yakushiji, and Mr. M. Kawasome for encouraging him by having a heart-to-heart talk with him.

Finally, the author expresses special thanks to his parents who were patient enough to allow him to complete this thesis.

December, 1998

Tetsuya YAMAKI

Table of Contents

CHAPTER 1

Introduction

1.1. Aim and Concepts

Stimulated by the invention of the transistor in the early 1950s, the electronic properties of semiconductors have become research and engineering topics of high interest. The results of these investigations have led to an electronic revolution with numerous applications for all solid electronic devices, replacing the old technology based on vacuum tubes. An extraordinary large number of scientific studies deal with the semiconductor's electronic properties, all the way from basic physics to device application topics [1].

The recent development in semiconductors with the very exciting application potentials was to realize their artificially-made structures for optical and electronics purposes. These structures generally comprise the low-dimensional systems, which are on an intermediate scale between bulk crystals and small molecules, i.e., "mesoscale". In such low-dimensional systems, the quantum-mechanical wave functions of electrons and holes are confined inside the material, giving rise to the so-called *quantum-confinement effects*.

Especially in contemporary condensed-matter physics, much attention has been directed toward these low-dimensional materials. The purpose of the study

on low-dimensional systems is twofold: (i) the simplified description of several phenomena which take place in three-dimensional materials, and (ii) the discovery of novel phenomena peculiar to low-dimensional materials. These two purposes can be summarized as "a trend from three-dimensional to low-dimensional systems".

A challenge of modern materials science has made it possible to manufacture new low-dimensional materials with characteristics that are expected neither of the bulk nor of molecules. Actually, many techniques, such as lithographic, etching, and epitaxial processes, have been used for the fabrication of the nanostructures. These techniques reduce the three-dimensional structures into the realms of low-dimensions based on the above-mentioned physical aspect of the research. Such physical methods, on the whole, require not only intricate and expensive apparatus but also sophisticated skills by which their applications are limited.

In contrast to the traditional approach involving physical processing, advantages should be taken of the versatile inorganic, organic, and electrochemical synthetic methodologies in the chemical approach to construct low-dimensional structures. In this sense, this research area is interdisciplinary between physics and chemistry. So far, preparative, polymer, and colloid chemical techniques have been employed to control the size of the structures and to stabilize them in the solid state and in aqueous and nonaqueous dispersions [2,3]. All these methods can be regarded as "a trend from atoms or ions to new low-dimensional systems" in that they create artificial novel low-dimensional materials from their constituent elements.

The author also stresses that another viewpoint of chemical methodologies is of special importance in the present and future study of low-dimensional materials. This view suggests that a low-dimensional material is treated as a

constituting element for creating an artificial novel system by its rearrangement. Not only the characteristics of the low-dimensional elements themselves but also the global connection and networking among them play crucial roles in yielding a variety of phenomena of the constructed materials. Hence, the possibility for artificial control of such phenomena will be expected. This will also bring wide applications.

The present thesis focuses upon the utilization of "wet" chemical and colloid chemical methods for the preparation of these low-dimensional structures, followed by the controlled construction of organized assemblies containing these low-dimensional elements using molecular-handling techniques such as the Langmuir-Blodgett (LB) method. The films prepared by this method are known to offer the possibility of built-in architectural control at the monomolecular level. In addition, characteristics of the low-dimensional structures themselves and their assemblies should be clarified, then the author has a guiding principle for designing and synthesizing novel artificial materials with the appropriate and desired properties.

1.2.   Outline

In the above-mentioned concept, the author chose two different types of low-dimensional systems: polysilane polymers and semiconductor nanocrystals, which are artificial structures of organic and inorganic semiconductors, respectively. Using semiconductor physics terminology, the former are one-dimensional *quantum wires* and the latter are zero-dimensional *quantum dots*.

The present thesis consists of eight chapters, each of which is interrelated

but can be read individually without referring to the other chapters. Since low-dimensional materials often possess their own characteristic structures, there are a variety of properties unique to that material. Therefore, almost every chapter contains an introduction on the characteristic features of the low-dimensional material described therein.

In the first part of this thesis (Chapters 2 and 3), the author describes his study of a polysilane compound, which is one of the material systems currently being investigated. Chain-like polysilanes, consisting of a Si skeleton and organic substituents, are regarded as a soluble, σ-conjugating polymer model for *quantum wires* with a several angstrom wire width. Polysilane studies beginning around 1975, including the synthesis of homo- and co-polymers, the investigation of electronic structure in ground and excited states, the characterization of ultraviolet-visible (UV-Vis) absorption and emission spectroscopic properties originating from the polymer structure both in solution and in the solid state, together with the related photochemical phenomena and finally potential applications, are presently one of the most active fields in modern semiconductor science. At first, in Chapter 2, the author describes the synthesis of ammonium-type amphiphilic polysilanes, including their LB-film investigation. Interestingly, these silicon-based polymers can be prepared by organic chemistry methods, in this context, which is analogous to a conventional carbon-based one. Most materials treated in organic chemistry consist of many types of molecular species such as moieties or fragments in each molecule. It is expected, therefore, that the interaction among the species will become one of the controlling factors in such a material system. Chapter 3 describes the spectroscopic investigation of the molecular interaction in the polysilanes synthesized in Chapter 2. The author hopes that the present study will finally make it possible to arbitrarily modify or to improve the functions of

the polysilanes by controlling the molecular interaction. Thus, such a kind of study is quite important in the field of engineering, i.e., polysilane applications to electronics as well.

The second main part of this volume (Chapters 4-7) is devoted to the author's study of semiconductor *quantum dots*. Systematic research on the *quantum dots* began in the early 1980s with the identification of quantum confinement in small, nanocrystalline semiconductor inclusions in glasses and colloids, through the use of semiconductor-doped glasses as edge-filters or as Q-switches in lasers in much older. Since then, *quantum dots* have been very attractive and interesting objects for the scientific research of three-dimensionally confined systems. This simplest, naturally given zero-dimensional material is the ideal model system for the study of the basic questions of three-dimensional confinement in semiconductors. Beyond basic research, there is always the question of possible applications. Promising ideas exist regarding the fields of nonlinear optics (optical switching or modulating devices and laser diodes) and of physical chemistry (solar energy conversion, photocatalysis).

The quantum dots, referred here to as microcrystallites, microcrystals, quantum-sized particles, fine particles, nanoparticles, etc., of the II-VI or I-VII compounds can be grown in different matrices, such as glasses, solutions, polymers, or even the cavities of zeolites, and by different manufacturing processes, for example, by melting and annealing, by organometallic chemistry or by sol-gel techniques. In Chapter 4, the author, based on the above aspect of his own research, describes the preparation of cadmium sulfide (CdS) microcrystallites in LB films. The LB technique seems to be interesting as the methodology of nanocrystallite synthesis, because it provides highly anisotropic initial conditions. This chapter also gives information on the CdS microcrystal's real morphology, which was obtained by a new analysis of the film structure

based on Rutherford backscattering spectrometry. In Chapter 5, the author then continues to present the fabrication of microcrystallites of diluted magnetic semiconductors as a novel nanoparticle system. The method was slightly modified from that used for the preparation of the CdS microcrystals.

It is important to keep in mind that the smaller the particles are, the larger the portion of their constituent atoms are located at the surface. In semiconductor fine particles, this arrangement facilitates electron and/or hole transfers to and from acceptors and/or donors localized at their surface. It is becoming increasingly recognized that the properties of nanoparticles are strongly influenced by the physics and chemistry of their surface states as well as by their size and shape. In Chapter 6, the author uses an ion-irradiation technique to modify the surface states of the CdS fine particles. The technique presented has a significant applicability for the surface treatment of fine particles with the possibility of circumventing many constraints found in the conventional method. Chapter 7 then deals with a discussion concerning the nonlinear optical phenomena of nanoparticles. It is shown that the third-order susceptibility, $\chi^{(3)}$, which is a parameter to characterize the optical nonlinearity, of CdS nanoparticles is enhanced by surface modification.

The last chapter, Chapter 8, contains the concluding remarks. The author summarizes the results and suggests possible future directions.

In conclusion, this introductory chapter provided an outline of the fundamental concepts and ideas on which this thesis is based, including the rather limited prerequisites so that one can follow it and, finally, some hints about its contents.

REFERENCES

[1] For a textbook, see: N. Peyghambarian, S.W. Koch, and A. Mysyrowitz, *Introduction to Semiconductor Optics*; Prentice-Hall: New Jersey, 1993. See also the many references cited therein.

[2] G.A. Ozin, *Acc. Chem. Res.* **1997**, *30*, 17.

[3] P. Calvert and P. Rieke, *Chem. Mater.* **1996**, *8*, 1715.

CHAPTER 2

Synthesis of Amphiphilic Polysilanes Bearing a Pendant Ammonium Moiety for Preparing Langmuir-Blodgett Films

ABSTRACT

Five homologous amphiphilic polysilanes bearing an ammonium moiety in the side chain were synthesized. From the spreading behavior at the air-water interface, it was found that all the polysilanes provided stable monolayers on a water surface. These polysilane monolayers were readily transferred to hydrophilic substrates by applying the Langmuir-Blodgett (LB) technique. Anisotropy of the strong UV absorption due to the main-chain σ-conjugations, which was measured by polarized UV spectroscopy, revealed that the Si-Si backbone would align parallel to the dipping direction in the multilayered LB films.

2.1.　Introduction

In the past decade much attention has been directed toward linear polysilanes (polysilylenes), Si catenated polymers bearing two substituents at each Si unit, because of their characteristic optical and electronic properties [1]. For example, this new class of polymers exhibits large nonlinear optical effects, photodegradation, photoconduction, etc. These properties have been attributed to the extensive delocalization of the σ electrons, which is strongly influenced by the backbone conformations [1,2].

High-molecular-weight polysilane derivatives have been generally synthesized by the Wurtz coupling of the dichlorosilanes with sodium:

$$R^1R^2SiCl_2 + 2Na \rightarrow [R^1R^2Si]_n + 2NaCl \qquad (2.1)$$
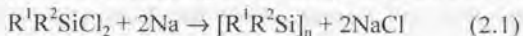
Various polysilanes have already been prepared by this reaction. However, the organic substituents on the Si have been largely restricted to two organic groups, alkyl and aromatic, because of the difficulties in achieving the polymerization [1]. Consequently, although a great deal of knowledge has been accumulated on polysilanes, these studies are limited in the three-dimensional state such as in solutions and in the bulk.

On the other hand, much recent effort has been devoted to the preparation of a monolayer at the air-water interface and Langmuir-Blodgett (LB) films of the preformed polymers. This effort could allow the study of a bidimensional molecular material and, therefore, provide a better understanding of the interchain packing and conformational states of the polymers. Such interfacial molecular handling gives structure-controlled films on the nanometer scale, and the molecular films obtained in this manner may have some features that deviate from the properties of the bulk materials. Based on these ideas, the application

of the LB technique to polysilanes is likely to be of both scientific and technological importance.

Suitable LB films can be formed either from amphiphilic polymers [3,4] or from polymers with rigid chains [5,6]. Especially, as for the former idea, the LB investigation of ordinary alkyl- and aryl-substituted polysilanes is very difficult due to the lack of hydrophilicity for interaction with a water surface. Nevertheless, as already mentioned, the following research groups carried out LB studies on chemically functionalized polysilanes.

Embs et al. [7] first reported LB work on polysilanes having bis(butoxyphenyl) substituents that generate stiff backbones to form a rodlike structure. With their polysilanes, the ether linkage was found to be essential for spreading as a monolayer on the water subphase. Due to the stiffness of these materials, highly oriented LB films were generated with their backbone aligned parallel to the dipping direction. Neher et al. [8] described the nonlinear optical properties (third-harmonic generation) of these highly oriented LB multilayers.

Hayase's group [9,10] synthesized polysilanes bearing a phenol group in the substituent that are well suited for LB film preparation. Introduction of the phenol moiety was achieved by protection with a trialkylsilyl group during the Wurtz-type condensation polymerization. Some of these polysilanes were found to form highly in-plane oriented LB films, and the orientational order was discussed on the basis of polarized fluorescence data [10,11]. More recently, hydroxyalkyl- and alkoxyalkyl-substituted polysilanes have been exploited [12], and the anisotropy of the thermochromism with regard to the dipping direction was observed in the LB films of a poly[bis(alkoxyalkyl)silane].

Brynda et al. [13] synthesized poly(methylphenylsilane) bearing σ-conjugated electron acceptor substituents and prepared LB films for investigating the electric and photoelectric properties of these substances.

Although the polysilanes did not seem to be fully spread as a monolayer on the water subphase, the utility of LB deposition for evaluation of the resistivity and photoconductivity at the metal/LB film contact region was demonstrated.

In this study, the author independently focused his efforts on LB investigations using polysilanes which bear ammonium substituents. This family of polymers is the representative example of a fully water-soluble charged polysilane first reported by Seki et al. [14,15]. Their preliminary experiments [14,15] revealed that the polysilanes with a long alkylammonium moiety formed stable monolayers on water and were readily transferred onto a solid substrate by the LB method. Another type of polysilane LB film could be prepared from a water-soluble polysilane that was ion-complexed with an arachidic acid monolayer at the air-water interface [16].

This chapter describes the detailed methodology for preparing the five ammonium-containing polysilane amphiphiles indicated in Chart 2.1 (**PS1–PS5**). In addition, the author reports herein his expanded investigation, presenting the results of an LB study using some of the above polymers. The spectroscopic properties of these samples (in solution or films) will be critically discussed in the next chapter.

2.2.   Experimental Section

2.2.1.   Materials

The silane monomers of methylphenyldichlorosilane and methyl(β-phenethyl)dichlorosilane for **PS1–PS3** and **PS5** were purchased from the Shin-

$$CH_2-N^{\oplus}\begin{matrix}CH_3\\|\\|\\CH_3\end{matrix}C_mH_{2m+1}\quad Cl^{\ominus}$$

$(CH_2)_y$

$\left(\!-\!Si\!-\!\right)_n$

CH_3
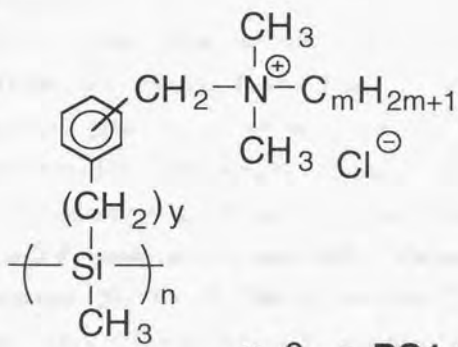
y=0 → **PS1 (m=8)**
PS2 (m=10)
PS3 (m=14)

y=1 → **PS4 (m=14)**
y=2 → **PS5 (m=14)**

Chart 2.1. List of structures and abbreviations of the polysilanes prepared in this study.

Etsu Chemical Co., Ltd. and distilled before use. Anhydrous tin(II) chloride and all tertiary amines were obtained from the Wako Pure Chemical Co. and Tokyo Kasei Kogyo Co., respectively, and were used without purification. Chloromethyl methyl ether was obtained from the Tokyo Kasei Kogyo Co. and used after distillation.

For the synthesis of **PS4**, the methylbenzyldichlorosilane monomer was prepared by the following route. Benzyl chloride (77.8 g, 0.615 mol) was mixed with magnesium grain (16 g, 0.66 mol) in diethyl ether to provide benzyl magnesium chloride. This Grignard reagent was added dropwise to methyltrichlorosilane (80 g, 0.54 mol) dissolved in 240 mL of benzene. After evaporation of the diethyl ether at about 100 °C, the residue was distilled under reduced pressure (200 °C). ^{1}H NMR (CDCl$_3$): δ 0.72 (singlet, 3H, Si–CH$_3$), 2.67 (singlet, 2H, Si–CH$_2$–Ar), 7.13–7.29 (multiplet, 5H, Ar–H).

2.2.2. Preparation of Amphiphilic Polysilanes

As shown in Scheme 2.1, the ammonium-containing amphiphilic polysilanes were prepared according to the procedure adopted by Seki et al. [14]. Note that this scheme represents only the essence of the reaction. The starting polysilanes were obtained by the conventional Wurtz-type coupling [1,17]. The phenyl group was chloromethylated and then quaternized with a tertiary trialkylamine in tetrahydrofuran at refluxing temperature. The synthesis was performed under dim red light or in the dark. The detailed procedures are described below.

Wurtz-Type Condensation

Sodium condensation for the synthesis of the prepolymer was essentially
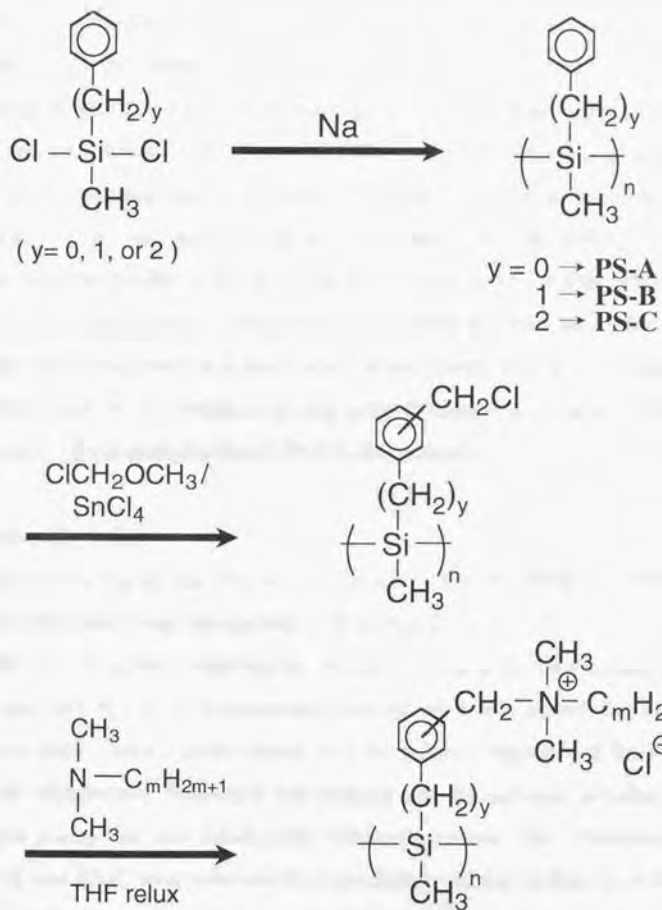
Scheme 2.1. Syntheses of amphiphilic polysilanes with ammonium moieties.

performed according to the procedure of Rabolt et al. [17]. Methylphenyldichlorosilane (0.078 mol) and dispersed sodium (more than twice the amount of the silane monomer) were refluxed in undecane for about 2 h. The reaction mixture was poured into 2-propanol. The resulting precipitate was dissolved in toluene, washed twice with water, and dried over anhydrous MgSO₄. The polymer was reprecipitated by pouring this toluene solution into 2-propanol. The precipitate was dried under reduced pressure to yield poly(methylphenylsilane) (**PS-A**) as the starting polysilane of **PS1–PS3**.

For the other polymers, the precursors of **PS4** and **PS5**, the polymerization reaction was performed in toluene and toluene/diethylene glycol diethyl ether (diglyme) (80/20 by volume), giving poly(methylbenzylsilane) (**PS-B**) and poly[methyl(β-phenethyl)silane] (**PS-C**), respectively.

Chloromethylation

The phenyl group of the starting polysilanes (**PS-A**, **PS-B**, and **PS-C**) was chloromethylated using the method of Ban et al. [18].

PS-A (3.5 g) was dissolved in 30 mL of chloroform and cooled in an ice bath, and then 30 mL of chloromethyl methyl ether was added. SnCl₄ (about 1 mL) was slowly added under argon, and the solution was stirred for 15-20 h at ice-bath temperature. Methanol was poured into the polymer solution, and the obtained precipitate was dried under reduced pressure. The chloromethylation of **PS-B** and **PS-C** was achieved by a procedure similar to that used for **PS-A**. In the ¹H-NMR spectrum, the chloromethylene protons showed a broad peak at 4.2-4.7 ppm. As is commonly accepted, chloromethylation predominantly occurs at the para or ortho positions of the phenyl groups by the Friedel-Crafts reaction. In this case, however, it appears that there is just not enough room at the ortho positions, where crowding increases close to the main chain of the

polymer, for appreciable substitution to occur there. Due to such steric reasons, most of the chloromethyl groups are thought to be attached at the para position.

Quarternization with Tertiary Amines

Chloromethylated polysilanes were successively reacted with tertiary amines in refluxing tetrahydrofuran for 15-20 h to provide amphiphilic polysilanes. When the polymer started to precipitate during the reaction, a small portion of ethanol was added to maintain a homogeneous solution. The final products were purified by precipitation from tetrahydrofuran in n-hexane or acetone. In particular, the quaternization reaction of the **PS-A** was performed using N,N-dimethylalkylamine whose long-chain alkyl group varied from octyl- (m = 8) to tetradecyl- (m = 14) to yield the polysilanes of **PS1–PS3**.

2.2.3.   Methods and Characterization

LB Film Preparation

The amphiphilic polysilanes were spread under dimmed red light from freshly prepared chloroform solutions (ca. 1×10^{-3} unit mol dm^{-3}) on a Lauda FW-1-M film balance. The author employed pure water as the subphase which was doubly distilled and then passed through a Milli-Q system. After the solvent evaporated, the monolayer was compressed at the given speed and the surface pressure was recorded versus the area per Si unit at 19-21 °C. For the LB deposition, the monolayer compressed to 30 mNm^{-1} was transferred onto a quartz glass plate (9 mm $\times$ 39 mm; dipping along the longer side) using the vertical dipping technique at a dipping speed of 3.0-3.5 cm min^{-1} for both the

up and down strokes.

Spectroscopy

^{1}H nuclear magnetic resonance (NMR) spectra were measured with a JEOL EX-270 operating at 270 MHz in CDCl$_3$. Chemical shifts are reported in ppm (δ) relative to tetramethylsilane as the internal reference.

UV-Vis spectra were recorded at room temperature with a Hitachi U-3200 spectrophotometer. All measurements were made in the transmission mode using chloroform solutions (1×10^{-4} unit mol dm^{-3}) and LB films. The LB-coated plates were secured in a metal holder which fit into a 1-cm path length UV-Vis absorbance cell. The incident beam was polarized with a polarizer for the dichroism experiments on the LB films.

Polymer Characterization

The molecular weights of the starting and chloromethylated polysilanes in tetrahydrofuran were estimated by gel permeation chromatography (GPC) (polystyrene standard) using a Shimadzu LC-6A chromatograph equipped with two columns of TSK Gel from Toyo Soda Co.; GPC measurements on the final amphiphilic polysilanes were made using a TOSOH HLC-8120 chromatograph with N,N-dimethylformamide as the eluent. Elemental analyses were performed on a Perkin-Elmer 240C analyzer at the Institute of Scientific and Industrial Research, Osaka University.

2.3.   Results and Discussion

2.3.1.   Polymer Syntheses

In the polymerization procedure, all monomers produced the polysilanes having a weight-averaged molecular weight (M_W) of nearly 10^5 or above in satisfactory yields. The final polymers derived from these parent polysilanes did not show any decrease in the molecular weight: M_W exceeded 2.7×10^5 in all cases. In order to identify the polymers as being polysilanes, the UV-Vis absorption spectra were obtained for **PS1–PS5** in chloroform solutions. The representative spectrum of **PS3** is shown in Figure 2.1. For all the polysilanes, an intense band assigned to the σ–σ* transition of the conjugated Si-Si backbone [1] was observed at 300-330 nm. This spectral profile was almost the same as that of the corresponding starting polymer.

In the previous study of Seki et al. [19], the chloromethylation of **PS-A** was performed under relatively mild conditions compared to that of the other polysilanes because, for the aryl-substituted polysilane, the phenyl group is readily replaced by chlorine in the presence of a Lewis acid [1b]. This side reaction should lead to a significant decrease in the molecular weight and modulation of the absorption spectra. However, from the above-mentioned properties of the final polysilanes, the author considers that his experimental conditions were too mild to induce such an unfavorable replacement reaction.

The elemental analysis data are as follows: Calculated for $[C_{24}H_{44}NSiCl]_n$ (**PS3**): C, 70.31; H, 10.74; N, 3.42. Found: C, 68.33; H, 10.88; N, 3.21. Calculated for $[C_{25}H_{46}NSiCl]_n$ (**PS4**): C, 70.82; H, 10.86; N, 3.31. Found: C, 68.16; H, 10.92; N, 3.08. Calculated for $[C_{26}H_{48}NSiCl]_n$ (**PS5**): C, 71.30; H, 10.97; N, 3.20. Found: C, 69.78; H, 9.61; N, 1.66. From these data, the
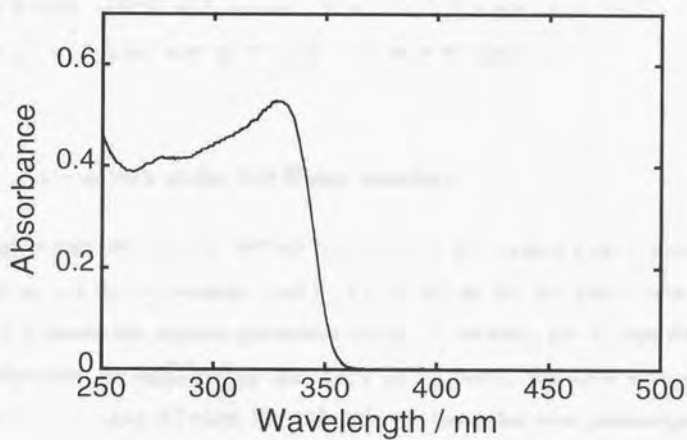
Figure 2.1. UV-Vis absorption spectrum of **PS3** in chloroform at a concentration of 1×10^{-4} unit mol dm^{-3}.

introduction ratios of the long alkylammonium group can be estimated to be 82, 81, and 27%, respectively. These estimations are based on the assumption that all the chloromethyl groups on the phenyl groups have reacted with the tertiary amines as reported in previous papers [14,19]. There is nothing to account for the decrease in reactivity for **PS5** at the present time.

The polysilanes with ammonium groups were soluble in hydrophilic solvents such as alcohols. They were almost insoluble in hydrophobic solvents such as hexane, xylene, and toluene. These solubilities are completely opposite to those of polysilanes bearing only alkyl and aromatic groups.

2.3.2.   Monolayers at the Air-Water Interface

The relationship between the surface pressure and the surface area determines whether or not the polysilanes make monolayers at the air-water interface. Figure 2.2 shows the surface pressure-area (π-A) isotherm per Si unit for the **PS3** polysilane. As indicated by the shape of the curve, the surface pressure increased and leveled off when the molecules on the water were pressurized. It has been believed that molecules provide monolayers on the air-water interface in the region between the point where the surface pressure begins to appear and the point where the surface pressure levels off (onset of collapse). The isotherm indicates that **PS3** would form a stable L film (monolayer at the air-water interface). It is worth mentioning that irreversible compression-expansion behavior was seen in that region. Essentially, the same behavior was observed for the other polysilanes.

The limiting area per Si unit, by extrapolation of the steepest region to zero surface pressure for the polysilane (about 0.45 nm^2), was larger for the cross-
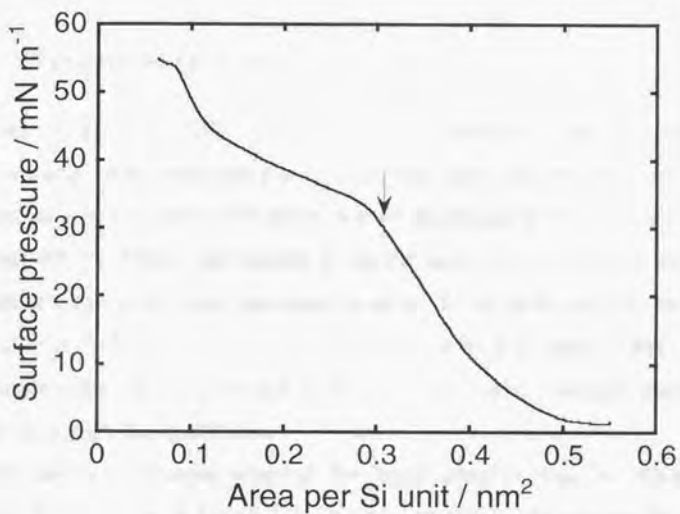
Figure 2.2. Surface pressure-area isotherm per Si unit of **PS3** on pure water. The arrow refers to the transfer condition of sample preparation for spectroscopic measurements shown in Figures 2.3 to 2.5.

section of a vertically oriented long alkyl chain (0.2 nm^2). This suggests that the molecular dimension of the condensed surface monolayers is determined by the bulky part around the Si unit and that the long alkyl chains of the monolayer are in the air phase and loosely packed.

2.3.3. Transferred LB Films

Polymers that provide stable L films (monolayers at the air-water interface) do not necessarily yield multilayer films. If the monolayer can be deposited onto a substrate step by step, the σ−σ* absorption of the prepared film should linearly increase with the deposition number. From the inset of Figure 2.3, it becomes apparent that the multilayers composed of up to 201 monolayers were obtained in the case of **PS3**. Actually, the transfer ratios defined as (area of transferred polysilanes onto plate)/(decreased area on the air-water interface) were high enough to prepare the specimens.

The surface pressure selected for layer transfer was 30 mNm^{-1} as indicated by the arrow in Figure 2.2. This corresponds to the area per Si unit of 0.32 nm^2. The UV spectrum recorded from 201 monolayers of **PS3** on each side of a substrate (that is, a total of 402 layers) is depicted in Figure 2.3. The spectrum shows the same absorption bands as polysilanes in solution without any shift (compare to Figure 2.1). The LB films of **PS4** are similar to those of **PS1**–**PS3**. These data suggest the important conclusion that a deposited film on the solid substrate maintains the polymer conformation in solution. In contrast, the conjugated backbone absorbance for **PS5** exhibited a slight blue-shift (approximately 10 nm) from the solution (result not shown). Seki et al. [15,19] reported that the spectral change for such a methyl[β-phenethyl]silane-based
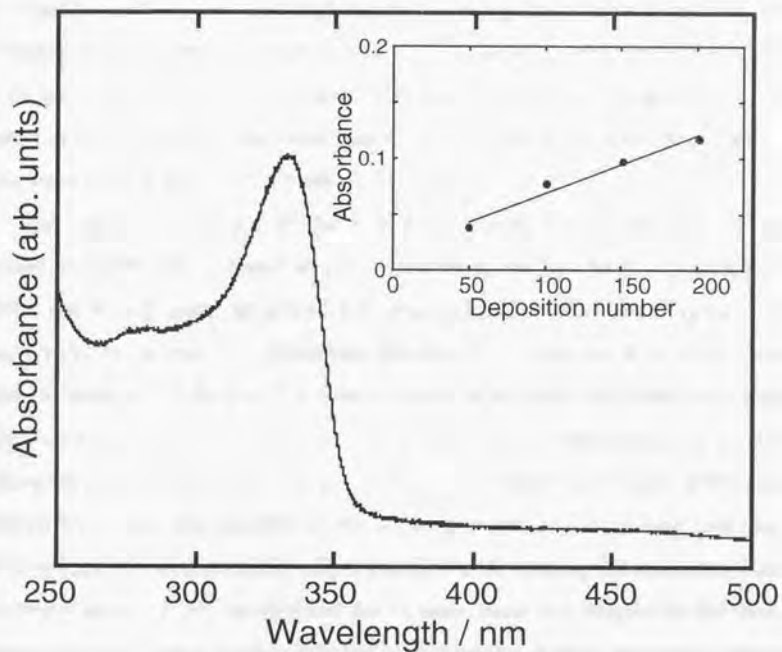
Figure 2.3. UV-Vis absorption spectrum of transferred monolayers of **PS3** on both sides of a quartz substrate (deposition number: 201). Transfer condition is indicated by arrows in Figure 2.2. Inset: Absorbance of the σ–$\sigma*$ transition at 330 nm as a function of the deposition number.

material was sensitive to the magnitude of the pressure applied for LB deposition, and also regarded the spectral shift as an example of the piezochromic effect. According to their reports, the blue-shift should be attributed to conformational changes in the σ-conjugated Si backbone from an expanded state, namely, enhancement of the gauche conformer in the Si backbone. This difference between **PS5** and the other polysilanes may be related to the stiffness in the main chain of each polymer, which stems from steric interference of the substituents [20].

The transition moment of the first σ–σ* band around 300-330 nm is parallel to the Si chain direction [21]. Therefore, the Si chain orientation is readily estimated using polarized UV absorption spectroscopy. Figure 2.4 displays the polarized UV absorption spectra of 151-layered **PS3** deposited under the present conditions. The electric vector of the polarized light in normal incidence was set parallel (solid curve) and perpendicular (dashed curve) to the dipping direction. The absorptivity of the σ–σ* band was larger when the polarization plane was parallel to the dipping direction, indicating that the polymer backbone preferentially aligns parallel to the dipping the direction. The previous studies [15,19] clarified that the Si main chain was aligned by the flow orientation on the water surface induced by successive dipping processes rather than by flow on the substrate.

The dichroic ratio R defined as A(parallel)/A(perpendicular), where A(parallel) and A(perpendicular) represent the absorbance parallel or perpendicular to the dipping direction, respectively, was rather small (ca. 1.1). This R value was comparable to that obtained by Seki et al. [19]. As already introduced, some of the other polysilane LB films reported by both Embs et al. [7] and Kani et al. [8,10] are highly oriented in the dipping direction. Such LB films have a dichroic ratio of more than 3. The author assumes that the high
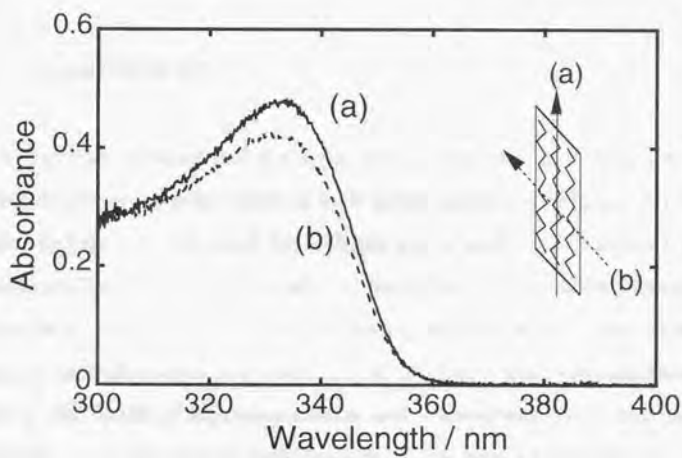
Figure 2.4. Polarized absorption spectra of a 151-layered LB film of **PS3** on both sides of a quartz substrate. Absorption spectra were taken in normal incidence with linearly polarized light set parallel (a, solid line) and perpendicular (b, dashed line) to the dipping direction.

flexibility and lack of stereoregularity for the present polysilanes may be responsible for the rather poor orientation. In fact, Seki et al. [22] demonstrated that introduction of the bulky and symmetrical dihexylsilane component improved the orientational order.

2.4. Conclusions

This chapter demonstrated that it was possible to introduce ammonium moieties into the side chains of polysilanes as hydrophilic groups. Stable monolayers on the water surface were obtained for all these polysilanes. Application of the LB technique for the polysilanes was able to modulate the molecular arrangement which cannot be attained by a simple casting method. Also, it provided very homogeneous multilayered polysilane ultrathin films. These materials may be of interest in the fields of microelectronics and microoptics. As a first step for such applications, the author will describe in the next chapter the molecular interactions in the diluted solutions and in the thin films of the polysilanes based on their detailed spectroscopic measurements. Both the intra- and inter-molecular interactions determine the relaxation process of the excited chromophores, whose study will bring new breakthroughs in understanding the mechanism of the unique functions exhibited by polysilanes. The possibility for precise control of these interactions will also be described.

REFERENCES

[1] For reviews, see: (a) R.D. Miller and J. Michl, *Chem. Rev.* **1989**, *89*, 1359. (b) R.J. West, *Organomet. Chem.* **1988**, *300*, 327. See also references cited therein.

[2] R.D. Miller, *Angew Chem., Int. Ed. Engl., Adv. Mater.* **1989**, *28*, 1733.

[3] Y. Nishikata, Y. Morikawa, Y. Takiguchi, M. Kanemoto, M. Kakimoto, and Y. Imai, *Jpn. J. Appl. Phys.* **1988**, *27*, L1163.

[4] Y. Nishikata, Y. Morikawa, Y. Takiguchi, M. Kanemoto, M. Kakimoto, and Y. Imai, *Nippon Kagaku Kaishi* **1987**, 2174.

[5] G. Duda, A.J. Schouten, T. Arndt, G. Lieser, G.F. Schmidt, C. Bubeck, and G. Wegner, *Thin Solid Films* **1988**, *195*, 221.

[6] G. Duda and G. Wegner, *Makromol. Chem., Rapid Commun.* **1988**, *9*, 495.

[7] F.W. Embs, G. Wegner, D. Neher, P. Albouy, R.D. Miller, C.G. Willson, and W. Schrepp, *Macromolecules* **1991**, *24*, 5068.

[8] S. Mittler-Neher, D. Neher, G.I. Stegeman, F.W. Embs, and G. Wegner, *Chem. Phys.* **1992**, *161*, 289.

[9] Y. Nakano, S. Murai, R. Kani, and S. Hayase, *J. Polym. Sci., Part A: Polym. Chem.* **1993**, *31*, 3361.

[10] R. Kani, H. Yoshida, Y. Nakano, S. Murai, Y. Mori, Y. Kawata, and S. Hayase, *Langmuir* **1993**, *9*, 3045.

[11] H. Yoshida, R. Kani, S. Hayase, and K. Horie, *J. Phys. Chem.* **1993**, *97*, 5370.

[12] R. Kani, Y. Nakano, Y. Majima, S. Hayase, C. -H. Yuan, and R. West, *Macromolecules* **1994**, *27*, 1911.

[13] E. Brynda, I. Koropecky, I. Kminek, S. Nespurek, and W. Schnabel, *Polym. Adv. Technol.* **1994**, *5*, 257.

[14] T. Seki, T. Tamaki, and K. Ueno, *Macromolecules* **1992**, *25*, 3825.

[15] T. Seki, T. Tamaki, K. Ueno, and Y. Tanaka, *Thin Solid Films* **1994**, *243*, 625.

[16] T. Seki, A. Tohnai, T. Tamaki, and K. Ueno, *J. Chem. Soc., Chem. Commun.* **1993**, 1876.

[17] J.H. Rabolt, D. Hofer, R.D. Miller, and G.N. Fickes, *Macromolecules* **1986**, *19*, 611.

[18] H. Ban, D. Sukegawa, and S. Tagawa, *Macromolecules* **1987**, *20*, 1775.

[19] T. Seki, N. Tanigaki, K. Yase, A. Kaito, T. Tamaki, K. Ueno, and Y. Tanaka, *Macromolecules* **1995**, *28*, 5609.

[20] L.A. Harrah and J.M. Zeigler, *Macromolecules* **1987**, *20*, 601.

[21] H. Tachibana, Y. Kawabata, S. Koshihara, T. Arima, Y. Moritomo, and Y. Tokura, *Phys. Rev. B* **1991**, *44*, 5487.

[22] T. Seki, T. Tamaki, K. Ueno, and Y. Tanaka, *J. Photopolym. Sci. Technol.* **1993**, *6*, 113.

CHAPTER 3

Control of Molecular Interactions in Ammonium-Type Amphiphilic Polysilanes for Application to Electronics

ABSTRACT

Molecular interactions in five amphiphilic polysilanes bearing an ammonium moiety in the side substituent and the possibility of their control were investigated. From the results of detailed spectroscopic measurements of the polymer solutions, the fairly broad emission at 400-500 nm, observed for some of these polysilanes for the first time, was ascribed to the intramolecular exciplex formation between the Si-conjugated backbone and ammonium site. The main- and side-chain orientations were predicted from a conformational energy calculation. The nearest distance between the chromophores was estimated to be 6.9 Å. Assuming a direct charge-transfer (CT) model, the process involving the exciplex emission should be regulated by the different distances between the pair. In contrast to the normal case of the exciplex, the present system showed a very small effect of solvents with different polarities on the emission, possibly due to the peculiarity that the σ-delocalized state of

the backbone is involved in the exciplex formation. Importantly, behavior of the photo-generated holes in the Si backbone seemed to be affected by the CT interaction during the excited-state process. In addition, polysilane films prepared by a solvent casting method showed another emission band at a longer wavelength (around 560 nm). This band was not observed for the LB films where the molecules were oriented parallel to the dipping direction and so the possibility that it originates from an intermolecular interaction was considered.

3.1.   Introduction

Polysilanes are considered as one-dimensional molecular wires based on the σ-conjugation in the Si-Si backbones, the backbone being the wire, the organic side group acting as the insulator [1]. Their generally excellent thermal and mechanical properties, coupled with the unusual electronic characteristics and photolability, have led to many potentially interesting applications. The first of these to be commercially exploited was the use of polysilanes as thermal ceramic precursors [2]. This was soon followed by applications that exploited the photolability of the polysilane derivatives for the photoionization of vinyl polymerization [3,4] and in many imaging (i.e., lithographic) applications [5,6]. The curious electronic properties of the polysilanes have also attracted attention in areas such as electrical conduction [7] and photoconduction [8,9] and, most recently, as new materials with interesting nonlinear optical characteristics [10]. In this last area, it is anticipated that their capacity for high-resolution imaging coupled with their unusual optical properties is a unique combination with much utility.

Such potential applicabilities originate from the unusual σ-electron nature of the electronic excitations in polysilanes. According to many studies on a more fundamental level [1,11], the dynamics of the excitation is governed by an interesting and complex interplay among energy transfer, fluorescence, photochemistry, and other deactivation routes. Also, on the basis of spectroscopic and photochemical measurements (vide infra), a chromophoric segmental model has been proposed for the polysilane chain both in solution and in the solid state. This model suggested that the polysilane chain consisted of a series of approximately planar all-trans segments separated by one or more conformational twists or kinks in the backbone. The nonhomogeneous distribution of the chromophoric segments containing 20-30 silicon units, their spectroscopic properties, and their energy transfer processes are then assumed to dictate the optical properties of the polysilane high polymers. Thus, almost all the above-mentioned unique properties of the polysilanes could be interpreted in terms of a similar picture. For example, previous measurements of the temperature dependence of carrier mobility suggested that the photocurrent was conducted via a hopping transport from one segment to another [12].

Each chromophoric segment in the polysilanes can be regarded as a higher-order structure of the polymer, which is very familiar in protein chemistry. In this sense, the characteristics of the electronically excited states of these chromophores depend on both their intrinsic chemical makeup and the environment in which they are placed. Accordingly, it is fully expected that the processes occurring between different segments be basically determined by the nature of the molecular interactions especially in the excited state. In general, the behavior of molecules in the excited state significantly differs from that in the ground state and so their interaction might bring about a variety of new and interesting phenomena, e.g., the charge transfer or separation, thereby the

induced formation of excited complexes or their deactivation, and some photosensitized reactions. Consequently, these phenomena have recently been used to study the macro- and micro-environments in polymers [13]. Emission measurements are quite suitable for this type of study.

It is accepted that the molecular interactions can involve two kinds of processes. The first is the *intramolecular* route in which the polymer coil achieves a configuration that happens to place one part in a reasonable location from another. The second is the *intermolecular* route occurring between different molecules. In principle, of course, the relative importance of these mechanisms could be assessed by dilution or concentration studies. In the present study, the author treats both kinds of interactions using the five polysilanes synthesized in Chapter 2, and then controls them in the following two ways:

(i) The ammonium-type amphiphilic polysilanes obtained possess various side-chain structures. Thus, one could envision the appearance of different intramolecular interactions in these polymers. As expected from their structures (shown in Chart 2.1), the difference may be related either to the ammonium group with different lengths of the long alkyl chain or to the methylene(s) between a Si atom and a phenyl moiety.

(ii) The LB method is one of the techniques employed for the preparation of orderly molecular assemblies. The use of this method for polysilanes would enable the molecules to be "statically" fixed at specific locations (see Chapter 2). Therefore, it may be possible for intermolecular interactions in the films to be controlled by molecular handling.

The author hopes that this work will make it possible to arbitrarily modify

the intriguing electronic properties of polysilanes (mentioned above) by the precise control of the molecular interactions. In this respect, the present chapter also provides, as a first step, an attempt to control the behavior of the photo-generated holes through a variety of the excited-state interactions based on the different chemical structures.

Concerning the amphiphilic polysilanes with ammonium moieties employed here, Seki et al. [14-17] revealed their spectroscopic properties both in solutions and in LB films to some extent. Nevertheless, the characteristics of the excited states, including the relaxation processes, in these polysilanes have not been clarified so far. The present chapter describes, for the first time, the observation of the emission from excited complexes formed in some of the obtained polymers.

3.2. Experimental Section

Synthesis of the ammonium-containing amphiphilic polysilanes (PS1–PS5) and film preparation were carried out in a manner similar to that used by Seki et al. [14]. The details were mentioned in Chapter 2.

Spectrometric measurements were made in organic solvents (1×10^{-4} unit mol dm^{-3}) and in the solid films at room temperature. All solvents (chloroform, carbon tetrachloride, chlorobenzene, dichloromethane, and 1,2-dichloroethane), being transparent down to 250 nm, were used as received. For film samples, the author observed emissions induced by high-energy-ion-beam bombardment. This measurement has an advantage that huge energy can be easily deposited before decomposition of the Si main chain. As a substrate, the author adopted

Si which is irradiation resistant up to very high doses without any detectable formation of radiative species in the measured wavelength range of the emission spectra. Optical UV-Vis absorption and emission spectra were recorded using a Hitachi U-3200 and F-3000 spectrometers, respectively. For the emission spectroscopy, Ar gas was bubbled through the sample solution at least 10 min. before the measurement. Excitation at 300 nm was carried out using a 150-W Xe lamp.

The samples in a vacuum chamber ($< 10^{-5}$ Pa) were irradiated by 2 MeV H^+ from a single-ended Van de Graaff accelerator of the Research Center for Nuclear Science and Technology, the University of Tokyo. The system for detection of the ion-beam-induced emission is schematically shown in Figure 3.1. There was a computer-controlled beam shutter in front of the vacuum chamber and this beam shutter was charged by a high voltage generator (150 ~ 700 V). Therefore, electrons scattered from the shutter hit by the ion beam were accelerated in the electric field. Observing this scattered electron current enabled one to monitor the beam stability during irradiation. The emission from samples was delivered from the chamber to the detection device by glass fibers.

The detection device was an optical multichannel analysis (OMA) USP-600 system produced by Unisoku Corp., and this system was suitable for the detection of photons from 200 to 850 nm. In-situ observation of the emission spectra was carried out in two steps. First, a sample was irradiated by ion beams for 10 s while the OMA system simultaneously collected the emitted photons. Next, the beam shutter was inserted in the path of the beam trajectory, and the beam current and blank signal from the photodiode array of the OMA system were measured during the 10 s of irradiation. Specifically, one cycle was 20 s, and an unlimited number of cycles was repeated. Through all the experiments presented here, the beam current was 1-10 nA and the beam spot
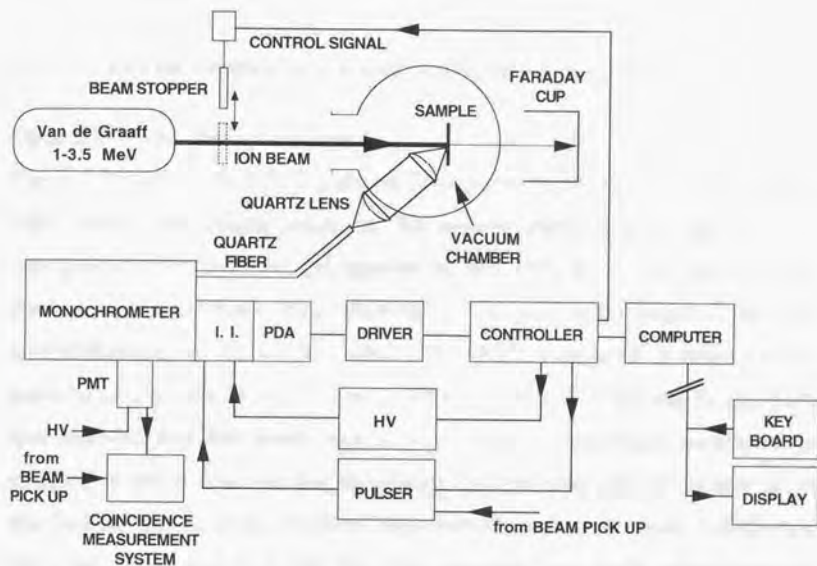
Figure 3.1. Schematic representation of the in-situ observation set-up geometry of the ion-induced emission spectra.

was about 5 mm in diameter.

3.3.   Results and Discussion

3.3.1.   Intramolecular Interaction in Organic Solutions

Optical UV-Vis Absorption Spectra

Figure 3.2 displays the UV-Vis absorption spectra of all the polysilanes (**PS1–PS5**) in the chloroform solutions. An intense band originating from the conjugated Si-Si backbone [1] appears at 300-330 nm. The position of the absorption maximum was shifted to longer wavelengths for the methylphenylsilane-based polymers (**PS1–PS3**) compared to those for the polysilanes from the other monomers (**PS4** and **PS5**). Harrah and Zeigler [18] demonstrated that the wavelength of the Si band absorption maximum in solution is dependent on the dimensions of the two organic substituents attached to the Si atom; bulkier substituents lead to a more red-shifted spectrum. They suggested that the shift stemmed from steric interference of the substituents which resulted in straining the Si backbone conformational preference. According to their observations and interpretation, the bathochromic shifts exhibited in **PS1–PS3** should be attributed to the bulkiness of the aromatic group on Si, thereby enhancing the trans/gauche ratio in the backbone conformation.

The ionization potential of polysilanes is known to be lower than that of carbon-based polymers, because the σ bond in the former polymers is formed by overlap of the $3sp^3$ hybrid orbitals whereas the latter by lower-energy $2sp^3$
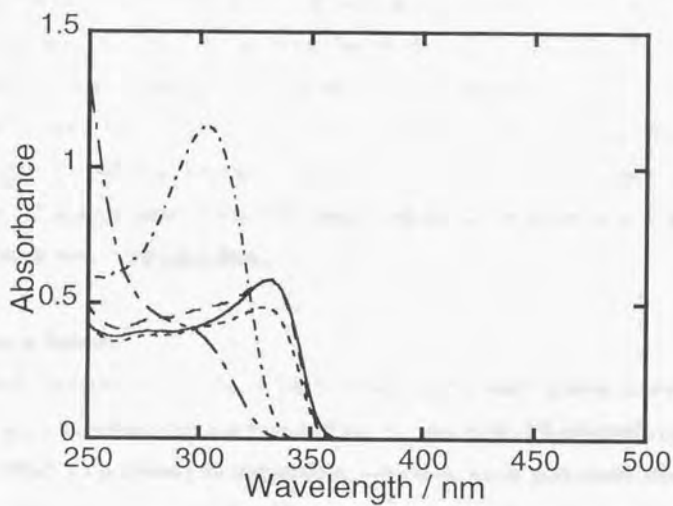
Figure 3.2. UV-Vis absorption spectra of **PS1** (——), **PS2** (- - -), **PS3** (— —),
PS4 (- ——), and **PS5** (—·—) in chloroform solution (ca. 1×10^{-4} unit mol dm^{-3}).

hybrids. In this regard, it has been expected that the Si-Si backbone acts as an electron-donor and involves charge-transfer (CT) interactions with certain electron-acceptors. In fact, Kira et al. [19] found intramolecular CT interactions in origosilane compounds, where silanyl donors are separated from dicyanoethylene acceptors by two ethylene groups. Additionally, Traven et al. [20] and Sakurai et al. [21] reported that σ electrons of Si-Si bands could be donated to certain π-acceptor molecules such as tetracyanoethylene (TCNE). In all these cases, the CT interaction was accompanied by the weak absorption below the $\sigma - \sigma*$ band. However, this is not the case with the present system; Figure 3.2 did not exhibit any CT bands, indicating the absence of a ground-state interaction in the polysilane.

Emission Spectra

Figure 3.3 presents the emission spectra observed for methylphenylsilane-based (**PS3**, a), methylbenzylsilane-based (**PS4**, b), and methyl[β-phenethyl]silane-based (**PS5**, c) polymers in chloroform solutions. Each polysilane examined here has a C_{14} alkyl chain in the side ammonium group. These spectra displayed an intense and sharp emission band centered at 325-355 nm (with small Stokes shifts, about 0.3 eV), which is due to a $\sigma* \rightarrow \sigma$ transition of the Si backbone [1]. The longer-wavelength shift of the emission observed for **PS3** is in good accordance with the bathochromic shift of the UV absorption.

Strikingly, another broad emission band around 400-500 nm was observed only for **PS3**. This broad band is in contrast to the sharp fluorescence arising from the backbone delocalized state as cited in the above paragraph. Generally, linear polysilane derivatives never show a visible emission like this except for a weak and broad phosphorescence or an impurity band only in rigid media (below 77 K) [18,22].
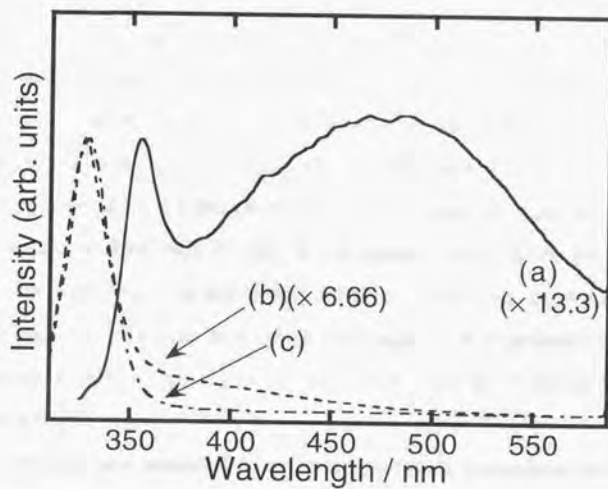
Figure 3.3. Emission spectra of methylphenylsilane-based **PS3** (a), methylbenzylsilane-based **PS4** (b) and methyl[β-phenethyl]silane-based **PS5** (c) polymers in chloroform solution (ca. 1×10^{-4} unit mol dm^{-3}). The excitation wavelength was 300 nm.

It is quite natural that the intermolecular interaction be negligible in the diluted solution system where molecules are supposed to be isolated from each other. Thus, it seems probable that an intramolecular interaction can be responsible for such a new emission. This can also be predicted by the previous report demonstrating that the polysilanes exhibited an absorption band due to an intramolecular CT interaction when cationic moieties, such as ammonium and pyridinium ones, were introduced into the side substituent [23]. However, the interaction involved in the present case should be different from that found in that report, in that it exists only in the excited state as shown by the absorption spectra (Figure 3.2). In all the cases the author examined, the exciting light (300 nm) was absorbed only by the Si conjugated main chain. Based on this point, one may conclude that the visible emission involves a species including a polysilane backbone state (σ) as a component and that it is probably an excited-state complex. It seems unlikely, however, that the species could be an excimer in the present case.

If an excited-state complex is being formed here, consideration should be then given to the existence of an exciplex. Many observations of exciplex formation have been reported, and the best-characterized case involving ground-state lone pair donors (such as amines, nitriles, and others) and excited-state π acceptors was discussed by Mataga et al. [24,25]. One of the main purposes of this study was to establish the mechanism of the low-energy emission. The author then had an extensive discussion regarding the characteristics of the emission spectra as described in the following sections.

As also shown in Figure 3.3, the broad, visible emission band appeared only in the methylphenylsilane-based polymers PS1–PS3. It is reasonable, therefore, to consider that a difference in the side-chain structure, i.e., methylene-chain length between the Si atom and an aromatic group in the same

monomer unit, determines the generation of the intramolecular interaction probably responsible for the emission.

Figure 3.4 compares the emission spectra of methylphenylsilane-based polymers bearing different alkyl chain lengths in the ammonium group (**PS1–PS3**). The emission band in the visible region seems to be red-shifted with an increase in the carbon-chain length from C_8 (**PS1**) to C_{14} (**PS3**). The apparent spectral shift resembles the photophysical behavior of the exciplex formed between the aromatic hydrocarbons (i.e., arenes) and aliphatic amines; the emission energy closely depends on the alkyl-chain length in the amines [24,25]. This strongly suggests an interaction in which the ammonium moiety is involved.

Contribution of the backbone excited-state to the emission is also supported by the result from Figure 3.5. This figure represents a change in the emission spectra during the course of repeated measurements. Polysilanes are known to be very photoactive under UV irradiation, with photoscission processes occurring for aryl- and alkyl-substituted polymers [26]. These photodegradation processes are manifested by a continuous decrease in the $\sigma^* \to \sigma$ emission in the near-UV region. It appears in Figure3.5 that the visible band declined together with this Si-backbone emission. There should be a strong correlation between the two emitting states.

Therefore, the emission observed only in **PS1–PS3** should be related to the intramolecular interaction between the excited Si backbone and the ammonium moiety. It could be concluded that the most important contribution to this interaction is a CT process from the former (donor labeled D) to the latter (acceptor labeled A), based on the low ionization energy of general polysilanes, which is further decreased in the excited state, and the large electron affinity of ammonium compounds. The presented model also confirms that an excited
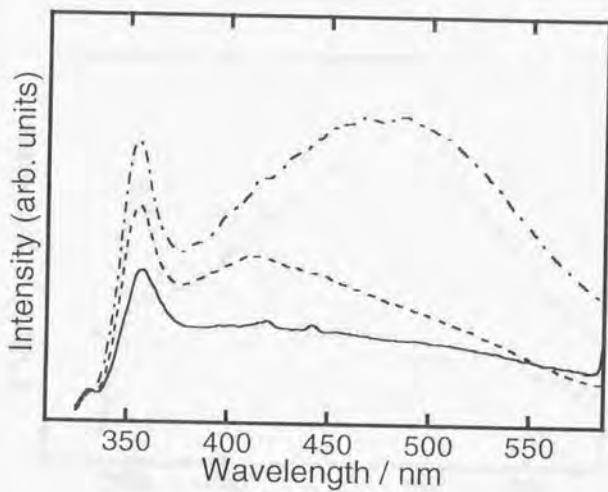
Figure 3.4. Emission spectra of the series of methylphenylsilane-based amphiphilic polymers having different alkyl chain lengths in the side ammonium group. This figure contains curves of **PS1** (——), **PS2** (- - -), and **PS3** (—·—) in chloroform solution, which are measured under the same conditions as Figure 3.3.
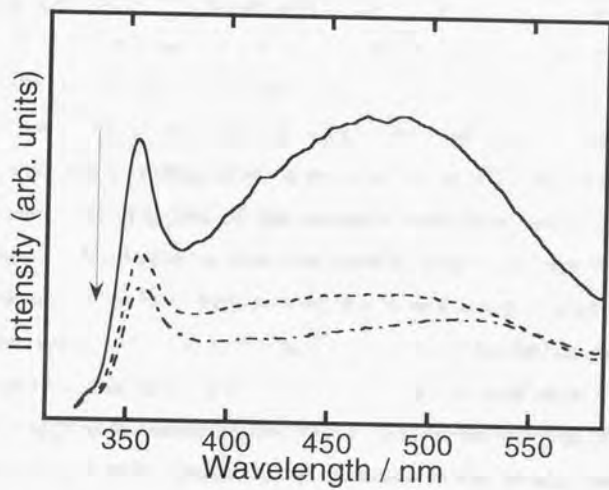
Figure 3.5. Change in the emission spectra of **PS3** (in chloroform) during the course of repeated measurements. Each measurement was made under the same conditions as Figure 3.3.

complex, which the ammonium moiety forms with the excited σ-conjugated segment, would lead to the appearance of the broad emission in the visible region.

Another mechanism to account for the visible emission might be suggested. A phenyl group contributes to the formation of the excited complex as its counterpart. This mechanism was based on the above-mentioned studies regarding the CT complex between polysilane and TCNE molecules [20,21]. However, the mechanism is not likely due to the following facts. First of all, in the polysilane-TCNE system, there was a specific D-A interaction prior to the electronic excitation, leading to the appearance of the CT absorption. This is very different from the case of the exciplex formation under discussion. Second, the exciplex formation should be usually determined from the strength of the intermolecular force between the donor and acceptor species. In the present case, only the Si conjugated backbone is excited by 300-nm light, while both the phenyl and ammonium sites are in the ground state. Thus, the ionization energy of the backbone becomes much smaller than that of the other parts; the most probable electron-acceptor species is the cationic ammonium site. Consequently, the intramolecular intermolecular force between these two species is considered to be the strongest of all the interactions involved in this system.

As a result, the author confirmed that the visible emission, which was first observed for the polysilane, could be attributed to the following exciplex formed between the Si backbone (D) and the ammonium moiety (A):

Step 1, excitation on D: $D + A \rightarrow D^* + A$

Step 2, electron transfer & exciplex formation: $D^* + A \rightarrow (D^+A^-)^*$
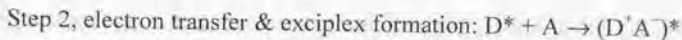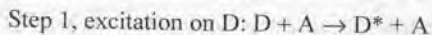
These processes in the D-A system are regulated by the intramolecular interaction based on the chemical structure of the side chain.

Conformational Analysis

The previously mentioned spectroscopic measurement results suggested the intramolecular interaction largely determined by side-group structure would be responsible for the low-energy emission. A conformational energy calculation was carried out to predict the stable main- and side-chain orientations in the polysilanes under study. The structure and the energy parameters employed in the calculation were based on the molecular mechanics program MM3 (AccuModel v.1.1 from MicroSimulations) [27]. The calculation was performed through two steps: (i) the energy calculation for the main-chain orientations specified by the torsion angles; and (ii) the energy minimization of the overall polymer structures including the side-chain orientations. The details are given in the following.

For simplicity, the author focused solely on a single-chain model compound to investigate the intramolecular dynamics therein according to the methodology of Tersigni et al. [28,29] and Sundararajan [30]. The model used in the calculation for main-chain orientations (as noted in (i)) consisted of a backbone of five Si atoms with a phenyl (or benzyl, β-phenethyl) moiety and a methyl group attached to each Si, and additional methyl groups attached to both terminal Si atoms. Apparently, all the polysilanes have asymmetrically substituted chains. Thus, with respect to the plane of the skeletal bonds in the planar all-trans conformation, the phenyl-group containing substituents on the three internal Si atoms can be all up, all down, or alternate, for a total of eight possible configurations. According to a previous study [30], the author limited his choice of input structures in the following calculation to the three configurations in which the phenyl (or benzyl, β-phenethyl) groups on the internal Si atoms are (up, up, up), (up, down, up), and (up, up, down) as shown in Figure 3.6.
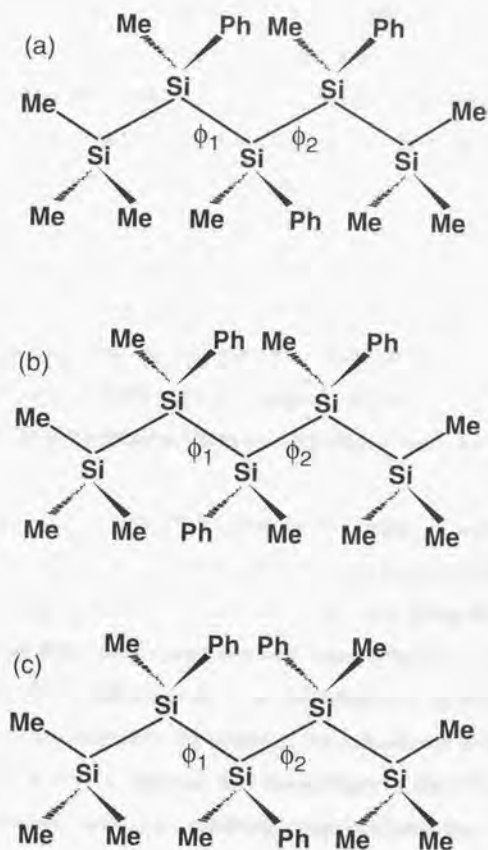
Figure 3.6. A schematic of the model compound used for the calculation of the main-chain orientations. The phenyl groups refereed to as Ph should be replaced by benzyl or β-phenethyl groups in the case of the calculation for **PS4** and **PS5**, respectively. Note the relationship between successive bonds for the various configurations of the phenyl group: (a) (up, up, up), (b) (up, down, up), and (c) (up, up, down). The two backbone torsion angles are designated as ϕ_1 and ϕ_2.

By analogy with previous studies of other polysilanes [28,29,31], molecular structures and relative conformational energies were calculated as a function of rotation about two adjacent, backbone Si-Si bonds within the model compounds, as described by the torsion angles ϕ_1 and ϕ_2. In general, particular attention should be paid to the conformational states in the vicinity of the trans (T), gauche-plus (G^+), and gauche-minus (G^-) conformations corresponding to the familiar three-state (i.e., T, G^+, G^-) rotational scheme found for the analogous carbon backbone polymers [31]. However, the present calculations for the main-chain orientations showed that one of the bonds being in the G state (i.e., $TG^\pm$, $G^\pm G^\pm$, $G^\pm G^+$) leads to high energy. From this result, G states of any type or in any sequence would be virtually excluded at room temperature as reported by Welsh [33].

As shown above, the position of the absorption maximum was shifted to longer wavelengths for the methylphenylsilane-based polymers (**PS1-PS3**) due to an increase in the population of the T conformation in the Si backbone. Thus, these polymers derived from poly(methylphenylsilane) (PMPS) would almost exclusively prefer the TT conformation. This preference is overwhelmingly stronger than that in other polymers. In contrast, the calculation results for all the configurations in Figure 3.6 showed that the minima in the TT state were shifted from the idealized value, i.e., perfectly staggered position ($\phi_1 = \phi_2 = 180°$), even in the case of the phenyl-substituted compounds. The shift in the TT minimum for the (up, down, up) configuration was the smallest of the three. This can be rationalized on the basis of interaction between the side chains on the adjacent Si atoms; the two phenyls are trans to each other and as are the methyl groups. Accordingly, as far as the PMPS-based **PS1-PS3** are concerned, the author adopted only the (up, down, up) configuration in the calculation, while all three in Figure 3.6 were considered for **PS4** and **PS5**. In

this context, the minima in the TT states are expected to be largely shifted in the latter case including the (up, up, up) and (up, up, down) configurations. In fact, the significant displacement from the T conformation was calculated for **PS4** and **PS5**, possibly resulting in the higher-energy absorption maximum appearing in Figure 3.2.

Starting from the stable main-chain orientations found in step (i), energy minimization was carried out to search for the most stable side-chain orientation. In this calculation, the author used another model compound where long-chain ammonium substituents were added to the preceding one. The ball-and-stick atomic model for the minimum-energy conformation of **PS3** is illustrated in Figure 3.7. The main-chain orientation in this structure was (ϕ_1, ϕ_2) = (178°, 173°), which is not significantly shifted from that determined in step (i). This small shift in the stable structure indicates the presence of a considerable steric constraint by the accompanying very long, bulky side chain. Additionally, it should be noted that the center-to-center distance between the ammonium group and the Si in the same monomer unit was 6.9 Å for **PS3**, whereas those for **PS4** and **PS5** were 7.4 Å and 8.9 Å (averages of the values for the three configurations), respectively.

In the present case, the electron transfer from the excited Si backbone to the ground-state ammonium moiety is the most important for the exciplex formation. This transfer may occur either by a direct process or by an indirect process involving phenyl groups attached to the backbone. Which process should be assumed in order to provide a more suitable interpretation of the results? The author postulates that the phenyl groups do not provide a large contribution to the excited-state phenomena under discussion, as described above, and prefers the former process to the latter. This assumption leads to the consideration that the different Si-ammonium distance essentially determines the
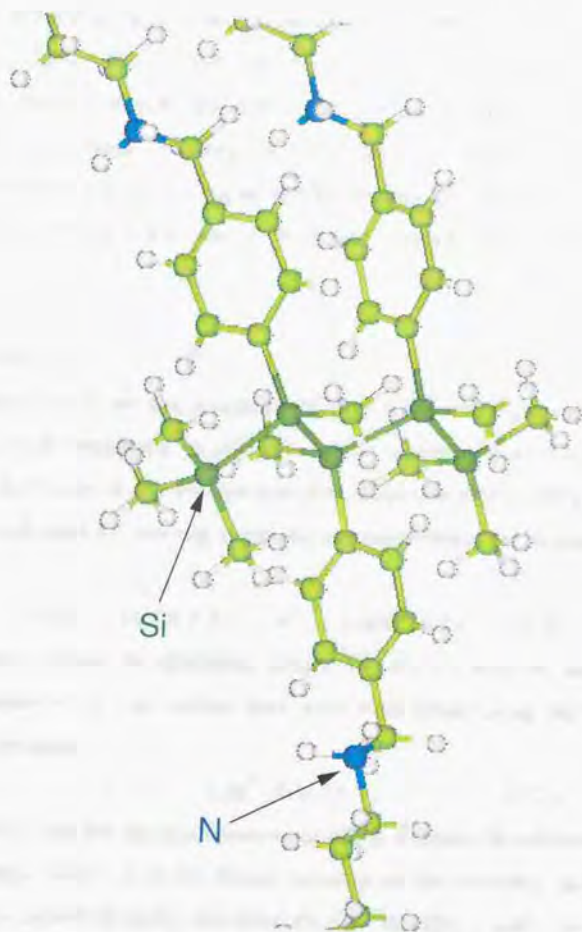
Figure 3.7. The most probable conformation of **PS3**. The overall long alkyl chains in the ammonium group are omitted, although they were considered in the calculation. The energy minimization was performed on both the main- and side-chain orientations.

photophysical behavior of the three polysilanes. Thus, based on the calculated results, the difference in the spectral profiles of Figure 3.3 is simply explained as follows. The exciplex cannot be formed in **PS4** and **PS5**, in which the methylene chain is directly bonded to the polymer backbone and keeps the ammonium site from overlapping the Si orbital in the same monomer unit. In contrast, the exciplex can be formed in **PS3** because the complex-forming parts easily approach each other, and an efficient overlap between their orbitals occurs.

Solvent Effect

The solvent effects on the emission arising from a CT process are very interesting and important in relation to the electronic structures of and electronic processes in the formed exciplex. The effect of solvent polarity is normally evaluated by plotting emission maxima versus the solvent polarity parameter

$$f = (\varepsilon - 1)/(2\varepsilon + 1) - (n^2 - 1)/(4n^2 + 2) \qquad (3.1)$$

where ε and n denote the dielectric constant and the refractive index of the solvent, respectively. The plotted data were then fitted using the following theoretical equation.

$$\nu = \nu_0 - (2\mu^2 / hca^3) f \qquad (3.2)$$

where ν and ν_0 are the emission maximum of the exciplex in solution and in a vacuum, respectively, μ is the dipole moment of the exciplex, and a is the radius of the spherical cavity occupied by the exciplex. h and c are Planck's constant and the light velocity, respectively. As easily predicted by this so-called Lippert-Mataga equation [34,35], the exciplex emission was shifted to the longer wavelength with an increase in solvent polarity. This behavior may be understood on the basis of the fact that the exciplex can exist more stably in

polar solvents than in non-polar solvents.

In Figure 3.8 the wavenumber of the emission maximum in pure solvents is plotted versus f, and a very small effect was observed for the present exciplex system. According to the above theory, such a small slope of the plot is indicative of a large dipole moment for the intramolecular exciplex. This could result from a larger separation of the ammonium moiety and the Si atoms in the formed exciplex than that expected from the above calculation. The author has considered here the peculiarity that the σ-delocalized state of the Si backbone is related to the exciplex formation to give one possible explanation for the observation as follows.

As is well-known in most exciplex systems, the CT interaction in the excited state is primarily responsible for their formation. In the present case, the electron transfer from the excited Si backbone (D^*) to the ammonium (A) is expected to be the most important interaction. Thus, the intermediate CT configuration (or charge-separation state), $(D^+A^-)^*$, may be regarded as polysilane radical cations, in which a hole was injected into the backbone. Tagawa et al. [36], in a pulse radiolysis study on both the radical cation and anion of polysilanes, reported that the added hole was delocalized over the Si-conjugated main chain. Consequently, the extensive delocalization of the hole in this scheme probably separated the D-A pair in the exciplex, leading to the small solvent effect shown in Figure 3.8. It can be concluded, therefore, that the exciplex in the polysilane presented here is different from that of which was already studied by several authors.
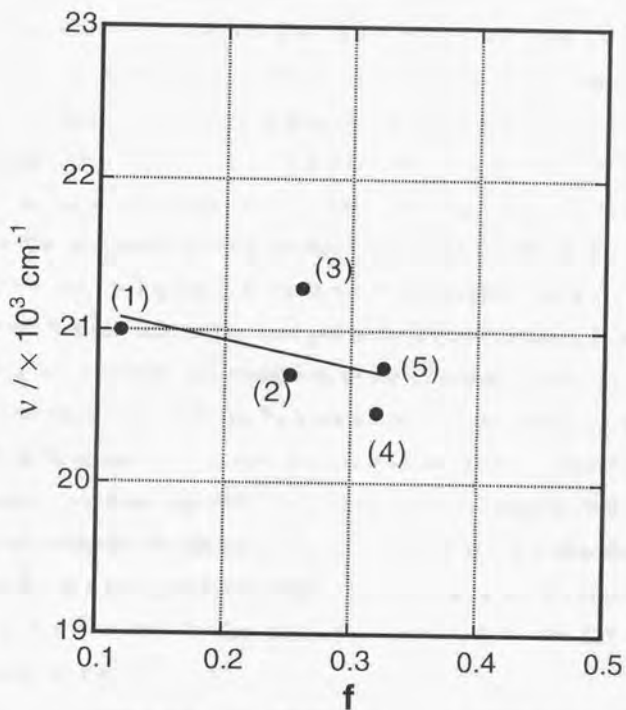
Figure 3.8. Solvatochromic shift of the **PS3** exciplex emission spectrum in neat solvents: (1) carbon tetrachloride, (2) chloroform, (3) chlorobenzene, (4) dichloromethane, (5) 1,2-dichlororthane.

3.3.2.   Intermolecular Interaction in Film Samples

The ion-induced spectra recorded from a solvent-cast film (a) and a 500-layered LB film (b) of the polysilane **PS3** on a Si substrate are depicted in Figure 3.9. These spectra were measured during the initial irradiation stage, where the irradiation damage is negligible (the ion fluences were 0.12 $\mu C/cm^2$ for (a) and 0.16 $\mu C/cm^2$ for (b)). The films prepared for the experiment were thin enough to have homogeneous irradiation without a depth profile. This was based on the calculation of the deposited energy with the TRIM-89 code [36].

Obviously, in Figure 3.9, another broad emission band, to which no assignment has yet been made, emerged at the longer wavelength (around 560 nm). This new emission was found only in the solvent-cast film, while the 400-500-nm emission was observed for both films. As described in Chapter 2, the LB film of the obtained polysilanes was oriented parallel to the dipping direction, in contrast to the film attained by the simple solvent casting method. Thus, this spectral discrepancy should be ascribed to a difference in molecular ordering between the two films, and the origin of the emission can be regarded as an example of the intermolecular interaction regulated by the LB molecular handling technique.

Here, to present a plausible explanation for the appearance of the lowest-energy emission, the author has considered the interaction between adjacent molecules in the excited state. In line with the above discussion on the 400-500-nm emission, it can be assumed that the new band originates from an intermolecular interaction, leading to formation of a similar type of exciplex, of course, although the possibility that the emission process might involve some other complexities cannot be entirely excluded. On the basis of this assumption, the LB film in which each molecule fixed at specific location did not exhibit an
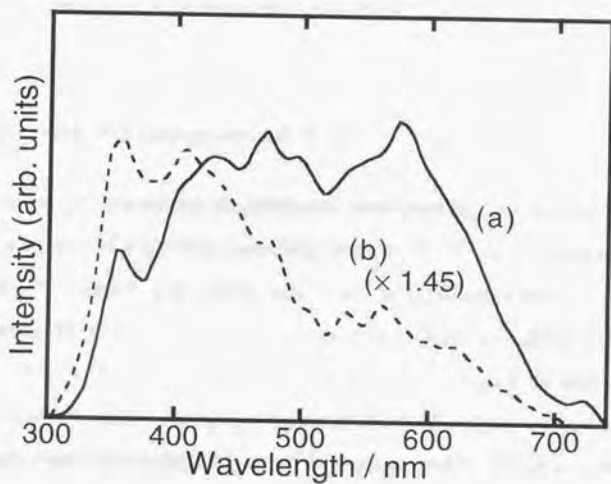
Figure 3.9. Ion-induced emission spectra of a solvent-cast film (a) and a 500-layered LB film (b) of the amphiphilic polysilane **PS3** on a Si substrate. The fluences of 2 MeV H^+ were 0.12 $\mu C/cm^2$ for (a) and 0.16 $\mu C/cm^2$ for (b), respectively.

emission because the intermolecular distances were constantly so great that the complex could not be formed. On the other hand, in the solvent-cast films where each molecule is randomly located, an ammonium site in one molecule can be incidentally close to a Si conjugated segment in a neighboring molecule, so that an efficient overlap between their orbitals is established. Only under this condition would it lead to intermolecular exciplex formation.

3.3.3. Behavior of Photogenerated Holes

As mentioned in the introduction, electronic transport in polysilanes has been one of the subjects of vigorous scientific activity [7-9]. In comparison with common π-conjugated polymers such as poly(diacetylene) [37] and polythiophene [38], polysilanes exhibit an unusually high hole drift mobility on the order of 10^{-4} $cm^2V^{-1}s^{-1}$ [7,39,40]. In spite of such a high hole mobility, the quantum efficiency of the charge-photogeneration of polysilanes is low. For example, poly(methylphenylsilane) (PMPS; represented by **PS-A** in Chapter 2) exhibited a hole-generation efficiency of up to 1% [8]. The improvement in both factors will be needed to make the polymer the best photoconducting material.

Many doping experiments using some appropriate dopants, namely, electron donors or acceptors have significantly improved the photoconducting properties of polymeric materials. Especially, in the case of polysilanes, oxidative doping with electron acceptors, such as iodine (I_2) and fullerenes, would be preferred to reductive doping [41-43]. This doping property is supported by the transport mechanism that photo-induced holes move along the Si backbone as shown in Figure 3.10. However, the molecularly doped
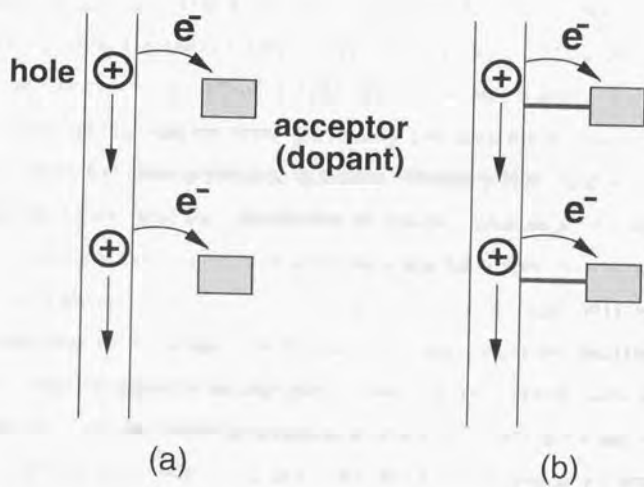
Figure 3.10. Schematic diagram of methods for doping into polysilanes: (a) "intermolecular doping"; (b) "intramolecular doping".

polysilanes become extremely sensitive to air or moisture and so they have not yet exhibited stable photoconductivity for a long time period.

In order to solve this problem, the synthesis of polysilane derivatives containing electron acceptor groups in the side chain has been investigated for some time. Such an approach, often referred to as "intramolecular doping" (Figure 3.10 (b)), causes the polysilane substituents to act as electron-acceptor dopants. This new method can realize higher photoconductive performance instead of using the conventional "intermolecular doping" (Figure 3.10 (a)) and may further precisely control it. Nitro groups in polysilanes with attached π-conjugated chromophores were previously found to act as electron acceptors and improve the photogeneration quantum efficiency [44]. In the present study, it was anticipated that the introduction of cationic ammonium moieties into the side chain of polysilanes would provide a similar effect. Actually, the above sections indicated the existence of efficient excited-state electron transfer between ammonium moieties in the side chain and polysilane backbones, which leads to the formation of an exciplex between them. Here the author describes the results of photocurrent measurements made using the obtained polysilanes. They involve an attempt to control the behavior of photo-generated holes through the D-A processes due to various molecular interactions.

In the experiments, the author selected, from the five polysilanes, **PS2** and **PS3**, each of which has a phenyl group directly attached to a Si atom. In a recent study of G.P. van der Laan et al. [45], the influence of the phenyl group appeared in both the hole drift mobility and charge-photogeneration efficiency. Thus, the selection is suitable to compare the relative effects of molecular interactions without any contribution of the phenyls. The polymer films, 10 μm thick, were cast from the chloroform solutions (about 10 wt %) on aluminum substrates by a bar-coating technique. The sandwich structure was completed

by evaporating a semitransparent Au top contact as shown in Figure 3.11 (a). The measurements were based on the usual Time-of-Flight (TOF) experiments at room temperature, whose arrangement is schematically presented in Figure 3.11 (b). A KrF excimer laser (248 nm) was used as the excitation light source; the light-intensity incident on the sample was about 10 mJ/cm^2 per pulse. The laser pulses with a 2 ns width were strongly absorbed on the upper surface of the polymer films through the semitransparent Au top contacts, leading to plane-like charge packets. These carriers were forced to move due to the applied electric fields. The transient current was observed as voltage signals over 3-30-kΩ resistances using a digitizing oscilloscope. It is noteworthy that all the samples showed no evidence of photodegradation even under repeated pulse excitations.

Figure 3.12 shows a typical transient TOF current signal for the parent polysilane, PMPS, with the irradiated electrode positively biased (electric field: 1.0×10^5 V/cm). The signal must ideally have a rectangular shape, indicating movement of plane-like charge carriers followed by their simultaneous arrival at the bottom contact. The observed signal, however, shows a long current tail. This tail is indicative of charge dispersion through the transport similar to that observed in a variety of hole transporting organic media. From such a dispersive trace, an average transit time can be determined using the double logarithmic plot shown in the inset of Figure 3.12.

The TOF current-mode transit pulse for **PS3** is then shown in Figure 3.13, obtained under the same conditions as PMPS. Unlike the PMPS curve, there appears a sharp decrease in the photocurrent just after the laser flash, even in a stronger electric field. This is probably due to a very rapid trapping and charge recombination in the vicinity of the irradiated electrode. For the other polysilane, **PS2**, a similar behavior was found. In these cases, the average transit time
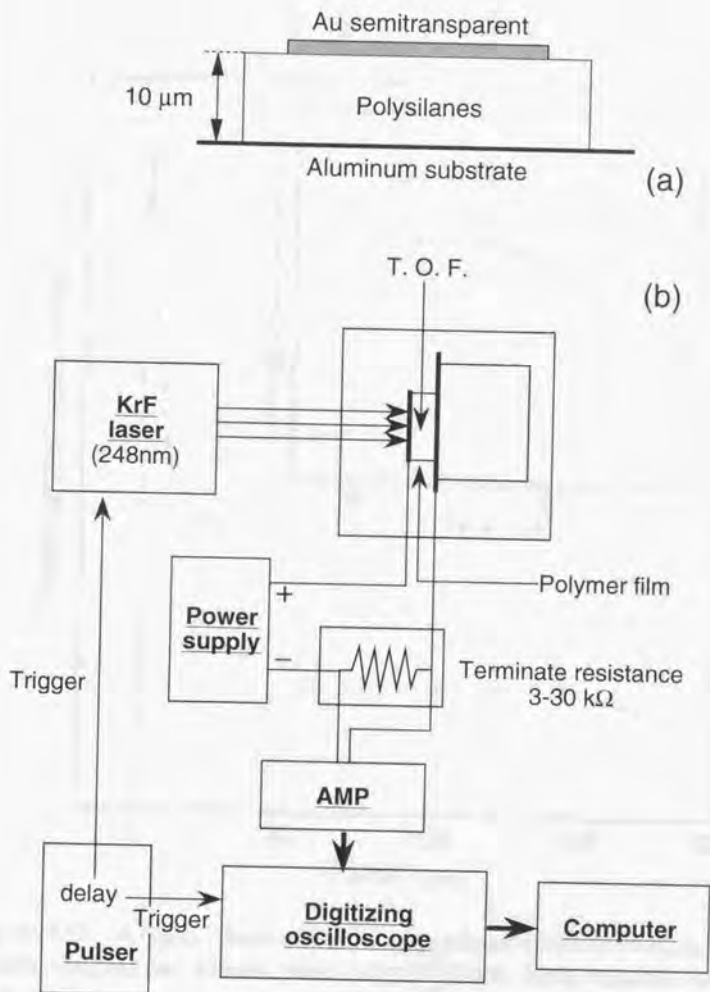
Figure 3.11. (a) The sandwith structure of electrodes and a polysilane film, which was employed in the TOF measurements. (b) Schematic experimental arrangement for the measurements of transient photocurrents.
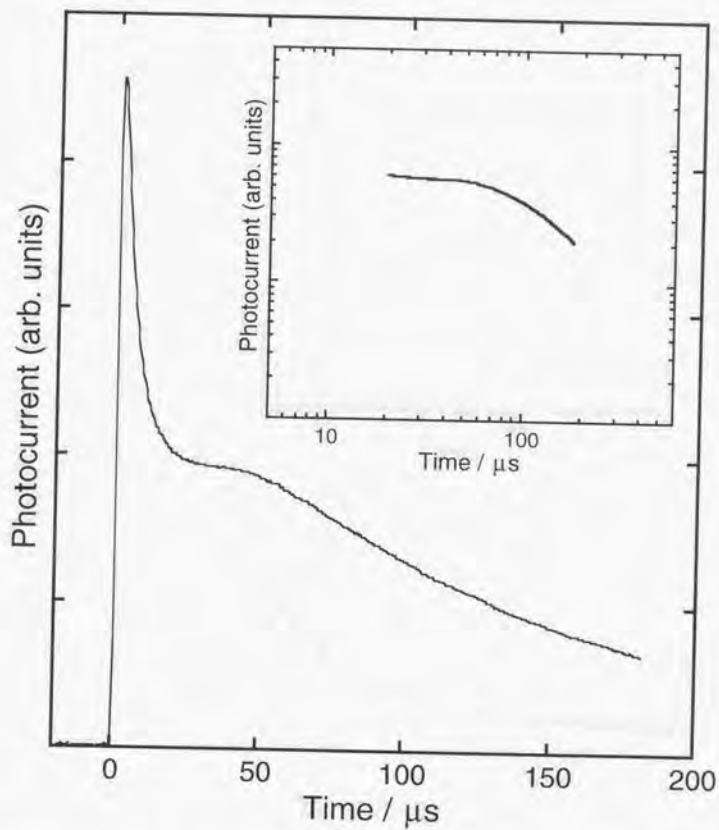
Figure 3.12. A typical shape of the transient current traces observed in PMPS at room temperature. Electric field: 1.0×10^5 V/cm. Inset: replotted curve in log-log coordinates.
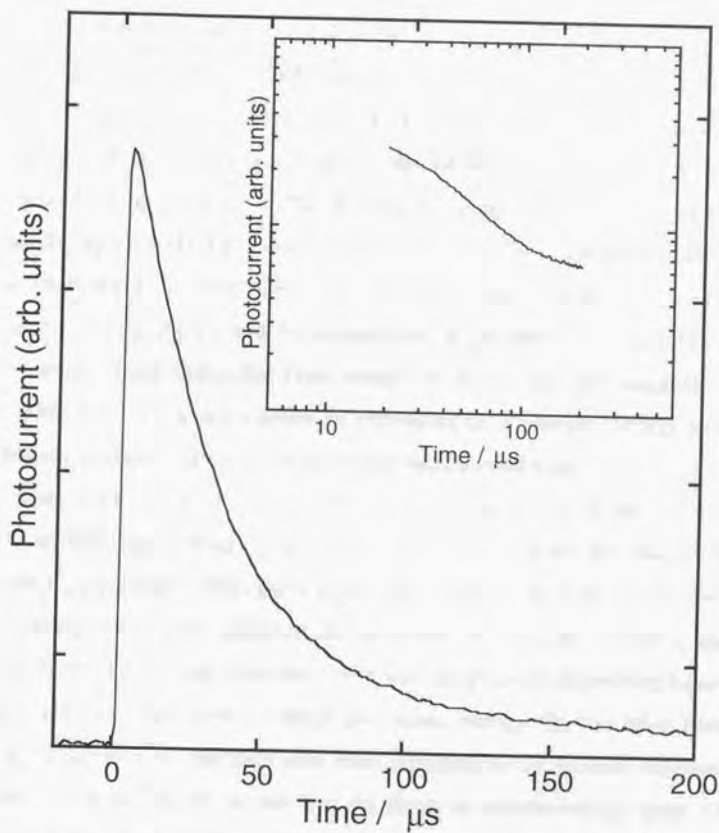
Figure 3.13. A typical shape of the transient current traces observed in **PS3** under the same condition as Figure 3.12. Inset: replotted curve in log-log coordinates.

cannot be determined because the curve replotted in log-log coordinates (inset of Figure 3.13) has no branches characterized by different exponents and no breakpoint of the exponent.

The photocurrent data will now be discussed from a different point of view. The current decay curves like Figure 3.13 were well fitted with a single-exponential function; the goodness of the fit was judged from correlation coefficients being close to 1. The decay rates computed by the fit are plotted versus the applied electric-field strength in Figure 3.14. Apparently, there is a linear relationship between them in the measured range, qualitatively as expected based on the trapping and recombination processes. This electric-field dependence varied somewhat from sample to sample [8] and suggests that a detectable but very small number of photogenerated charge carriers do reach the bottom contact under the present experimental conditions.

It should be noticed here that the decay is roughly a factor of 1.3 times slower in **PS3** than in **PS2**. Broadening of the decay curves was also observed for other polysilanes when the temperature was raised [44]. In that case, at higher temperatures, the shape of the curve became similar to PMPS, and the hole mobility determined from this curve was temperature-dependent because it is thermally activated with a certain activation energy. On the other hand, as already described, no mobility data were obtained in the present experiments. Anyhow, it would be fair to say that the decay is determined by some effect, which may be like the above-mentioned temperature effect on the mobility.

Here, to provide an interpretation of this behavior, the following assumption is made: the density of the trapping species homogeneously distributed in each film is the same. Chloride ions, Cl^-, existing as counter ions of the ammonium cations, are the most probable candidate for hole-trapping sites. Thus, the present assumption also states that no difference in the
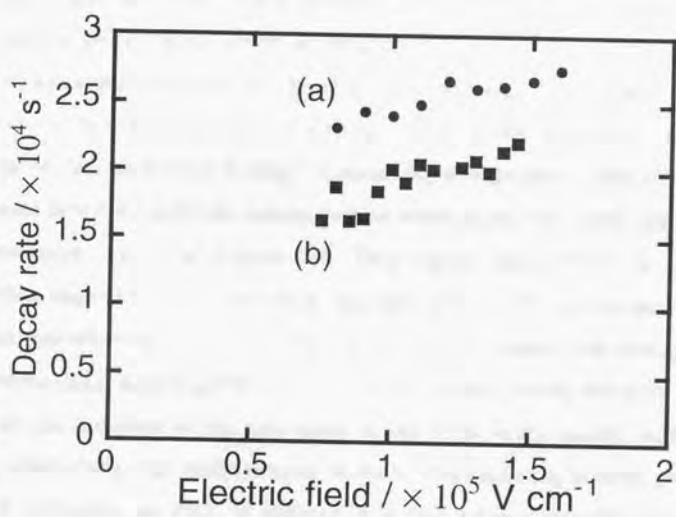
Figure 3.14. The decay rates deduced from single-exponential fits to the photocurrent curves of (a) **PS2** and (b) **PS3** as a function of the electric field.

introduction ratios of the alkylammonium group is found between **PS2** and **PS3**. If, as assumed in Chapter 2, the chloromethylated groups on the phenyl group have completely reacted with the tertiary amines, this seems reasonable because both polysilanes were produced by the same chloromethylated intermediates. Consequently, based on the assumption made here, the effects of the trapping and recombination processes are common to both films and their contribution to the photocurrent decay can be ignored.

Which should then be considered as an alternative? The findings of many previous studies as noted above virtually lead to the incorporation of the concept of "intramolecular doping". Concerning this standpoint, the polysilanes examined here have different intramolecular interactions that clearly appeared in the emission spectra of Figure 3.4. This figure shows that the spectral properties depend on the length of a long alkyl chain in the ammonium group. The relative efficiency of the 400-500-nm emission increases with elongation of the carbon chain from C_8 (**PS1**) to C_{14} (**PS3**). In other words, electron transfer from an excited state of the polysilane to the ammonium moiety in the side chain, which forms the exciplex prior to the visible emission, is more enhanced in **PS3** compared to **PS2**. It follows that this charge-transfer interaction modulates the behavior of the photo-induced current. In line with this argument, it is possible to regard the D-A processes involving the exciplex formation as an example of intramolecular dopant effects controlling the behavior of the photogenerated holes with the ammonium group acting as the electron acceptor. Importantly, the molecular interaction regulated by the different chemical structures determines these effects.

At last, note that the hole-photogeneration efficiency, i.e., the number of holes generated by a laser pulse, was found to be larger in **PS2** than in **PS3**. This correlation is contrary to the above expectations for reasons unknown.

The author should point out that the present interpretation does not take the phenyl groups into account but, actually, there is a possibility that they are also excited by 248-nm light. Therefore, as far as this problem is concerned, rather complex mechanisms might be involved.

3.4.   Conclusions

The author investigated the molecular interaction in the ammonium-type amphiphilic polysilanes synthesized in Chapter 2 using extensive spectroscopic measurements. The broad, visible emission other than that originating from the $\sigma^* \rightarrow \sigma$ transition of the Si-conjugated backbone was observed for some of these polysilanes for the first time.

In the present study, the molecular interaction was examined from two aspects. One is an *intramolecular* interaction regulated by different side-chain structures in the polysilanes. The 400-500-nm emission that appeared only in the poly(methylphenylsilane)-based polymers was a result of exciplex formation between the ammonium moiety and the Si backbone. On a basis of the model that the electron transfer to the ammonium might take place by direct transfer from the backbone, the appearance of this emission can be reasonably rationalized by considering the intramolecular interaction determined by the distance between the pair. The emission was not very sensitive to solvent polarity, indicating the peculiarity that the σ-delocalized state of the backbone acts as an exciplex-counterpart. Furthermore, it is worth mentioning that behavior of the photo-excited holes in the polysilane was found to be modulated by the charge-transfer process involving the exciplex formation. This finding

should be important in view of the applicability of polysilanes in electronics, especially in photoconductive materials. The other is an *intermolecular* regulation due to the different varieties of molecular ordering or packing. Comparing the emission spectra between the polysilane films prepared by the solvent-casting and LB technique suggested that a different intermolecular interaction exists between the films. This interaction might be the origin of the emission around 560 nm additionally observed only for the solvent-cast film.

REFERENCES

[1] R.D. Miller and J. Michl, *Chem. Rev.* **1989**, *89*, 1359.

[2] S. Yajima, *Am. Ceram. Soc. Bull.* **1983**, *62*, 893 and references therein.

[3] R. West , A.R. Wolff, and D.J. Peterson, *J. Radiat. Curing* **1986**, *13*, 35.

[4] A.R. Wolff and R. West, *Appl. Organomet. Chem.* **1987**, *1*, 7.

[5] J.M. Zeigler, L.A. Harrah, and A.W. Johnson, *SPIE Adv. Resist Technol. Proc. II* **1985**, *539*, 166-174.

[6] D. Hofer, R.D. Miller, and G.C. Willson, *SPIE Adv. Resist Technol.* **1984**, *469*, 16.

[7] R. West, L.D. David, P.I. Djurovich, K.L. Stearley, K.S.V. Srinivasan, and H. Yu, *J. Am. Chem. Soc.* **1981**, *103*, 7352.

[8] R.G. Kepler, J.M. Zeigler, L.A. Harrah, and S.R. Kurtz, *Phys. Rev. B* **1987**, *35*, 2818.

[9] M. Fujino, *Chem. Phys. Lett.* **1987**, *136*, 451.

[10] F. Kajzar, J. Messier, and C. Rosilio, *J. Appl. Phys.* **1986**, *60*, 3040.

[11] J.M. Zeigler, *Mol. Cryst. Liq. Cryst.* **1990**, *190*, 265.

[12] M.A. Abkowitz, F.E. Yuh, H.J. Weagly, and M.S. Stolka, *Solid State Commun.* **1987**, *62*, 547.

[13] D. Bryce-Smith, A. Gilbert, and G. Klunklin, *J. Chem. Soc., Chem. Commun.* **1973**, 330.

[14] T. Seki, T. Tamaki, and K. Ueno, *Macromolecules* **1992**, *25*, 3825.

[15] T. Seki, T. Tamaki, K. Ueno, and Y. Tanaka, *Thin Solid Films* **1994**, *243*, 625.

[16] T. Seki, N. Tanigaki, K. Yase, A. Kaito, T. Tamaki, K. Ueno, and Y. Tanaka, *Macromolecules* **1995**, *28*, 5609.

[17] T. Seki, A. Tohnai, T. Tamaki, and A. Kaito, *Chem. Lett.* **1996**, 361.

[18] L.A. Harrah and J.M. Zeigler, *Macromolecules* **1987**, *20*, 601.

[19] M. Kira, K. Takeuchi, C. Kabuto, and H. Sakurai, *Chem. Lett.* **1988**, 353.

[20] V.F. Traven and R. West, *J. Am. Chem. Soc.* **1973**, *95*, 6824.

[21] H. Sakurai, M. Kira, and T. Uchida, *J. Am. Chem. Soc.* **1973**, *95*, 6826.

[22] O. Ito, M. Terajima, and T. Azumi, *J. Am. Chem. Soc.* **1994**, *112*, 444.

[23] N. Kajiwara and K. Murakami, *Mukikobunshi* (Japanese); Sangyotosho: Tokyo, 1992.

[24] N. Nakashima, N. Mataga, F. Ushino, and C. Yamanaka, *Int. J. Chem. Kinet.* **1973**, *5*, 833.

[25] A. Nakashima, *Bull. Chem. Soc. Jpn.* **1969**, *42*, 3409.

[26] P. Trefonas, III, R. West, R.D. Miller, and D. Hofer, *J. Polym. Sci., Polym. Lett. Ed.* **1983**, *21*, 823.

[27] N.L. Aligned, Y.H. Yuh, and J.-H. Lii, *J. Am. Chem. Soc.* **1989**, *111*, 8551.

[28] W. Lin, S.H. Tersigni, and W.J. Welsh, *Comput. Polym. Sci.* **1991**, *1*, 225.

[29] S.H. Tersigni and W.J. Welsh, *Comput. Polym. Sci.* **1992**, *2*, 1.

[30] P.R. Sundararajan, *Macromolecules* **1988**, *21*, 1256.

[31] J.R. Damewood, Jr. and R.C. West, *Macromolecules* **1985**, *18*, 159.

[32] P.J. Flory, *Statistical Mechanics of Chain Molecules*; Interscience: New York, 1969.

[33] W.J. Welsh, J.R. Damewood, Jr., and R.C. West, *Macromolecules* **1989**, *22*, 2947.

[34] E. Lippert, *Z. Naturforsch* **1955**, *109*, 541.

[35] N. Mataga, Y. Kaifu, and M. Koizumi, *Bull. Chem. Soc. Jpn.* **1955**, *28*, 690.

[36] J.F. Ziegler, J.P. Biersack, and U. Littmack, *The Stopping Range of Ions in Solids*; Pergamon Press: New York, 1985. R.R. Chance, G.N. Patel, and J.D. Witt, *Chem. Phys.* **1979**, *71*, 206.

[37] O. Inganas, W.R. Salanek, J.E. Osterholm, and J. Laakaso, *Synth. Met.* **1988**, *22*, 2141.

[38] M. Stolka, H.-J. Yuh, K. McGrane, and D.M. Pai, *J. Polym. Sci. Part A: Polym. Chem.* **1987**, *25*, 823.

[39] M.A. Abkowitz, M.J. Rice, and M. Stolka, *Phil. Mag. B* **1990**, *61*, 25.

[40] K. Takada, N. Matsumoto, and M. Fukuchi, *Phys. Rev. B* **1984**, *30*, 5871.

[41] K. Takada, N. Matsumoto, and M. Fukuchi, *J. Am. Chem. Soc.* **1986**, *108*, 8186.

[42] Y. Wang, R. West, and C.-H. Yuan, *J. Am. Chem. Soc.* **1993**, *115*, 3844.

[43] J. Pfleger, I. Kminek, S. Nespurek, and W. Schnabel, *IEEE Trans. Electr. Insl.* **1992**, *27*, 856.

[44] G.P. van der Laan, M.P. de Haas, A. Hummel, H. Frey, and M. Möller, *J. Phys. Chem.* **1996**, *100*, 5470.

CHAPTER 4

RBS Analysis of Langmuir-Blodgett Films Bearing Quantum-Sized Cadmium Sulfide Microcrystallites

ABSTRACT

Rutherford backscattering spectrometry (RBS) was used for the first time to analyze the structural changes in cadmium arachidate Langmuir-Blodgett (LB) films during the formation of quantum-sized (Q-sized) cadmium sulfide (CdS) microcrystallites. Beam effects did not influence the RBS spectra under the present irradiation conditions, therefore, the obtained results proved reliable. The spectral change between before and after exposure to hydrogen sulfide (H_2S) suggests that a well-ordered layer structure of the original film was disordered by the sulfidation reaction. This finding was in agreement with that of an in-depth analysis using X-ray photoelectron spectroscopy. Based on a quantitative analysis by a simulation method, Cd migration toward the substrate seemed to be involved. Consequently, the Q-sized CdS produced in hydrophilic interlayers could not be two-dimensional platelets but were spherical particles as reported in previous studies.

4.1.   Introduction

There has been considerable interest in quantum-sized (Q-sized) inorganic semiconductor microcrystallites with dimensions of less than 10 nm because of their structural, chemical, and physical properties which are different from those of the corresponding bulk materials [1]. Such unusual properties originating from the so-called quantum size effect are directly related to various new technologies such as nonlinear optics [2].

Q-sized semiconductor microcrystallites are inherently inclined to aggregate in order to reduce their surface energy. The samples have been carefully prepared in solutions [3], zeolites [4], glasses [5], polymers [6], and surfactant systems [7-12] such as reversed micelles [7], vesicles [8], and Langmuir-Blodgett (LB) multilayer films [9-12]. All these media play a part in restricting crystal growth to the Q-state regime. The use of LB film matrices is particularly suitable for the construction of practical devices, because this technique allows microcrystallites to be coated with molecular precision onto a solid substrate. For microcrystal formation in LB films, a preformed film composed of a metal salt of a long-chain carboxylic acid is exposed to a reducing gas (such as H_2S or H_2Se) [9]. For example, the exposure of cadmium arachidate ($CdAr_2$) LB films to H_2S causes Q-sized cadmium sulfide (CdS) to form by [9-12]

$$(C_{19}H_{39}COO)_2Cd + H_2S \rightarrow 2\ C_{19}H_{39}COOH + CdS \qquad (4.1)$$
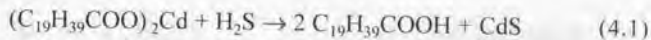
Figure 4.1 illustrates the models proposed for the generation of Q-sized CdS in arachidic acid (AA) LB films. Hydrophilic interlayers of LB films are expected to serve as a well-restricted two-dimensional reaction field. Thus, if the layered structure of the LB matrices is perfectly preserved during the
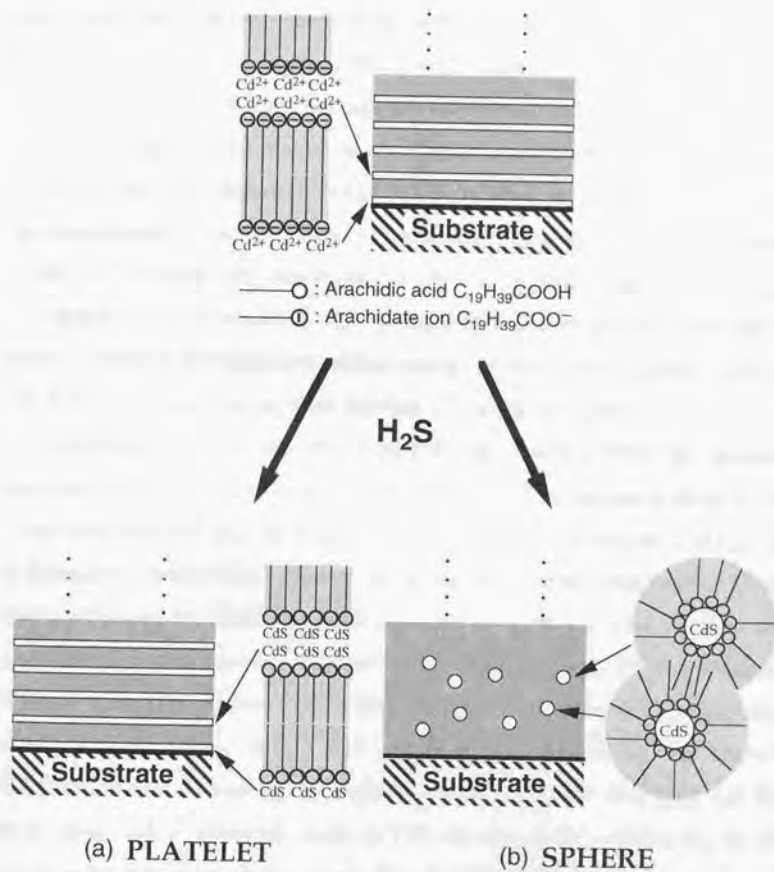
Figure 4.1. Proposed schematic model of Q-sized microcrystallites produced in an LB matrix: in (a) thin-platelet and (b) spherical forms.

particle formation, the particles formed in their interlayers are in thin platelets which have two-dimensional features (as shown in (a)). Such layers are analogous to the superlattices of II-VI semiconductors produced by molecular beam epitaxy [13]. Therefore, the morphology of Q-sized semiconductor microcrystallites in LB films has recently received attention for nonlinear optical applications and the preparation of two-dimensional model compounds [14,15]. However, several papers [10-12] have pointed out the possibility that aggregated particles are produced in a spherical form involving the destruction of the LB assembling structures, as shown in (b). The morphology of incorporated microcrystallites chiefly depends on the relationship between the driving forces to minimize the surface energy of the microcrystallite itself (i.e., cohesive forces) and the physical stability of the LB assemblies.

Information on microcrystal morphology comes from the structural analyses of the LB matrices after H_2S treatment. Techniques such as Fourier transform infrared spectroscopy [10,11], X-ray diffraction [10,12], and ellipsometry [9] have been used to investigate multilayer films bearing Q-sized semiconductors, but little has been reported on these LB film systems using Rutherford backscattering spectrometry (RBS) except for the studies of Johnson et al. [16-18] and Voit et al. [19]. RBS is effective for the analysis of small samples (some mm^2) and provides information on the chemical composition and its homogeneity (depth profiling) in the film [20]. LB films containing high-Z elements (such as Cd) are especially suitable for an RBS analysis, because these films provide high sensitivity to high-Z cations.

In the present study, the author carried out an RBS analysis using $CdAr_2$ LB films before and after the reaction with H_2S, and then derived quantitative information from the raw spectra by a simulation method. The samples were further analyzed using X-ray diffraction (XRD) and X-ray photoelectron

spectroscopy (XPS). These experimental measurements demonstrated the utility of RBS for the analysis of the structural change in the LB films. Finally, the morphology of the CdS microcrystallites formed in the interlayers of the LB films was discussed in comparison with previous results obtained using conventional methods.

4.2.   Experimental Section

4.2.1.   Film Preparation

Arachidic acid, AA, obtained from the Eastman Kodak Company was used without further purification. Cadmium chloride ($CdCl_2$) and sodium hydrogen carbonate ($NaHCO_3$) purchased from Koso Chemical Co., Ltd., were guaranteed grade reagents and used as supplied. The water used in all subphase solutions was doubly-distilled and then passed through a Milli-Q system (Millipore Corp.). H_2S gas was produced by adding a dilute aqueous solution of HCl to a flask containing iron(II) sulfide.

LB films of $CdAr_2$ were built up using a Langmuir 'Teflon' trough (Lauda FW-1; surface area: 560 cm^2) at 19-21 °C. Precursor monolayers of $CdAr_2$ were prepared by spreading a chloroform solution of AA (1×10^{-3} mol dm^{-3}) on subphases containing 4.0×10^{-4} mol dm^{-3} $CdCl_2$ and 5.0×10^{-5} mol dm^{-3} $NaHCO_3$ (as a buffer solution). The spread monolayer, compressed to 35 mNm^{-1}, was transferred to hydrophilic quartz plates by the conventional vertical dipping technique at a dipping speed of ~ 1.5 cm min^{-1} both upwards and downwards. For the RBS analysis, the author deposited 701 monolayers on one

side of the substrate. The transfer ratio for the overall deposition strokes was nearly unity, indicating a normal Y-type deposition.

CdS microcrystals in the LB matrix were synthesized by the method of Smotkin et al. [9]. As also mentioned in the Introduction, the transferred LB films were exposed to a flowing stream of H_2S at room temperature. The reaction time, depending on the layer number of the LB films, was long enough to complete the conversion of all the Cd^{2+} ions in the film to CdS, as will be discussed later.

4.2.2. Characterization Methods

The RBS analysis was carried out at the Research Center for Nuclear Science and Technology, the University of Tokyo, using the 0.1-1.7 MV Tandetron accelerator and a scattering chamber evacuated to 10^{-6} torr. The film samples before and after the H_2S treatment were analyzed using a 2 MeV He^{2+} ion beam with a beam spot of 1-mm diameter and a beam current of 10 nA. A Si (Li) surface barrier detector of 50 mm^2 was positioned at 160° with respect to the normal incident beam for detecting backscattered He ions. The energy resolution of the RBS tract was 20 keV on the [241]Am (5.486 MeV) line. The data acquisition time was 3 min.

XRD patterns were obtained using a Rigaku RAD-γA X-ray diffractometer, operated at 40 kV and 120 mA, with monochromatized Cu Kα (λ = 0.15418 nm) radiation through a Ni filter. Data were collected with a proportional counter in the θ-2θ mode. XPS was conducted in the ultra-high vacuum chamber of a Shimadzu ESCA 850 spectrometer. A Mg (1253.6 eV) X-ray source was operated at 8 kV and 240 W. The destructive in-depth

analysis was performed with Ar ion beam sputtering (0.6 kV, 50 mA) in order to obtain depth profiles of the chemical composition in the films. The sputtering rate for a standard reference sample of SiO_2/Si (a SiO_2 layer on Si) was determined to be about 80 nm/min. In the present study, however, the measured sputtering time was taken as the depth scale because the rate varies with sample composition. The elemental ratio was determined from the XP peak intensities of individual elements through correction of the sensitivity factors of these elements.

4.3. Results and Discussion

4.3.1. Beam Effects

RBS is generally considered to be a non-destructive analysis technique in that power density and dose normally used for the 2 MeV He-ion analysis are small. The temperature rise produced by such a beam is not very large; for example, it can be estimated to be only a few degrees at the surface of a Si wafer. The ion dose is typically three orders of magnitude below that needed to amorphize a single crystal Si layer.

For an analysis of relatively soft organic samples such as LB multilayers, however, RBS can*not* be considered to be non-destructive, because these samples are easily degraded by a flux of MeV ions impinging on the target to produce a spectrum. If some of the resulting defect species are mobile (radiation-enhanced diffusion) or volatile (for example, H_2), then significant changes in the depth distribution or stoichiometry may result. In fact, the

evaporation of the organic components of yttrium arachidate LB films was previously observed during the first few seconds of such a measurement [19]. Thus there exists the possibility that the radiation damage produced during the RBS analysis may lead to an erroneous measurement.

Nevertheless, Johnson et al. [17] suggested in their study of beam effects on backscattering spectra that the measured film thickness and metallic components were reliable provided that moderate doses and beam currents were used. The irradiation conditions used by the author (ion fluences and their rates are 7.2×10^{14} ions/cm^2 and 4.0×10^{12} ions/cm$^2 \cdot$s, respectively) were much milder than those in their study [17] (1.7×10^{17} ions/cm^2 and 1.2×10^{14} ions/cm$^2 \cdot$s). It may be concluded, therefore, that the beam effects are insignificant in the present case although the film turned brown upon beam exposure as they also observed.

Furthermore, the effects of ion beam bombardment during the RBS analysis were investigated by XRD. The XRD measurement is undoubtedly a powerful method for studying the order structure in the perpendicular direction to the plane of the LB films. Figure 4.2 illustrates the XRD patterns of 25-layered LB films of CdAr$_2$ as deposited, after the H$_2$S treatment, and after irradiation with 2 MeV He ions. From the first two patterns, (a) and (b), it was shown that the structure of the LB film underwent a vigorous change. The original LB film, which gave distinct X-ray 00l Bragg peaks (Figure 4.2 (a)), had a well-organized layered structure with a basal-plane spacing (d) of 5.49 nm. This long spacing was almost the same as that reported by Matsuda et al. [21]. After the treatment, all the diffraction peaks disappeared (Figure 4.2 (b)) except for a weak peak (at $2\theta = 6.0°$) due to a new phase. Although the origin of the unexpected peak corresponding to a long spacing of $d = 1.48$ nm is not known, the two patterns indicate that, in the direction perpendicular to the plane

of the substrate, the positions of almost all of the metal ions within the LB films were changed. In other words, the structure of the LB films was completely destroyed.

Figure 4.2 also compares the XRD pattern of the sample irradiated with 2 MeV He ion whose fluence is the same as that used for the RBS analysis. Apparently in this pattern (c), the amplitudes of the diffraction peaks significantly decreased after the irradiation. This finding revealed that the ion irradiation influenced the well-ordered arrays of hydrocarbon chains of the LB films. According to previous studies [22,23], the destruction of the film structure is probably due to hydrogen desorption or a hydrocarbon-bond breaking process during ion beam exposure.

A notable result is the fact that the diffraction peaks still remained in the irradiated sample although they became very weak. This suggests the following conclusion in comparison with the XRD pattern of the H_2S-treated sample showing no original signal (Figure 4.2 (b)): the H_2S treatment has a significant effect on the ordered structure of the LB films compared to the ion irradiation. Thus, it is reasonable to consider that a difference in the RBS spectra found before and after the H_2S treatment is attributed to a certain change induced by the reaction with H_2S, rather than by the irradiation damage which is common to both spectra.

It should be emphasized that although a large amount of damage was created by the analyzing beam, this did not necessarily introduce a significant error into the quantities being analyzed. Actually, no spectral change was observed for the same sample even after 10 minutes of ion-beam exposure. Therefore, the author will ignore, in the following discussion, the effect of ion bombardment on the measured composition and depth profiles in the obtained backscattering spectra.
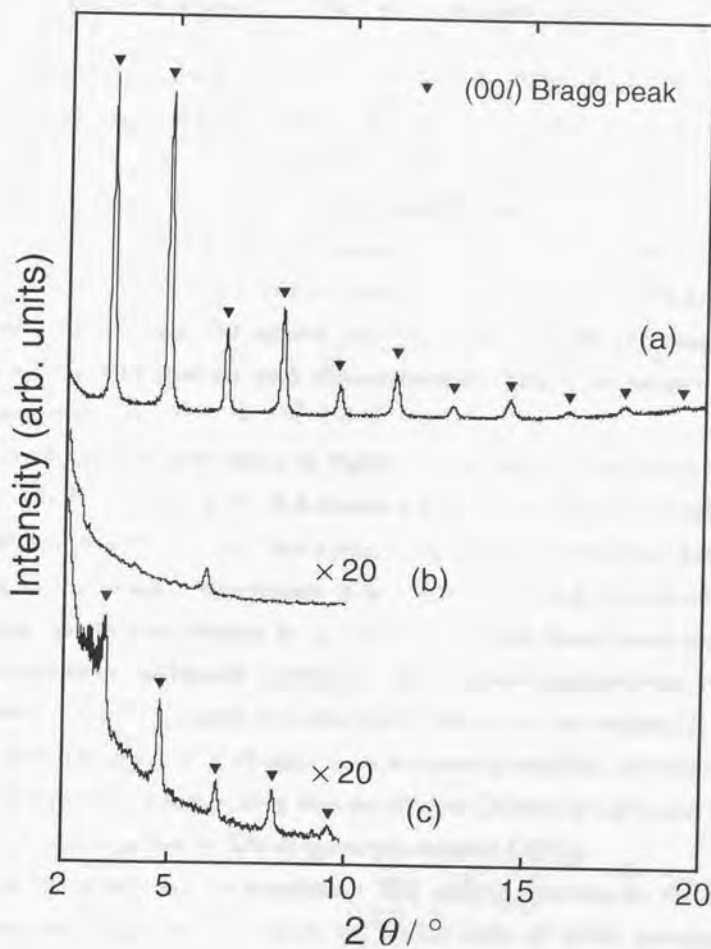
Figure 4.2. X-ray diffraction patterns of 25-layered cadmium arachidate LB films (a) as deposited, (b) after H₂S treatment, and (c) after irradiating the film (a) with He ions. The irradiation conditions were the same as that used for the RBS analysis. All the films were deposited onto a quartz substrate.

4.3.2.   Chemical Reactivity of the CdAr$_2$ LB Films with H$_2$S

The formation of Q-sized CdS particles involves the diffusion of H$_2$S gas into the film and then a subsequent reaction with Cd^{2+} ions as given by equation 4.1. As for the CdAr$_2$ films with 10-40 monolayers, earlier studies using a quartz crystal microbalance [24,25] indicated that the conversion to CdS neared completion within minutes. However, this is not the case with LB films with much more monolayers. It would be expected that such thick films would need a longer reaction time. 701-layered films before and after the H$_2$S treatment used for the RBS analysis were characterized by XPS to investigate their chemical reactivity.

As representatively shown in Figure 4.3 (a), the S 2p signal peaked at about 161.5-162.0 eV in the H$_2$S-treated LB film. Manocha et al. [26] and Lichtman et al. [27] suggested that a peak in this range was associated with the sulfur in the sulfide configuration. It is worth mentioning that almost the identical spectra were obtained for any depth in the same region, which implies a homogeneous sulfidation reaction in the direction perpendicular to the substrate. The Cd 3d$_{5/2}$ signal was observed at 405.6 eV in the original LB film and the H$_2$S-treated (i.e., CdS-bearing) multilayers in both the acid- and salt-form composite films, indicating that the divalent Cd ions in CdAr$_2$ and CdS cannot be distinguished by XPS as previously reported [10,11].

On the other hand, the quantitative XPS analysis provides the available information. Figure 4.3 (b) shows the atomic ratio of sulfur (present as sulfides) to cadmium, S/Cd, determined from XP peak intensities, as a function of the sputtering time counted from the beginning. Note that due to surface contamination mainly from the atmosphere, the data derived from some outermost layers are omitted from this figure. The S/Cd ratios at any depth in
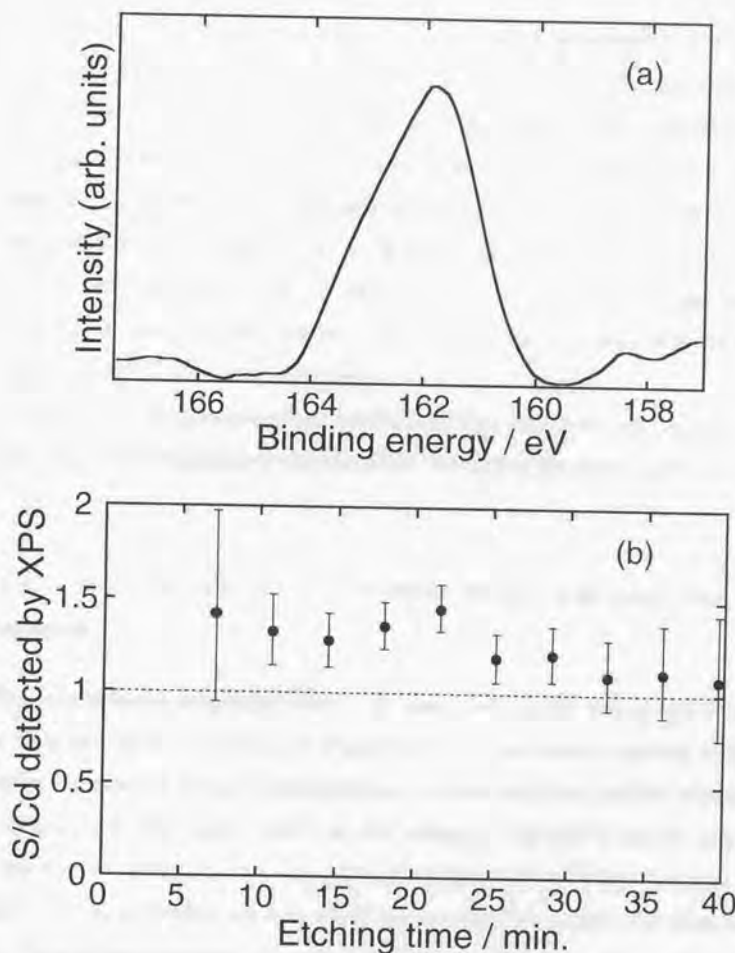
Figure 4.3. (a) Representative S 2p XP spectrum of 701-layered cadmium arachidate LB films after exposure to H_2S. (b) Atomic ratio of sulfur to cadmium (S/Cd) as determined from XP peak intensities versus the sputtering time for the same film. Due to surface coverage of the impurities, this figure does not contain the data on the first several layers (see the text of Section 4.3.2).

the film were found to be greater than 1, which is consistent with the quantitative formation of CdS, although they had large uncertainties due to an inadequate sensitivity to sulfur (easily found in Figure 4.8 (b)). Based on this finding, it would be expected that all Cd^{2+} ions in the film formed CdS. It also demonstrates, of course, the existence of other types of sulfur species, which is predicted from the shape of the S 2p spectrum (Figure 4.3 (a)). Chen et al. [28] claimed that there were at least two sulfur species in copper sulfide incorporated into LB films, one in the form of S^{2-} (sulfur ion) and the other in the form of S_2^{2-} (sulfur molecular ion).

All the results presented here confirm the H_2S diffusion into the innermost layers and then complete conversion of Cd^{2+} to CdS in the entire film.

4.3.3. RBS Spectra of the LB Films Before and After the H_2S Treatment

The backscattering spectra of $CdAr_2$ LB films obtained (a) before and (b) after the H_2S treatment are shown in Figure 4.4. The elemental markers in these spectra indicate the energy corresponding to scattering from surface atoms, the so-called *edge*. The signal located at low energy (≤ 0.6 MeV) may be ascribed to the backscattering from C atoms in arachidate and/or Si and O atoms in a quartz substrate. Hardly any amount of oxygen from arachidate was detected in the present measurement. A well-defined Cd signal was observed at high energy, while the H_2S-treated film (Figure 4.4 (b)) showed a weak S signal overlapping with the Cd signal. Backscattering spectrometry has much lower sensitivity to light elements; under the present experimental conditions, the sensitivity to Cd is about nine times that of S [20], as shown in Figure 4.4 (b).

Accordingly, the following discussion is only focused on the backscattering signals from Cd atoms.

In general, the peak width observed in a backscattering spectrum represents the energy loss of the particles scattered from rear-surface atoms along their inward and outward paths; hence, it is related to the overall thickness of the film. No change was observed in the measured signal width before and after the H_2S treatment although the low-energy step of each signal was considerably smoothed out due to contribution of the energy straggling in the film. This observation, however, does not necessarily mean that the film thickness did not change during the reaction, because the atomic densities (atoms per unit *volume*) of all the elements are not always uniform in the film. For particle formation in multilayers, one might expect that the growth of Q-sized particles in the multilayer causes a thickness change to some extent. Smotkin et al. [9] observed in their ellipsometric measurement of this system that the average change in thickness per layer was about 0.3 nm after H_2S exposure. They then rationalized this small change by proposing the formation of disk-shaped Q-sized CdS. If the film thickness increases by 0.3 nm per layer in the present case, as they observed, the change in total thickness for 701 layers is calculated to exceed 200 nm.

In addition, a difference in the depth profile near the Cd-edge at the highest energy (1.74 MeV) was found in the two spectra shown in Figure 4.4, as indicated by the arrows. The edge of the H_2S-treated sample (b) was more diffuse than that of the untreated one (a). Since the scattering yield at a certain depth is proportional to the number of particular atoms present, the spectral height corresponds to their volume concentration. Thus, this spectral change indicates that the Cd concentration near the front surface of the film was lower after the reaction than that in the untreated film with a uniform elemental
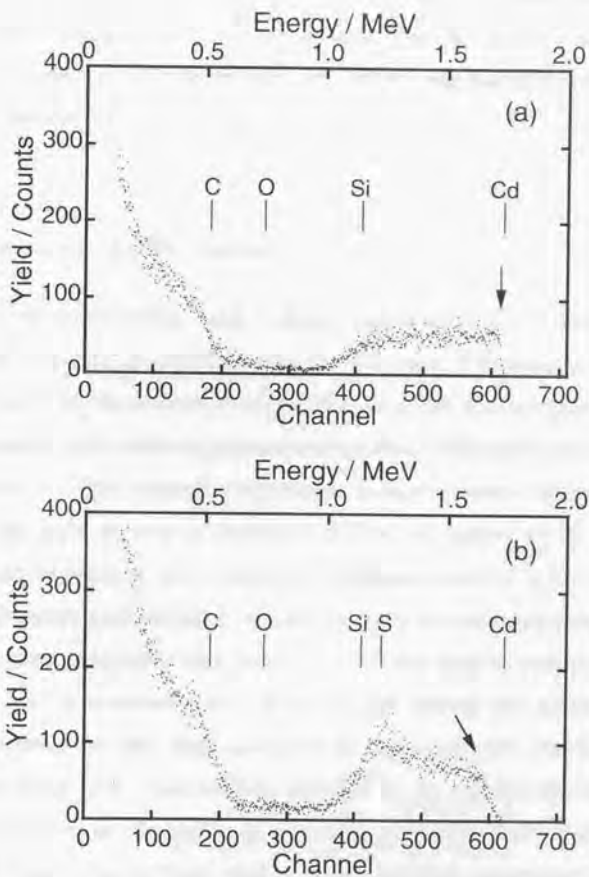
Figure 4.4. Backscattering spectra of 701 monolayers of cadmium arachidate on a quartz plate (a) as deposited and (b) after H_2S treatment. The spectra were taken with He^{2+} ions at 2 MeV at 160°, with a 1 mm-diameter beam spot and 10 nA beam current. Elemental markers indicate surface atoms. Arrows indicate that the Cd-edge of the H_2S-treated sample (b) is more diffuse than that of the untreated one (a).

composition. In other words, it seems that Cd atoms migrated toward the substrate. This is supported by the observation that the intensity of the Cd signal from a deeper area (recorded at lower energy) was higher for sample (a) than that for sample (b).

4.3.4. Simulation of RBS Spectra

As stated in the introduction, RBS is highly informative for an analysis of surface layers in solids. In practical analysis, however, it frequently becomes difficult to determine the elemental composition of a thin film comprising more than two elements with relatively close mass numbers. Difficulties also occur in the determination of light element compositions in heavier matrix materials if the signal from the light element is superimposed on the matrix signal. In such cases, it should be expected that a computer simulation method is the best way to derive quantitative and extensive information from the measured spectra.

In the present analysis, a very small ion dose was used to accumulate one spectrum because it minimizes irradiation damage during the measurement. Note that the dose was less than one-tenth of that under the standard RBS analysis conditions [29]. This problem resulted in the spectra showing low scattering yields (i.e., small signals) as presented in Figure 4.4. Even the signal from the Cd atoms may possess such a large statistical uncertainty that no more detailed result can be obtained by using it as measured. However, a quantitative interpretation of the RBS spectra is further required for a better understanding of the key problems such as the Cd migration.

The author describes here a computer simulation for calculating the concentration and depth distribution of Cd atoms from experimentally measured

RBS spectra (Figure 4.4). This may make it possible to distinguish the signal from the light elements, which is hidden in the statistical fluctuations of the Cd or substrate signal and is difficult to determine. The present method for generating a backscattering spectrum is very simple compared to other computer codes developed by previous studies [30-32]. More recently, sophisticated programs for computer simulations of backscattering spectra, such as RUMP [33], have also been published.

The program requires a database of atomic masses and stopping power values, and algorithms with which to generate them. The usual approach is to subdivide the sample into very thin layers of specified composition (Figure 4.5) and allow the program to follow the energy loss and scattering of the probing ions through successive layers. The detailed procedure and equations utilized for synthesis of backscattering spectra are described in many papers and textbooks [29-32]. Finally, the best fit to the raw spectrum was obtained by varying the parameters defining the depth profiles of the component elements.

To calculate the energy loss in compound specimens, the linear additivity of the stopping cross sections for the component, known as Bragg's rule, was then employed and, furthermore, constant stopping powers are assumed along the incident and exit paths. Generally, such a method, like the so-called surface energy approximation, is valid in the case that the penetration depth is confined to less than a few hundred nanometers since the stopping cross-section varies with beam energy. In this sense, it may be too rough to be reliable. It is considered that, however, this approximation is adequate and the introduced error is insignificant when it is used to characterize the surface region of the film. Note that the objective is to investigate the in-depth distribution of Cd atoms *near the front surface*, not to generate a realistic backscattering spectrum. For simplicity, the author also neglected the effect of isotopes and
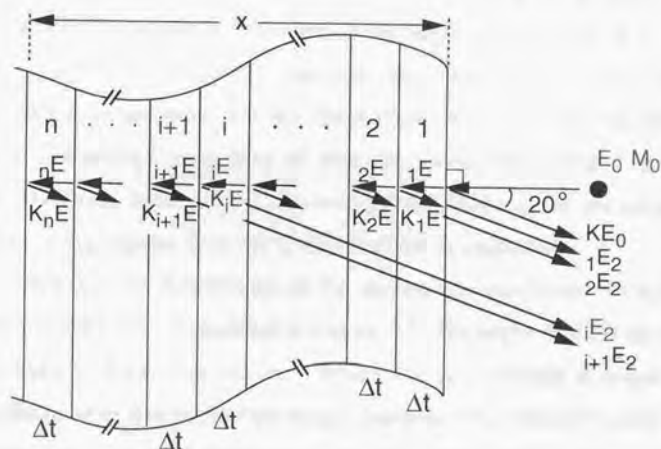
Figure 4.5. Schematic illustration of backscattering processes from the multielemental sample composed of n layers each of the same spatial thickness Δt. The analyzing beam (2 MeV He^{2+}) enters and leaves at 0° and 20° to the target normal, respectively. The beam energy at various stages of its progress through the solid is also shown.

the effects of statistical energy fluctuations due to the instrumental system resolution and energy straggling of penetrating ions.

Figure 4.6 shows the best fits to the experimental backscattering spectra (a) before and (b) after H_2S treatment. In these spectra, the calculated yields can be normalized to the experimental ones by multiplying by an appropriate constant. It was found that a difference in the depth profile near the Cd-edge was well reproduced. The deviation from the observed spectra is mainly ascribed to the assumption that the fluctuation effects due to the detector resolution and energy straggling of analyzing ions are excluded from the spectrum synthesis. Interestingly, this assumption results in the appearance of the backscattering signals from the C and O atoms in arachidate.

The concentration distribution of Cd atoms, on which each simulation spectrum was obtained, is depicted in Figure 4.7. The depth scale is shown by the areal density of Cd in atoms cm^{-2}, which can be converted to length units defining the number densities of the target elements. This naturally leads to the assumption that the overall thickness of the film, represented in atoms per unit area for each element, remained unchanged during the CdS formation (for example, 2.0×10^{16} atoms cm^{-2} for Cd). As mentioned in Section 4.3.1, there should be no significant loss of the component elements due to ion-beam exposure during the analysis, but the possible evaporation of organic components. Thus, this assumption seems quite reasonable.

As for the concentration profile before the H_2S treatment, the author assumes that it is kept constant at 9.8×10^{19} atoms cm^{-3} throughout the film (Figure 4.7 (a)). This was estimated from the value of 2×10^{-15} cm^2 for the surface area per arachidate molecule. On the other hand, as quantitatively found from Figure 4.7 (b), Cd atoms existing in the near-surface $< 3 \times 10^{15}$ atoms cm^{-2} depth migrated toward the substrate. The following question then comes
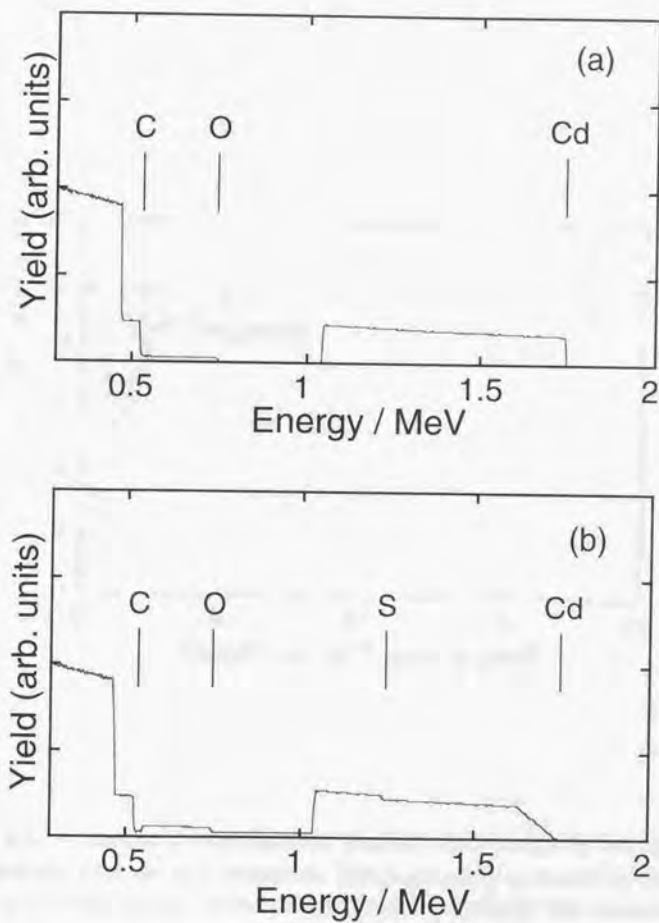
Figure 4.6. Simulated backscattering spectra from the cadmium arachidate LB films onto quartz (a) before and (b) after the H₂S treatment.
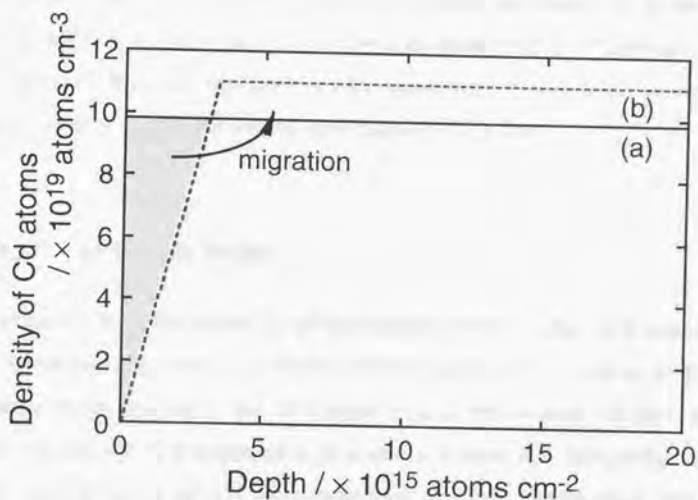
Figure 4.7. Calculated concentration profiles of Cd atoms in the films (a) before and (b) after the H_2S treatment. The depth scale is shown by the areal density of Cd because the number density cannot be defined. The concentration before the treatment was estimated from the deposition number (701) and the value of 2×10^{-15} cm^2 for the surface area per arachidate molecule. These profiles give the simulated backscattering spectra shown in Figure 4.6.

to mind: how do the Cd atoms displaced to a deeper area repopulate in the film? Of course, it is unlikely that they are uniformly distributed once again as shown in the calculated profile. The answer to this question, however, cannot be provided here due to the limitation of the present simulation; the calculation of the parameters was not perfect for deeper regions as already mentioned. More importantly, it appears from the present calculation that the migration suggested in the raw RBS spectrum involves the displacement of a large amount of Cd atoms widely distributed on the front surface of the film.

4.3.5. XPS Depth Profile

In order to check the reliability of the obtained RBS results, XPS was also used to investigate the depth distribution of the chemical composition in the films. Sputter depth profiles of the XPS peaks from a 701-layered LB film (a) before and (b) after the H_2S treatment is provided in Figure 4.8. Before the treatment, the peak intensity of Cd $3d_{5/2}$ remained constant throughout the Ar-ion sputtering (Figure 4.8 (a)). This suggests a uniform distribution of Cd atoms in depth, as easily predicted from the fact that the normal Y-type LB films were obtained in the present study. In contrast, from the in-depth distribution curve of the H_2S-treated film (Figure 4.8 (b)), the uniformity in the depth distribution was apparently broken after the reaction; the Cd atoms near the front surface of the film were seemingly moved to a lower area. In this sense, the depth profiles of Cd obtained by XPS seem to be consistent with the above RBS results, supporting the reliability of the present RBS analysis. Moreover, the depth distribution of the S 2p signal was similar to that of the Cd. This confirms that the Cd migration occurred together with the CdS formation.
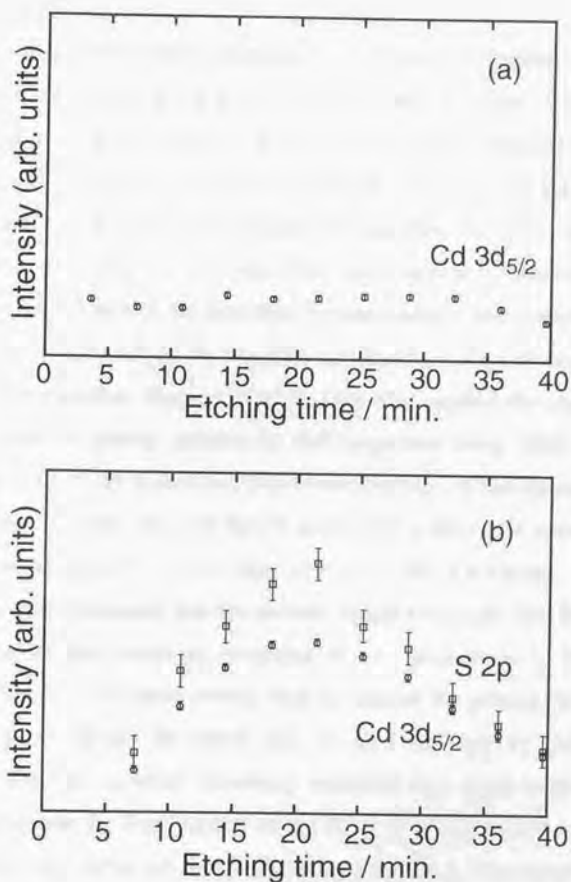
Figure 4.8. The intensity of XP Cd $3d_{5/2}$ peaks as a function of sputtering time for the 701-layered LB films (a) before and (b) after H_2S treatment. For the treated film, the profile of the S 2p peak intensity is also compared. These intensities were normalized against the sensitivity factors of individual elements. The data on the first several layers are omitted for the same reason as in Figure 4.3.

4.3.6. Morphology of the CdS Particles

The changes in the RBS spectra discussed in the previous sections undoubtedly indicate that the depth distribution of the Cd atoms in the film surface is disordered during the Q-sized CdS formation. Quite naturally, the same conclusion was brought by the above XRD results; almost all the diffraction peaks disappeared after the H_2S treatment. In fact, Pan et al. [12], in a study on the formation of CdS in stearic acid LB films, similarly observed a slight movement of metal ions in the direction perpendicular to the substrate, leading to an increase (a decrease) in the breadths (amplitudes) of the X-ray diffraction peaks after the reaction. Moriguchi et al. [10] also studied the change which occurred in the LB matrix induced by H_2S treatment using XRD and FT-IR spectroscopy; the X-ray diffraction peaks characteristic of the layered structure were significantly weakened, and the tilt angles of the fatty acid molecules were increased in conjunction with the Q-sized CdS formation. From this observation, they concluded that the particle formation caused the film-forming molecules to be less oriented, resulting in the destruction of the layered structure of the film. All these results seem to support the present findings.

However, it should be noted that, as also clarified by the spectrum simulations, the Cd migration seemingly occurred on a much larger scale; Cd atoms existing near the front surface might move to a deeper area across many organic molecules. Although the mechanisms for such a long-range migration are not yet clarified, it is obvious that many factors regarding the peculiarities of the author's samples, coupled with each other, would be related to this phenomenon. Two of these are described as follows: (i) Thick films composed of up to no less than 701 monolayers were prepared for the RBS analysis. This is because the *in-depth* distribution analysis of the samples was one of the main

objectives. If the RBS analysis had been carried out on thinner LB films, for example, of 100 monolayers or less, then one would have obtained a round peak instead of a flat profile due to the limited depth resolution of the instrumentation. As expected in the previous section, the film thickness possibly determines the time for completing the sulfidation reaction. There should be a long time interval for H_2S diffusion between the innermost and outermost layers in such thick films. (ii) It is also expected that the H_2S pressure has an important effect on the formation of the CdS microcrystallites. Indeed, in the above-mentioned study of Pan et al. [12], it was found that lower H_2S pressure weakened the destruction of the LB films. In the present case, on the contrary, the CdS particles were formed by the reaction with H_2S at atmospheric pressure. The H_2S treatment under the higher pressure should bring about considerable changes in the in-depth elemental distribution in the film.

Based on these discussions, it is unlikely that Q-sized CdS, being two-dimensional in nature, was formed in the well-ordered hydrophilic planes of the film. In other words, the CdS would be three-dimensionally aggregated. Smotkin et al. [9] also pointed out that their ellipsometric measurement did not exclude the possibility of large three-dimensional microcrystallites embedded in arachidic acid, while they suggested thin disk-like platelets of domains of CdS as an alternative to spherical particles, as already mentioned. Thus, it is reasonable to consider that spherical fine particles are generated in the film by the H_2S treatment in the present experiment. Asai et al. [34] previously estimated the dimension of CdS microcrystalltes incorporated into $CdAr_2$ LB films under the same conditions on basis of the assumption that spherical particles were formed. Their estimation uses the curve describing the absorption threshold as a function of the particle diameter proposed by Spanhel et al. [35]. They thus revealed that the diameters of the CdS particles are

comparable to (or larger than) the length of the AA molecule as shown in Figure 4.1 (b). It is concluded, therefore, that the formation of spherical CdS particles is followed by the destruction of the well-ordered structure of the host LB matrix.

4.4.   Conclusions

RBS was shown to be well suited for the characterization of LB films, and is particularly sensitive to the concentration-depth profile of the cations (metal atoms). The effect of ion-beam exposure during the analysis was insignificant enough to be ignored under the present irradiation conditions. The analysis confirmed the well-known fact that highly uniform LB films of $CdAr_2$ could be prepared with thickness regulated to a monolayer. The RBS signal of the films exposed to H_2S gave rise to a change in the Cd-edge. This spectral change was consistent with the result of the XPS in-depth analysis, indicating that the depth distribution of Cd atoms was disordered during the CdS formation. In conjunction with the simulation of the obtained backscattering spectra, it seemed to involve a long-range Cd migration towards a substrate during the CdS formation. It follows that the CdS microcrystallites produced in the films have a spheroidal morphology and do not exist in a two-dimensional disk form as has been suggested in previous reports. RBS can play an important role in the analysis of the structural changes in LB films accompanied by the formation of microcrystallites.

REFERENCES

[1] Y. Wang and N. Herron, *J. Phys. Chem.* **1991**, *95*, 525.

[2] A. Nakamura and T. Tokizaki, *Nonlinear Optics – Fundamentals, Materials and Devices*; Elsevier Science Publishers: Amsterdam, 1992.

[3] A. Eychmüller, A. Hässelbarth, L. Katsikas, and H. Weller, *Ber. Bunsenges. Phys. Chem.* **1991**, *95*, 79.

[4] Y. Wang and N. Herron, *J. Phys. Chem.* **1988**, *92*, 4988.

[5] A.I. Ekimov, Al.L. Efros, and A.A. Onushchenko, *Solid State Commun.* **1985**, *56*, 921.

[6] Y. Wang, A. Suna, W. Mahler, and R. Kosowski, *J. Chem. Phys.* **1987**, *87*, 7315.

[7] C. Petit, P. Lixon, and M.P. Pileni, *J. Phys. Chem.* **1990**, *94*, 1598.

[8] T.F. Towey, A.K. –Lodhi, and B.H. Robinson, *J. Chem. Soc. Faraday Trans.* **1990**, *86*, 3757.

[9] E.S. Smotkin, C. Lee, A.J. Bard, A. Campion, M.A. Fox, T.E. Mallouk, S.E. Webber, and J.M. White, *Chem. Phys. Lett.* **1988**, *152*, 265.

[10] I. Moriguchi, K. Hosoi, H. Nagaoka, I. Tanaka, Y. Teraoka, and S. Kagawa, *J. Chem. Soc. Faraday Trans.* **1994**, *90*, 349.

[11] R.S. Urquhart, C.L. Hoffmann, D.N. Furlong, N.J. Geddes, J.F. Rabolt, and F. Grieser, *J. Phys. Chem.* **1995**, *99*, 15987.

[12] Z. Pan, J. Liu, X. Peng, T. Li, Z. Wu, and M. Zhu, *Langmuir* **1996**, *12*, 851.

[13] Y.M. Lu, B.J. Wang, Z.P. Guan, L.C. Chen, A.H. Yang, W.S. Li, and X.W. Fan, *Proc. SPIE-Int. Soc. Opt. Eng.* **1994**, *2321*, 222.

[14] W. Nie, *Adv. Mater.* **1993**, *5*, 520.

[15] Y. Wang, *Acc. Chem. Res.* **1991**, *24*, 133.

[16] D.T. Amm, D.J. Johnson, T. Laursen, and S.K. Gupta, *Appl. Phys. Lett.* **1992**, *61*, 522.

[17] T. Laursen, G.R. Palmer, D.T. Amm, and D.J. Johnson, *Nucl. Instr. and Meth. B* **1993**, *82*, 125.

[18] D.J. Johnson, D.T. Amm, T. Laursen, and S.K. Gupta, *Thin Solid Films* **1993**, *232*, 245.

[19] M. Schurr, D. Brandl, Ch. Tomaschko, Ch. Scoppmann, and H. Voit, *Thin Solid Films* **1995**, *261*, 271.

[20] W.-K. Chu, J.W. Mayer, and M.-A. Nicolet, *Backscattering Spectrometry*; Academic Press: New York, 1978.

[21] A. Matsuda, M. Sugi, T. Fukui, S. Iijima, M. Miyahara, and Y. Otsubo, *J. Appl. Phys.* **1977**, *48*, 771.

[22] B.M.U. Scherzer, M. Wielunski, W. Möller, A. Turos, and J. Roth, *Nucl. Instr. and Meth. B* **1988**, *33*, 714.

[23] G.G. Ross and I. Richard, *Nucl. Instr. and Meth. B* **1992**, *64*, 603.

[24] R.S. Urquhart, D.N. Furlong, H.S. Mansur, F. Grieser, K. Tanaka, and Y. Okahata, *Langmuir* **1994**, *10*, 899.

[25] H.S. Mansur, F. Grieser, M.S. Marychurch, S. Biggs, R.S. Urquhart, and D.N. Furlong, *J. Chem. Soc., Faraday Trans.* **1995**, *91*, 665.

[26] A.S. Manocha and R.L. Park, *Appl. Surf. Sci.* **1977**, *1*, 129.

[27] D. Lichtman, T.H. Craig, Jr., V. Sailer, and M. Drinkwine, *Appl. Surf. Sci.* **1981**, *7*, 325.

[28] H. Chen, X. Chai, Q. Wei, Y. Jiang, and T. Lin, *Thin Solid Films* **1989**, *178*, 535.

[29] J.R. Bird and J.S. Williams, *Ion Beams for Materials Analysis*; Academic Press: Sydney, 1989.

[30] W.K. Chu and J.F. Ziegler, *J. Appl. Phys.* **1975**, *46*, 2768.

[31] J.F. Zeigler, R.F. Lever, and J.K. Hirvonen, *Ion Beam Surface Layer Analysis*; Plenum: New York, 1976.

[32] D.K. Brice, *Thin Solid Films* **1973**, *19*, 121.

[33] L.R. Doolittle, *Nucl. Instr. and Meth. B* **1992**, *64*, 603.

[34] K. Asai, K. Ishigure, and H. Shibata, *J. Lumin.* **1995**, *63*, 215.

[35] L. Spanhel, M. Haase, H. Weller, and A. Henglein, *J. Am. Chem. Soc.* **1987**, *109*, 5649.

CHAPTER 5

Fabrication of Diluted Magnetic Semiconductor Nanoparticles by Langmuir-Blodgett Technique

ABSTRACT

The first example of diluted magnetic semiconductor (DMS) fine particles incorporated into LB films is reported. $Cd_{1-x}Mn_xS$ (x = 0.45, 0.27, and 0.20) particles with about a 3-nm diameter were prepared through the reaction of arachidate LB films containing Cd and Mn with hydrogen sulfide (H_2S) in an atmosphere of NH_3. ESR measurements, before and after the H_2S treatment, provided information on the microstructural changes which occurred in the film during the particle formation. The anomalous broadening of the line shape and the anisotropic properties of quasi two-dimensional magnets were observed before the H_2S treatment, while after the H_2S treatment, these characteristic features completely disappeared, and a typical exchange-narrowed line arose. The drastic changes observed here indicate that $Cd_{1-x}Mn_xS$ fine particles were produced in a spherical shape, not in a two-dimensional platelet.

5.1.   Introduction

Diluted magnetic semiconductors (DMSs) are semiconducting crystals whose lattice is made up in part of substitutional magnetic ions. The magneto-optical experiments on this group of compounds revealed a number of interesting effects such as giant Faraday rotation, large Zeeman splitting of the carriers, enhanced g-values and bound magnetic polarons [1-4]. These result from the exchange interaction between the spins of the semiconductor carriers and the magnetic ions. Their ternary nature also makes it possible to tune the band parameters and lattice constants by varying the alloy composition.

If a low-dimensional structure in the DMS lattice is realized, it is expected that some of the above magneto-optical properties are more enhanced by the confinement of electronic states. Wang et al. [5] and Oka et al. [6,7] synthesized nanoparticles of $Zn_{1-x}Mn_xS$ and $Cd_{1-x}Mn_xTe$ in a glass matrix. Although their success opened a new and exciting area of research in both basic and applied physics, their methods involving energetic processes, such as heating or sputtering, are never employed in the preparation of nanoparticle systems containing organic components, since damage to the molecules cannot be entirely avoided. On the other hand, there have been few reports on the DMS nanoparticle systems prepared through a low-energy chemical process except for the study of Levy et al [8]. They synthesized $Cd_{1-x}Mn_xS$ nanocrystals by using reverse micelles as a microreactor and simultaneously controlled their size and composition. For further developing a synthetic methodology, the author independently focused on the well-known LB technique.

LB films not only offer the possibility of built-in architectural control at the monolayer level, they also provide useful media for the controlled

fabrication of quantum-sized (Q-sized) particles under very mild conditions [9-12]. In addition, if these highly ordered films contain magnetic ions, such as Mn^{2+}, in their interlayers, they can be considered as a "two-dimensional magnetic system", whose existence was experimentally proved by Pomerantz and co-workers [13]. Based on their ESR experiments [13-16] on sheets of manganese (II) stearate ($MnSt_2$) bilayers, prepared by adding two layers of $MnSt_2$ to a single layer of $CdSt_2$ using the LB technique, the basic ESR properties of two-dimensional magnetic structures were verified.

In this chapter, the author reports the first successful fabrication of $Cd_{1-x}Mn_xS$ fine particles in LB films. In addition to the detailed preparation procedures, he describes an ESR study on the prepared films. The ESR spectral features, such as the line shape and the resonance linewidth, provided information on the Mn dispersity and dimensionality of the spin system. Based on the spectral difference before and after particle formation, the mechanisms of particle growth, as well as the morphology of the formed particles, were discussed.

5.2. Experimental Details

Manganese(II) chloride ($MnCl_2$) purchased from Nacalai Tesque, Inc. was a guaranteed grade reagent and used as supplied. The other materials used in the present experiments were already described in Section 4.2.1.

The method of synthesis is analogous to that used by Smotkin et al. [9] for incorporation of cadmium sulfide (CdS) particles into LB films. In the first step, LB films of Cd and Mn arachidates were obtained by depositing the Cd/Mn

mixed monolayers. The precursor monolayers were prepared by spreading a 1 $\times$ 10^{-3} mol dm^{-3} arachidic acid solution in chloroform onto subphase water containing CdCl$_2$/MnCl$_2$ (4.0×10^{-4} mol dm^{-3} in total) and NaHCO$_3$ (5.0×10^{-5} mol dm^{-3}). The spread monolayer, compressed to 30 mNm^{-1}, was transferred to a quartz substrate by the conventional vertical dipping technique. Although, as reported in various cases [17,18], the Cd- and Mn-salt formations were almost complete at the appropriate pH, the relative concentration of Mn^{2+}, exchanged with carboxylate protons of the arachidic acid, is not the same as that of the subphase. This is because the stability constant of the complex forming with fatty acids will vary with metal ions. The metal-ion composition of the film was, therefore, established by a chemical quantitative analysis; colorimetry determined the concentration of each ion in a solution prepared by dissolving the film in 0.1 mol dm^{-3} HCl. In the second step, the diffusion of hydrogen sulfide (H$_2$S) restores the arachidic acid and yields metal sulfide in the LB matrix. Empirically, manganese sulfide (MnS) crystallizes through the reaction of Mn salts with H$_2$S in the presence of NH$_3$. Thus, the preformed arachidate LB films in a sealed system were exposed to the H$_2$S-NH$_3$ mixed gas at room temperature for a specified time.

X-ray photoelectron spectrometry (XPS) was recorded using a Shimadzu ESCA 850 spectrometer. A Mg (1253.6 eV) X-ray source was operated at 8 kV and 240 W. UV-vis spectra were recorded using a Hitachi U-3200 spectrophotometer in the transmission mode. ESR measurements at room temperature were performed with the aid of the JES-TE200 spectrometer at the National Institute of Radiological Science. All the spectra were measured in the first harmonic mode.

5.3.   Results and Discussion

5.3.1.   Syntheses and Control of the Composition

As mentioned in the experimental section, the relative concentration of Mn^{2+} in the LB films is generally different from that in the subphase, because the amount of each ion therein is exclusively regulated by the complexation with carboxylate groups. Figure 5.1 shows the result of a chemical quantitative analysis; a correlation between the Mn ratio in the films and that in the subphases over the wide concentration range of Mn. Obviously in Figure 5.1, the ion exchange of Cd^{2+} with carboxylate sites was found to be dominant over that of Mn^{2+} onto the subphases at every Mn concentration. This figure also confirms that the Mn mole fraction in the film, which is equal to x in $Cd_{1-x}Mn_xS$ as described below, can be arbitrarily controlled by varying the ratio of Mn^{2+} to Cd^{2+} in the subphase. In the present case, the author deposited the LB films over the subphases of Mn/Cd 9/1, 7/3, and 5/5 mixtures, and thus obtained the films containing Mn at relative concentrations of 0.45, 0.27, and 0.20, respectively.

Before and after the H_2S treatment, 21-layer films supported on quartz were analyzed by XPS. The S 2p signal peaked at about 161.5-162.0 eV in the H_2S-treated samples as typically shown in Figure 5.2. Manocha et al. [19] and Lichtman et al. [20] suggested that a peak in this range was associated with the sulfur in the sulfide configuration. No difference in binding energies was recognized in the Mn $2p_{3/2}$ spectra of the film samples before and after the H_2S treatment and in the reference materials (manganese arachidate and MnS-bearing multilayers). Moriguchi et al. [11,12] previously reported that the Cd $3d_{5/2}$ signal was observed at 405.6 eV and that the binding energy was the same
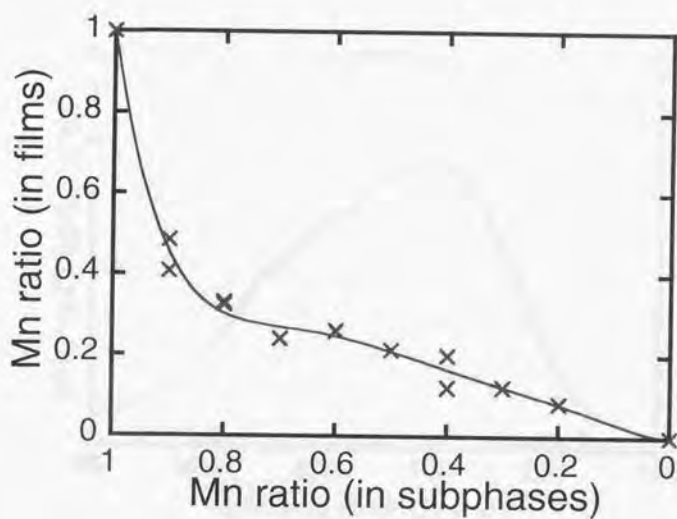
Figure 5.1. A plot of correlation between Mn ratio in films and that in subphases over the wide Mn concentration range. The solid line represents the result of the polynomial curve fit.
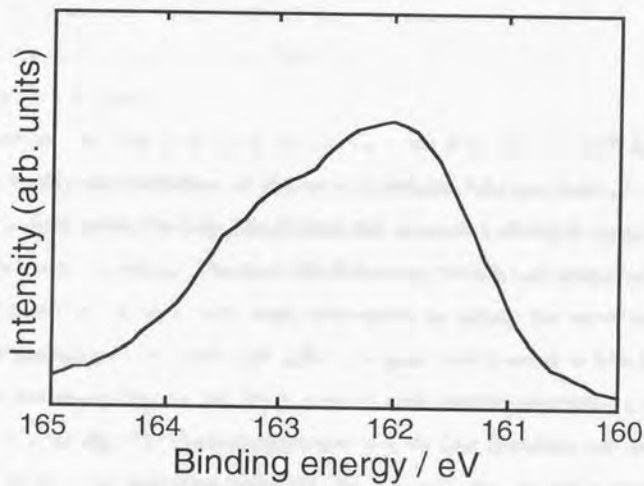
Figure 5.2. Representative S 2p XP spectrum of 21-layered arachidate LB films containing Mn at a concentration of x = 0.27 after exposure to H₂S.

in both cadmium arachidate and CdS. These identical binding energies of Mn and Cd mean that the chemical states cannot be identified by XPS. On the other hand, quantitative XPS analysis gives the available information, as they also proposed. In all the samples the atomic ratios of metal components to sulfur in the sulfide configuration, $(Cd + Mn)/S$, were almost unity, consistent with the stoichiometry of $Cd_{1-x}Mn_xS$. Therefore, the results obtained here seem to suggest the formation of CdS-MnS solid solutions, in other words, homogeneous $Cd_{1-x}Mn_xS$.

However, only the $(Cd + Mn)/S$ atomic ratio detected by XPS does not directly identify the formation of the solid solutions. Unexpectedly, it is very difficult to distinguish the $Cd_{1-x}Mn_xS$ from the separate CdS/MnS using any of the spectroscopic methods. The pure MnS-bearing multilayers prepared as the reference materials show a very weak absorption in almost the same range as that of the particles under study (the inflection point was located at 340-360 nm as will be shown in Chapter 6). Thus, even if each sulfide separately coexists, the relatively strong UV-Vis transition due to CdS fine particles can interfere with the absorption spectrum of MnS. As a result, the separate formation cannot be identified by an optical absorption measurement. In the luminescence spectra of the mixed Cd-Mn-S system, the emission originating from both the intrinsic Mn^{2+} state and the defect site of Cd atoms is expected to appear around 600 nm [4,21]. In fact, the previous observation for all the specimens confirmed that the 600-nm emission band was very broad, indicating an overlap of the two emission bands [22]. This means that luminescence is also of no use for identification of the sulfide-precipitation type in the present samples.

Generally, the X-ray diffraction (XRD) measurement is a powerful method for studying the order structure of solid solutions or the alloys of semiconductors. Based on the lattice parameter obtained from the XRD

patterns, the author expected the determination of the crystalline phases in the generated particles. The XRD measurement of the microcrystallites in an organic matrix (especially ultra-thin films such as LB multilayers), however, is nearly impossible because of its small fraction. The patterns for the much thicker films of more than several hundred monolayers might be taken with a step-scanned diffractometer and long exposure times. Even if the measurement is achieved, the data never contribute to the discussion in this chapter. This is because the degree of molecular ordering in such thick films is quite different from that in the thinner films prepared in the present study.

As for the nanoparticles of metal-sulfide ternary semiconductors, co-colloids of CdS and ZnS were produced by simultaneous precipitation of the two metal ions in aqueous solution [24]. Relatively easy incorporation of Zn^{2+} into CdS would be rationalized by considering the fact that both CdS and ZnS show the zinc blende or wurtzite structures. On the other hand, in the present case, the component binary semiconductors show the different crystal structures; unlike CdS, MnS crystallizes in either rocksalt or NiAs type structures. Thus, it is considered that the incorporation of Mn^{2+} into CdS is not very easy compared to the CdS-ZnS system. Nevertheless, as already mentioned, $Cd_{1-x}Mn_xS$ nanoparticles were synthesized through a conventional chemical process, such as coprecipitation in reverse micelles [8]. This latter research supports the conclusion that $Cd_{1-x}Mn_xS$ alloys are formed in the LB film.

The following facts are also likely to justify this conclusion. The Mn ions in the H_2S-untreated samples are considered to be well isolated and dispersed enough to indicate a broad signal in their ESR spectra (shown later in spectrum (a) of Figure 5.4). Furthermore, concerning the synthesis of metal sulfide particles by the LB technique, Moriguchi et al. [12] described that four types of

sulfide formations were expected in principle if mixed metal ions (M^{2+} and N^{2+}, for example) were in the interlayers of an LB film. According to their description, as one of these types, the formation of homogeneous $M_{1-x}N_xS$ is expected if MS and NS form a solid solution that is thermodynamically stable. It is widely known that CdS makes stable solid solutions of $Cd_{1-x}Mn_xS$ with MnS up to $x = 0.45$-0.50 [23]. Thus, in the present case, the formation of $Cd_{1-x}Mn_xS$ instead of separate CdS and MnS is more conceivable, although the chemistry involved in the $Cd_{1-x}Mn_xS$ formation in the LB matrix seems to be rather complicated as compared with the formation through other preparation processes such as sputtering. Accordingly, it would be fair to say that fine particles of $Cd_{0.55}Mn_{0.45}S$ ($x = 0.45$), $Cd_{0.73}Mn_{0.27}S$ ($x = 0.27$), and $Cd_{0.80}Mn_{0.20}S$ ($x = 0.20$) are produced in the preformed LB films (see above).

5.3.2. Optical Absorption for Estimation of the Particle Size

Because of the quantum size effects of semiconductor nanoparticles, the UV-vis spectroscopy has become a powerful method to determine their sizes. In the absence of an applied magnetic field, DMSs are known to behave essentially the same as their host counterparts, although their band gaps vary with x. Thus, according to the method used in the case of CdS particles, the author calculated the mean $Cd_{1-x}Mn_xS$ particle sizes of the present samples from the energy shifts in the absorption threshold. The band gap energy, E_g, in bulk crystals of $Cd_{1-x}Mn_xS$ was determined on the basis of a curve describing E_g as a function of x, which was the result of a previous study [25]. As predicted by the simple three-dimensional confinement model based on the effective mass

approximation, the energy of the lowest exciton state in the microcrystallites of radius R ($R \leq a_B$, where a_B is the exciton Bohr radius) is given by

$$E_{ex}(R) = E_g + h^2 / 8\mu R^2 - 1.8e^2 / \varepsilon R, \qquad (5.1)$$

where μ and ε are the reduced mass of the exciton and the dielectric constant of the microcrystallites, respectively [26].

The exposure to H_2S gas gave rise to the appearance of an optical absorption due to $Cd_{1-x}Mn_xS$ as presented in Figure 5.3. The wavelength of an absorption threshold was blue-shifted from the bulk crystal, which is indicative of the quantum confinement effect. The samples, however, showed a gentle slope around the threshold in the absorption spectra, suggesting that they have a wide size distribution. Therefore, according to the method of Spanhel et al. [27], the author took as the threshold the inflection point of the absorption spectrum. The inflection points of the samples of x = 0.45, 0.27, and 0.20 were 320-340 nm, 360-380 nm and 350-370 nm, respectively. These wavelengths correspond to particles of 2.9-3.0 nm, 3.0-3.2 nm, and 2.9-3.0 nm in diameter, respectively. Considering the large uncertainties in the size determination, the author proposed that $Cd_{1-x}Mn_xS$ particles with a diameter of about 3 nm were obtained in the present study.

5.3.3. ESR Characterization of $Cd_{1-x}Mn_xS$ Nanoparticles

The magnetic interaction of Mn^{2+} incorporated in LB films can be classified as spin-spin and hyperfine interactions. The former gives a single, relatively broad, band spectrum and the latter gives six well-resolved hyperfine lines. The ESR spectra of the H_2S-untreated samples (51 layers) showed a single, broad signal. This observation, in agreement with the results of Pomerantz et al. [15] and
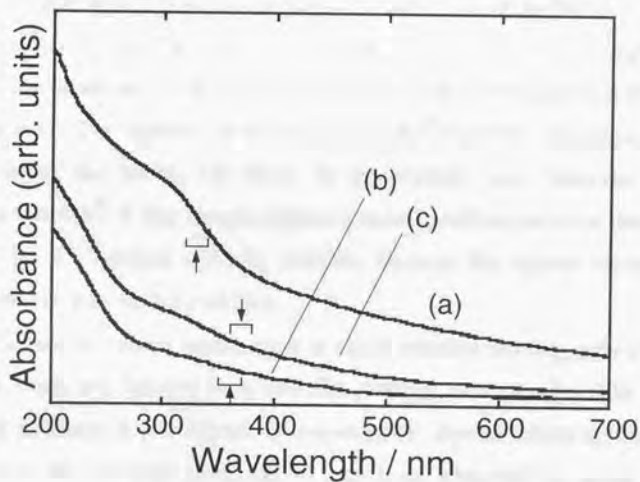
Figure 5.3. Absorption spectra of $Cd_{1-x}Mn_xS$ nanoparticles prepared in LB films with x = (a) 0.45, (b) 0.27, and (c) 0.20. The arrows mark the threshold wavelength on each spectrum.

Takamura et al. [28] for LB films of pure Mn salts, suggests that the Mn-Mn (i.e., spin-spin) interaction in the films is very strong. In addition to such a broad signal, only the x = 0.20 sample (Figure 5.4 (a)) has a weak hyperfine structure due to a coupling between the unpaired electrons and the ^{55}Mn nucleus (I = 5/2). Although the hyperfine lines, which in general, appear for single crystals doped with Mn^{2+}, were similarly observed for the Mn arachidate LB films by Takamura et al. [28], it was rather unusual to find a hyperfine structure in the broadened ESR signal, as they also stated. Pomerantz et al. [15] and Bonosi et al. [29] reported little trace of the Mn^{2+} hyperfine structure in the ESR spectra of the $MnSt_2$ LB films. In the present case, however, it is conceivable that Mn^{2+} in this sample might be isolated and dispersed in the same manner as the Mn^{2+}-doped crystals, possibly because the largest amount of Cd^{2+} coexisted in the microcrystallites.

The ESR measurement enables one to check whether the magnetic ions in the present films are located in a two-dimensional arrangement. The two-dimensional structure is manifested by characteristic dipolar anisotropy effects in both linewidth and line positions. It has been observed in quasi two-dimensional magnets that the ESR linewidth is of the form

$$\Delta H \approx a + b \, (3 \cos^2 \theta - 1)^2 \qquad (5.2)$$

where θ is the angle between the applied field and the normal to the film. Richards and Salamon [30] suggested a theory of these angular dependences on the basis of the dipolar interactions in a two-dimensional array.

Figures 5.5 (A), (B), and (C) display the angular variation of the ESR linewidth for x = 0.45, 0.27, and 0.20, respectively, and compare the spectra before (a) and after (b) the H_2S treatment. The author attempted to fit the observed dependence not with equation (2), but with the equation which Pomerantz et al. [16] had rederived from the theory of Cheung and Soos [31].
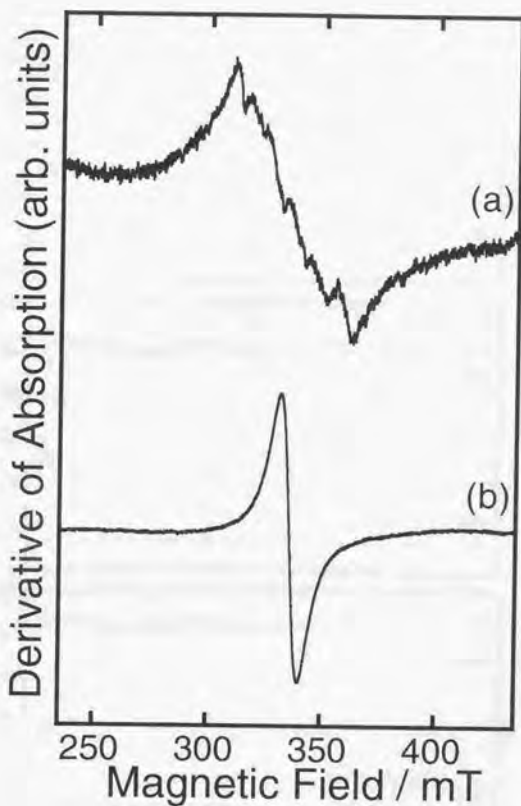
Figure 5.4. Typical ESR spectra of the arachidate LB films with 51 layers containing Mn at a concentration of x = 0.20. The measurements at room temperature were carried out at a θ = 60° configuration on the H$_2$S-untreated (a) and the treated (b) samples.
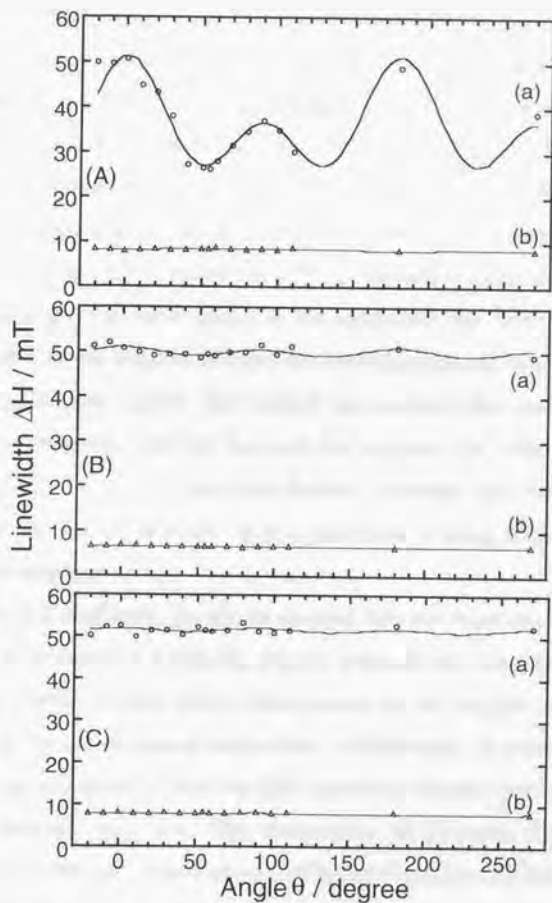
Figure 5.5. The angular variation in the resonance linewidth of ESR spectra from the arachidate LB films with 51 layers containing Mn at concentrations of (A) x = 0.45, (B) 0.27, and (C) 0.20. The spectra in each figure were obtained for the H_2S-untreated (a) and the treated (b) samples at room temperature. Theoretical curves (solid line) were fitted to the experimental data.

As for the H_2S-untreated sample, although metal ions therein are believed to form a two-dimensional array, the characteristic angular dependence of a two-dimensional array was observed only for the sample at the maximal Mn concentration, $x = 0.45$ (curve (a) in Figure 5.5 (A)). On the other hand, in the case of the lower Mn content, i.e., $x = 0.27$ and 0.20, the ESR absorption was isotropic with the linewidth in the orientation, as given by the randomly dispersed paramagnetic centers, shown in curves (a) of Figures 5.5 (B) and (C). Bonosi et al. [29] studied the ESR properties of LB films, which were prepared using mixed monolayers of Mn arachidate and methylarachidate, and found a limit to the Mn-Mn distance for two-dimensional magnetic properties. According to their report, the author can explain the above findings by considering the mean distance between the in-plane Mn^{2+} ions. In the samples of $x = 0.27$ and 0.20, the average distance between the Mn^{2+} ions is large enough to prevent in-plane spin-spin interactions, leading to the disappearance of the anisotropies.

After H_2S treatment, the above spectral features were drastically changed. In curve (b) of Figure 5.5 (A), the angular dependence completely disappeared. This undoubtedly means that a deterioration of the regular layered structure destroys the two-dimensional magnetism. Additionally, it was also found from spectrum (b) of Figure 5.4 that the ESR linewidth became very sharp compared to the untreated specimen. The sharpening of the line is referred to as "exchange narrowing". These spectral changes indicate that the formation and the growth of $Cd_{1-x}Mn_xS$ particles result in the destruction of the two-dimensional structure, leading to the enhancement of exchange interactions.

Similar observations have been also reported in previous studies. As was also cited in Chapter 4, Moriguchi et al. [11] studied the change, which occurred in LB films of $CdSt_2$ induced by H_2S treatment, using XRD and FT-

IR spectroscopy; the X-ray diffraction peaks characteristic of the layered structure were considerably weakened, and the tilt angles of the fatty acid molecules were increased in conjunction with the formation of the CdS particles. Based on this, they postulated that the particle formation caused the film-forming molecules to be less oriented, resulting in the destruction of the layered structure of the film. Quite recently, the author observed, based on Rutherford backscattering spectrometry (RBS) measurements of the H_2S-untreated and treated Cd arachidate films, that the Cd^{2+} in the film migrated toward the substrate after H_2S treatment [32] (see Chapter 4). Based on these findings, including the present one, it is concluded that $Cd_{1-x}Mn_xS$ particles in the film were aggregated in a spherical form, not as a two-dimensional platelet.

5.4. Conclusions

The author demonstrated, for the first time, the fabrication of $Cd_{1-x}Mn_xS$ microcrystallites using the LB technique which involves a wet, low-energy process. The sample preparation was modified from that used for preparing binary CdS particles; the preformed LB films of Cd and Mn arachidate were reacted with H_2S and NH_3. Characterization by chemical quantitative analysis, XPS and absorption spectroscopy confirmed that the author obtained 3-nm diameter particles of $Cd_{1-x}Mn_xS$, where the Mn fraction, x, can be arbitrarily controlled by varying the Mn/Cd ratio in the subphases. The author also measured the ESR spectra of H_2S-untreated and H_2S-treated samples, and then examined the microstructure changes which occurred in the LB matrix during particle formation. Before H_2S treatment, the author found a single, broad signal

in the spectra of all the samples tested so far. Additionally, the angular dependence of the resonance linewidth characteristic of two-dimensional magnetic systems was observed, but only for the film which contained Mn^{2+} at the maximal concentration ($x = 0.45$). In contrast, after H_2S treatment, these characteristic features completely disappeared, and a typical exchange-narrowed line arose. These findings indicate that, as also expected from the previous reports, the highly ordered two-dimensional structure was destroyed by the formation of $Cd_{1-x}Mn_xS$ microcrystallites in a spherical shape, rather than in a two-dimensional thin platelet.

REFERENCES

[1] J.K. Furdyna, *J. Appl. Phys.* **1982**, *53*, 7637.

[2] J.K. Furdyna, *J. Appl. Phys.* **1988**, *64*, R29.

[3] J.K. Furdyna and J. Kossut, *Semiconductors and Semimetals, Vol. 25, Diluted Magnetic Semiconductors*; Academic Press: New York, 1988.

[4] M. Jain, *Diluted Magnetic Semiconductors*; World Scientific: Singapore, 1991.

[5] Y. Wang, N. Herron, K. Moller, and T. Bein, *Solid State Commun.* **1991**, *77*, 33.

[6] K. Suzuki, M. Nakamura, I. Souma, K. Yanata, and Y. Oka, *J. Crystal Growth* **1992**, *117*, 881.

[7] K. Yanata, K. Suzuki, and Y. Oka, *J. Appl. Phys.* **1993**, *73*, 4595.

[8] L. Levy, J.F. Hochepied, and M.P. Pileni, *J. Phys. Chem.* **1996**, *100*, 18322.

[9]   E.S. Smotkin, C. Lee, A.J. Bard, A. Campion, M.A. Fox, T.E. Mallouk, S.E. Webber, and J.M. White, *Chem. Phys. Lett.* **1988**, *152*, 265.

[10] D.N. Furlong, R. Urquhart, F. Grieser, K. Tanaka, and Y. Okahata, *J. Chem. Soc., Faraday Trans.* **1993**, *89*, 2031.

[11] I. Moriguchi, I. Tanaka, Y. Teraoka, and S. Kagawa, *J. Chem. Soc., Chem. Commun.* **1991**, 1401.

[12] I. Moriguchi, H. Nii, K. Hanai, H. Nagaoka, Y. Teraoka, and S. Kagawa, *Colloids and Surfaces A* **1995**, *103*, 173.

[13] M. Pomerantz, *Solid State Commun.* **1978**, *27*, 1413.

[14] M. Pomerantz, F.H. Dacol, and A. Segmüller, *Phys. Rev. Lett.* **1978**, *40*, 246.

[15] M. Pomerantz and A. Segmüller, *Thin Solid Films* **1980**, *68*, 33.

[16] F. Ferrieu and M. Pomerantz, *Solid State Commun.* **1981**, *39*, 707.

[17] S. Bettarini, F. Bonosi, G. Gabrielli, and G. Martini, *Langmuir* **1991**, *7*, 1082.

[18] G. Gabrielli, M. Puggelli, E. Ferroni, G. Carubia, and L. Pedocchi, *Colloids Surf.* **1989**, *41*, 1.

[19] A.S. Manocha and R.L. Park, *Appl. Surf. Sci.* **1977**, *1*, 129.

[20] D. Lichtman, T.H. Craig, Jr., V. Sailer, and M. Drinkwine, *Appl. Surf. Sci.* **1981**, *7*, 325.

[21] Y. Wang and N. Herron, *J. Phys. Chem.* **1988**, *92*, 4988.

[22] T. Yamaki, T. Yamada, K. Asai, K. Ishigure, and H. Shibata, *Thin Solid Films* **1998**, *327-329*, 581.

[23] R.O. Miller, F. Dachille, and R. Roy, *J. Appl. Phys.* **1966**, *37*, 4913.

[24] A. Henglein and M. Gutiérrez, *Ber Bunsenges. Phys. Chem.* **1983**, *87*, 852

[25] M. Ikeda, K. Itoh, and H. Sato, *J. Phys. Soc. Jpn.* **1968**, *25*, 455.

[26] L.E. Brus, *J. Chem. Phys.*, **1984**, *80*, 4403.

[27] L. Spanhel, M. Haase, H. Weller, and A. Henglein, *J. Am. Chem. Soc.* **1987**, *109*, 5649.

[28] T. Takamura, K. Matsushita, and Y. Shimoyama, *Jpn. J. Appl. Phys.* **1996**, *35*, 5831.

[29] F. Bonosi, G. Gabrielli, and G. Martini, *Colloids and Surface A* **1993**, *72*, 105.

[30] P.M. Richards and M.B. Salamon, *Phys. Rev. B* **1974**, *9*, 32.

[31] T.T.P. Cheung and Z.G. Soos, *J. Chem. Phys.* **1978**, *69*, 3845.

[32] T. Yamaki, K. Asai, and K. Ishigure, *Chem. Phys. Lett.* **1997**, *273*, 376.

CHAPTER 6

Ion Irradiation Effect on Surface Electronic States in Semiconductor Fine Particles Incorporated into Langmuir-Blodgett Films

ABSTRACT

The author successfully prepared cadmium sulfide (CdS) fine particles with different dimensions in Langmuir-Blodgett (LB) films, and then examined the ion irradiation effect on their surface electronic states. Based on in-situ observations of the emission induced by a 1.0 MeV H^+ bombardment, the ion irradiation was found to decrease the intensity of the lower-energy emission without any aggregation and decomposition of the particles. This clearly shows that the irradiation will remove almost all the traps within the band gap and provide good surface passivation to the CdS particles. The adaptability of such a surface-treatment technique with high-energy ions to $Cd_{1-x}Mn_xS$ and MnS fine particles was also demonstrated. These irradiation effects appeared to be prominent in the fine-particle systems whose S/V ratio is much larger than that of the bulk crystals.

6.1.   Introduction

In recent years, there has been considerable interest in quantum-sized (Q-sized) semiconductor particles, whose dimension is smaller than that of the Wannier exciton. The most characteristic feature of the Q-sized semiconductor particles compared with the bulk is revealed in the electronic structure, that is, the blue-shifted absorption threshold and the discrete electronic levels [1-5]. This so-called quantum size effect can be potentially exploited in a broad variety of applications [6]. So far, the nonlinear optical property of Q-particles, which will be discussed in the next chapter, has been actively investigated in view of optoelectronic devices.

Such applications will always require that the particles be chemically stable and monodispersed. Well-controlled synthetic methods are indispensable to these requirements, because Q-sized particles are inherently liable to aggregate or grow, thus reducing the surface energy. One promising approach to synthesizing well-defined particles involves their formation in Langmuir-Blodgett (LB) films [7-10]. The use of LB film matrices is particularly suitable for practical device construction since this technique allows the particles to be arranged with constant interparticle distances as multilayers.

When the particle dimensions are reduced, an additional effect becomes increasingly important: the ratio of surface area to volume significantly increases. This effect is compounded by the irregular nature of the surface, where dangling bonds or defects act the part of traps for electrons and holes. Various localized states in the midgap originating from the surface irregularity complicate the dynamics of the photogenerated charge carriers in the small particles. The emission quantum yield of such fine particles is only a few

percent [11] indicating that the principal decay process is nonradiative. Thus, controlling the surface states is absolutely essential both for a better understanding of the emission mechanism and for the practical applications of Q-sized particles. Previous papers reported that excitonic emissions were enhanced by chemical modification of the particle surface [11]. Recently, quantum yields of nearly 1 at room temperature were achieved by size separation of the surface-modified particles using gel electrophoresis [12,13].

Ion beams with energies in the MeV range have been used extensively for material modification as well as elemental or structural analysis, because they can focus a huge energy on the target materials in a highly concentrated form compared with the other ionizing beams. For example, the electronic structure of materials is modified through radiation-enhanced short range ordering, clustering, precipitation, and self-diffusion [14,15]. Therefore, it has been a strong motivation for the author to use ion irradiation in order to control the midgap states of the Q-sized particle.

This chapter describes the effects of ion beam irradiation on the surface electronic states of cadmium sulfide (CdS) fine particles incorporated into LB films. To probe the changes in the surface states, the author used in-situ observations of the emission induced by the ion bombardment. In addition, the author adopted two different fine-particle systems, the microcrystallites of $Cd_{1-x}Mn_xS$ and MnS, and then investigated what effect the ion irradiation has on their surface electronic states. The former material, generally referred to as a Q-sized diluted magnetic semiconductor (DMS) particle, contains magnetic ions, Mn^{2+}, in the cation sites of host CdS. The present investigation enables one to collect information about the adaptability of the surface-modification technique with high-energy ions. Finally, it has turned out that the surface-treatment effect due to the ion irradiation is especially prominent in the fine

particles as compared with the corresponding bulk crystals. This is discussed in connection with the difference in the surface-to-volume ratio of the number of atoms between the fine particles and the bulk crystals.

6.2.   Experimental Section

6.2.1.   Sample Preparation

CdS fine particles were synthesized according to the method of Smotkin et al. [7]. It involves the reaction of cadmium arachidate $(C_{19}H_{39}COO)_2Cd$, which is formed in multilayers on solid substrates in ambient hydrogen sulfide (H_2S). The $(C_{19}H_{39}COO)_2Cd$ LB films were constructed under the following conditions: (i) surface pressure: 35 mNm^{-1}, (ii) the constituents of subphase water on which the monomolecular film was spread: CdCl$_2$ $(4.0 \times 10^{-4}$ mol dm^{-3}) and NaHCO$_3$ $(5.0 \times 10^{-5}$ mol dm^{-3}), and (iii) the solution spread over the subphase: $C_{19}H_{39}COOH$ in chloroform $(1 \times 10^{-3}$ mol dm^{-3}). For each sample, the number of monolayers deposited on one side of the substrate was 149. The H_2S treatment of the transferred film was carried out under two different conditions: at room temperature and at 80 °C, which is slightly above the melting point of $C_{19}H_{39}COOH$ (75.5 °C). When prepared at 80 °C, the sample was heated for several hours before the reaction. For the more detailed procedures, including the materials used in the present experiments, Section 4.2.1 should be reviewed.

The method used for fabricating fine particles of $Cd_{1-x}Mn_xS$ and MnS was analogous to that for CdS (mentioned above) with the following exceptions: (i) surface pressure: 30 mNm^{-1}, (ii) the subphase for arachidate monolayers: the

$MnCl_2/CdCl_2$ 1/1 mixture or pure $MnCl_2$ (4.0×10^{-4} mol dm^{-3} in total) with 5.0×10^{-5} mol dm^{-3} $NaHCO_3$, and (iii) the H_2S treatment in the presence of NH_3. The details concerning the preparation and characterization of $Cd_{1-x}Mn_xS$ particles has already been described throughout Chapter 5. According to this description, it is concluded that $Cd_{0.80}Mn_{0.20}S$ particles with about a 3-nm diameter were prepared under the present experimental conditions. As for the MnS particles, their size could not be estimated from their absorption spectrum, whose inflection point was located at 340-360 nm (result not shown). This is because, as far as the author knows, there has been little previous data on the semiconducting properties of the corresponding bulk crystals, such as the carrier effective masses.

Commercially-available CdS and MnS powders were supplied as bulk samples. Their grain sizes, whose measurement was attempted using scanning electron microscopy, were large enough (a few micrometers) to be considered in the "bulk crystal" range. The cast films of the powders dispersed in organic solvents were used for the irradiation experiments.

The author employed Si and quartz as the substrates for film preparation. The quartz plate was used only for absorption measurements to estimate the size of the fine particles.

6.2.2.　Measurements

Optical absorption measurements for estimation of the particle size were conducted using a Hitachi U-3200 UV-Vis spectrophotometer.

The samples in a vacuum chamber ($< 10^{-5}$ Pa) were irradiated by 1.0 MeV protons (H^+) from the Van de Graaff accelerator of the Research Center for

Nuclear Science and Technology, the University of Tokyo. In-situ observation of the high-energy-ion-induced emission was performed with the system illustrated in Figure 3.1. Emission from the samples during irradiation was detected by an optical multichannel analyzer (OMA), USP-600, produced by Unisoku Co. This system can detect photons in the range of 200-800 nm. In the present measurements, the beam current density was 52.0 nA cm^{-2}. Each emission spectrum was obtained by accumulating the signals detected over a 50 s period. In these spectra, the signals whose amplitude was less than 0.06% of full scale were ignored, based on the preliminary estimation of S/N. The wavelength resolution, depending on the slit width, was about 8 nm. The details of this measurement were also reported in Section 3.2 and elsewhere [16].

6.3.   Results and Discussion

6.3.1.   Absorption and Size of CdS Fine Particles

Figure 6.1 shows the UV-Vis absorption spectra of CdS particles in LB films prepared at (a) room temperature and (b) 80 °C. The spectra showed a very gentle slope around the absorption threshold. This caused uncertainties in determination of the threshold corresponding to the band gap. The gentle slope indicates that the samples have a wide distribution of sizes. Thus, the author took the inflection point of the absorption spectrum as the threshold, as adopted by Spanhel et al. [17]. In Figure 6.1 samples (a) and (b) show the absorption threshold at 420-440 nm and at 460-480 nm, respectively. It was found that the former has a mean diameter of 3.0-3.4 nm while the latter has a 4.1-5.0 nm
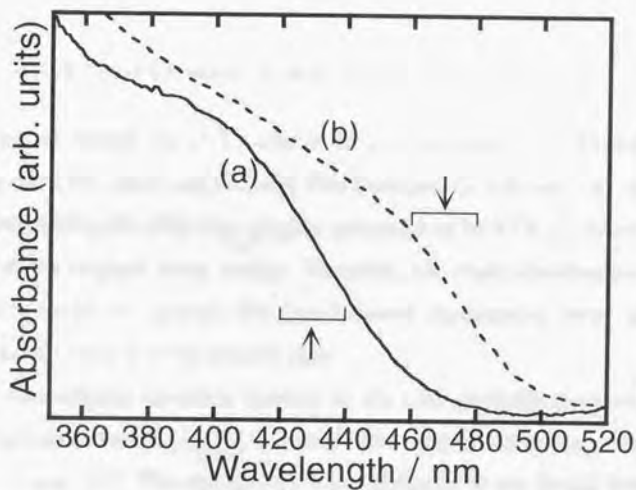
Figure 6.1. Absorption spectra of CdS fine particles prepared in LB films at (a) room temperature and (b) 80 °C. The arrow marks the threshold wavelength on each spectrum.

diameter based on the curve describing the threshold as a function of the particle diameter proposed by Spanhel et al. [17]. From this result, the author suggests that two kinds of particles with different sizes were acquired by varying the reaction temperature.

6.3.2. Ion-induced Emission from CdS Fine Particles

The author calculated the LET value at 23.2 eV/nm with the TRIM-89 code. Based on this LET value and the total film thickness ($\approx$ 420 nm), the deposited energy penetrating the film was roughly estimated to be 9700 eV which is less than 1% of the original beam energy. Therefore, the depth distribution of LET in the film could be ignored; the ion-induced phenomena were spatially homogeneous in depth in the present case.

The ion-induced emission spectra of the CdS particles prepared at (a) room temperature and (b) 80 °C, measured immediately after preparation, are shown in Figure 6.2. The top spectra were obtained at the initial irradiation stage and the bottom were at the stage of prolonged high-dose irradiation. Samples (a) and (b) were irradiated at 850-900 s ($2.7 \times 10^{14} \sim 2.9 \times 10^{14}$ ions cm^{-2}) and 1950-2000 s ($6.2 \times 10^{14} \sim 6.4 \times 10^{14}$ ions cm^{-2}), respectively, as counted from the start of the irradiation.

At the initial irradiation stage, the emission bands were observed at 440, 510, and 560-610 nm, as shown at the top. The 560-610-nm emission band (Q) is probably attributed to Cd atoms (Cd^0). This correlation is suggested by the following experimental results. It was reported that similar bands at 565 or 581 nm, depending on the sample, were generated from CdS particles by heating in air [18]. This band is probably due to Cd^0 because it is known that the heating
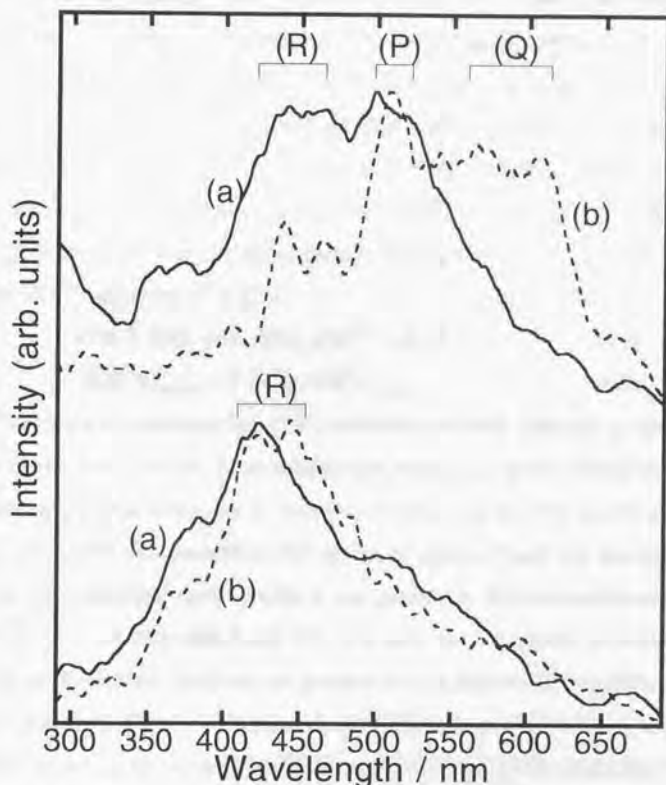
Figure 6.2. Emission spectra of CdS fine particles which were prepared at (a) room temperature and (b) 80 °C, induced by bombardments with 1.0 MeV H^+. The beam current density was 52.0 nA cm^{-2}. The top spectra represent the cumulative counts of signals for 50 s from the start of the irradiation. The measurement of the bottom spectra was carried out in succession to the top ones during the irradiation at (a) 850-900 s ($2.7 \times 10^{14} \sim 2.9 \times 10^{14}$ ions cm^{-2}) and (b) 1950-2000 s ($6.2 \times 10^{14} \sim 6.4 \times 10^{14}$ ions cm^{-2}).

of CdS can generate Cd^0 [19]. Therefore, it is reasonable to consider that, in the present case, heating at 80 °C generated Cd^0, which led to development of the emission (Q) only for sample (b). The following reactions were proposed for Cd^0 formation from a previous photoluminescence study of the same samples [20]. First, illumination of the CdS particles in air results in photooxidation of the particles (equation 6.1) [21]. This process, which has been observed on electrodes, produces $CdSO_4$ ($Cd^{2+} + SO_4^{2-}$). Secondly, photogenerated electrons are subsequently trapped by surface Cd^{2+} ions to give surface (Cd^0) (equation 6.2) [22].

$$CdS + 2\ O_2 \rightarrow CdSO_4\ (Cd^{2+} + SO_4^{2-}) \tag{6.1}$$

$$(Cd^{2+})_{surface} + 2\ e^- \rightarrow (Cd^0)_{surface} \tag{6.2}$$
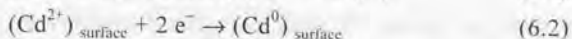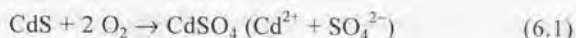
The 440-nm emission band (R) observed for both samples is assigned to sulfur-(S-)related defects. This assignment was adopted by Wang and Herron [23] because sulfur is known to fluoresce in this region [24]. As far as sample (b) is concerned, this emission (R) likely originates from the excitonic state because its wavelength corresponds to the previously determined threshold.

The 510-nm emission band (P) will now be discussed. Irradiating CdS crystals with neutron, electron, or gamma rays is known to generate emission in this region [25,26]. Galushka et al. [25] reported that the gamma ray irradiation caused an increase in the intensity of the 514-nm emission. Gamma ray irradiation generates acceptor species such as sulfur atom interstitials. Quite recently, Tam et al. [26] observed the 520-nm emission from the sulfur ion which was displaced into interstitials in the electron-irradiated CdS crystals.

These previous studies demonstrated that the state responsible for the 510-nm emission is related to a defect originating from sulfur. Additionally, some experimental results showed the following properties of this band. (i) Kotov et al. [10] observed that the emission maxima of CdS particles shifted from 510

nm in chloroform solution to 455 nm in LB films. They also proposed that desolvation of the particles in LB films led to this blue shift. Their study implied the close relation in the origin between the 510-nm state and 440-nm state in the present data. (ii) Asai et al. [27] previously observed that the behavior of these two bands during irradiation was complementary; the decrease in the 510-nm emission caused the 440-nm emission to increase. There should be a strong correlation between them. Therefore, it is possible to assume here that the 510-nm emission (P) is due to S-related defects, which may be the stabilized state of the 440-nm state (R).

This assumption is also supported by the observed fact that the ratio of the emission (P) in intensity to (R) was larger for sample (b) than for (a). It is reasonable to consider here that heating at 80 °C could accelerate the stabilization process, that is, transformation of the 440-nm state (R) to the 510-nm state (P).

After the high-dose irradiation, the emission spectra were drastically changed, as shown at the bottom of Figure 6.2. Obviously, in these spectra the emission (R) due to S-related defects, very shallow trapping sites, developed while the other emissions disappeared. This suggests that the H^+ irradiation would remove almost all the trapping sites except for the sulfur-related defect site for 440-nm emission (P). Regarding sample (b), *all* the trapping sites in the band gap are thought to be eliminated by the irradiation, if this 440-nm emission (P) is excitonic.

There was the possibility that the changes in the particle sizes induced by H^+ irradiation might lead to these trap-removing effects. However, this possibility is denied by Figure 6.3 that compares the absorption spectra of sample (a) before and after the irradiation. The absorption threshold did not show any shift, indicating that CdS particles would neither decompose nor
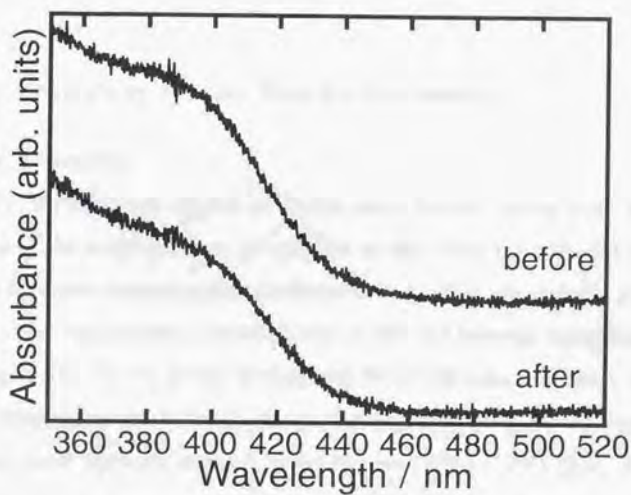
Figure 6.3. Absorption spectra of sample (a), CdS particles prepared at room temperature, obtained before and after the ion irradiation (2.9×10^{14} ions cm^{-2}). The irradiation conditions are the same as described in Figure 6.2.

aggregate during the irradiation. Thus, the trap-removing effects are probably ascribed to changes in the surface electronic states directly induced by the irradiation. Consequently, the ion irradiation was found to have an effect similar to the treatment with chemical stabilizers that modified the surface defect state.

6.3.3. Adaptability to Other Fine-Particle Systems

$Cd_{1-x}Mn_xS$ Particles

Generally, the emission spectra of DMSs show bands coming from the d or f electrons of the magnetic ions in addition to that from the intrinsic excitonic states of host non-magnetic semiconductors. In most of the systems containing Mn^{2+}, a very characteristic emission due to the d-d internal transition of Mn, involving $^4T_1(G)$-$^6A_1(S)$ levels, is observed for all Mn concentrations. At a high Mn concentration ($x \geq 0.01$), as in the present samples, a structureless emission peak appears around 590-620 nm (2.0-2.1 eV) [28]. It is now accepted that the energy of this emission does not depend on the Mn concentration, x. This is in contrast to the excitonic emission, which is significantly shifted with x. In the case of $Cd_{1-x}Mn_xS$, where the energy of the excitonic state is above this Mn^{2+} transition, the excitonic emission will be quenched, which leads to development of the Mn^{2+} luminescence over the entire concentration range of Mn [28]. This is due to effective energy transfer from the exciton to Mn^{2+}.

Figure 6.4 shows the ion-induced emission spectra of the $Cd_{0.80}Mn_{0.20}S$ particles prepared in LB films. The irradiation times counted from the beginning for each spectrum are (a) 500-1000 s, (b) 1000-2000 s, and (c) 2000-2500 s. In this figure, the emission centered at 610 nm is common in all the spectra.
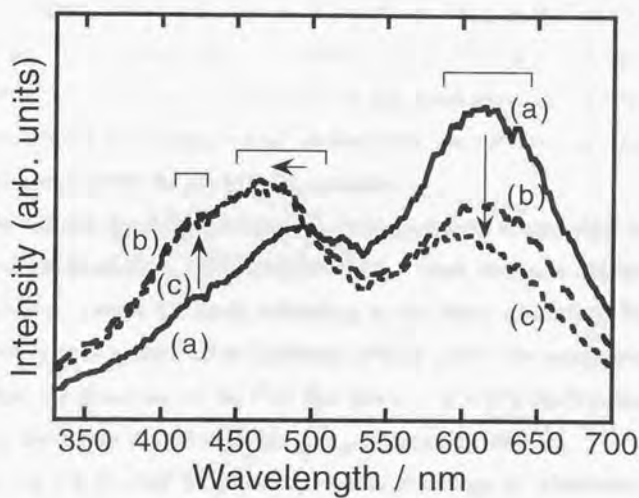
Figure 6.4. Ion-induced emission spectra of $Cd_{0.80}Mn_{0.20}S$ fine particles in LB films taken under the same conditions as stated in Figure 6.2. The measurement was carried out during the irradiation at (a) 500-1000 s, (b) 1000-2000 s, and (c) 2000-2500 s counted from the start trigger of the irradiation.

The author has considered the possibilities of Cd^0 and Mn^{2+} as the origin of this emission because both species emit in this wavelength range as already described. From the absorption spectrum of the irradiated CdS particles (Figure 6.3), it was confirmed that the ion bombardment caused little damage to the microcrystallites under this irradiation condition. Thus, if the luminescence is due to Mn^{2+} in $Cd_{0.80}Mn_{0.20}S$, its intensity is never decreased since the Mn state is intrinsic in DMSs and unchanged by ion irradiation. In contrast to the relatively small contribution of Mn^{2+} to that band, the radiative Cd^0 states might be largely responsible for the 610-nm emission.

The 490-nm band in spectrum (a) developed with a blue-shift during the course of the irradiation, and simultaneously, a weak emission appeared at the highest energy (about 420 nm). According to the above discussion, both these bands are probably ascribed to S-related defects which are complementary to each other. As observed for the CdS fine particles [20,27], the S-related defect state was reversibly shifted to higher energies during irradiation.

As a result, it could be concluded that high-energy H^+ irradiation reduces the number of deeper defect sites as determined in the CdS particles. In this case, however, only the intrinsic Mn^{2+} state is considered to be unchanged.

MnS Particles

Figure 6.5 shows the results of the irradiation of the MnS fine particles, which were obtained during the lower-dose irradiation stage (A) ((a): 200-250 s, (b): 1050-1100 s, and (c): 1750-1800 s) and at a further irradiation stage (B) in succession to (A) ((d): 1750-1800 s, (e): 2200-2250 s, and (f): 3200-3250 s). As shown in Figure 6.5 (A), the emission band centered at 450 nm was enhanced with its weak shoulder around 550-600 nm during the course of the irradiation. As for the 450-nm emission due to S-related defects, its apparent
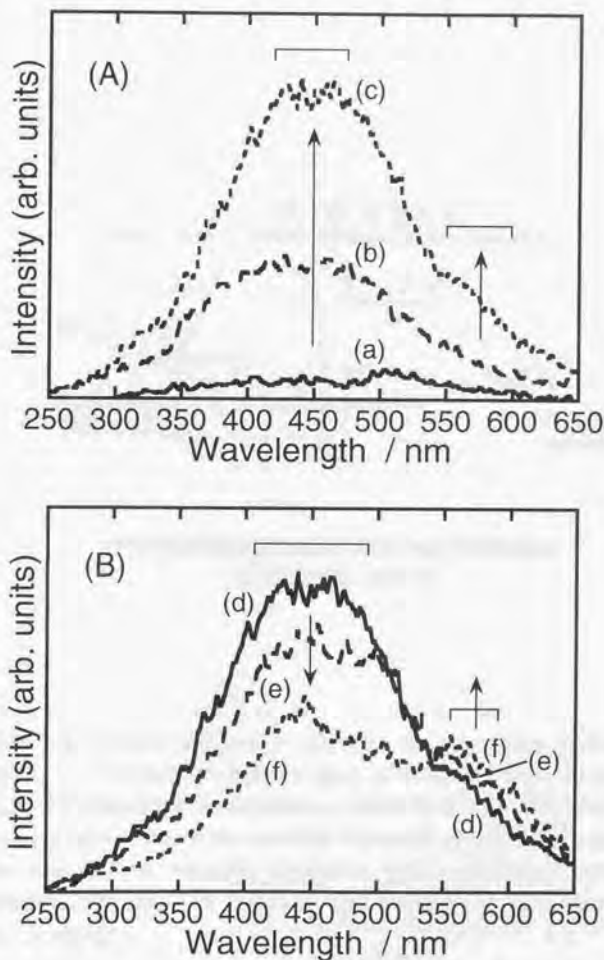
Figure 6.5. Ion-induced emission spectra of MnS fine particles incorporated into LB films under the same conditions as stated in Figure 6.2. These spectra were obtained during the lower-dose irradiation stage (A) ((a): 200-250 s, (b): 1050-1100 s, and (c): 1750-1800 s) and at the next irradiation stage (B) ((d): 1750-1800 s, (e): 2200-2250 s, and (f): 3200-3250 s).
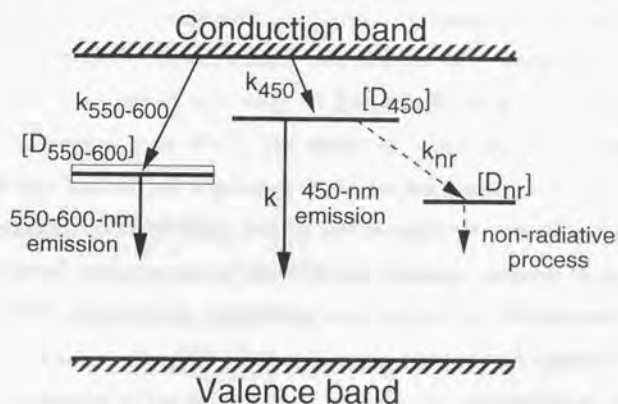
Figure 6.6. Schematic diagram to illustrate the energetics of the radiative defect states, 450-nm and 550-600-nm sites, of MnS fine particles in LB films. Considering this simplified model system, which consists of five levels, leads to a reasonable explanation of the spectral behavior of Figure 6.5. It should be noted that the 450-nm emission competes with a different non-radiative recombination process. The width of the rectangular box represents the dispersion in energy.

broad feature is possibly caused by the overlap of many intermediate bands, which occurred during the stabilization process, in line with the above assumption; the transformation from the 440-nm state (R) to the 510-nm state (P). From Figure 6.5 (B) it is recognized that further irradiation resulted in a decrease in the 450-nm emission intensity, in contrast to successive development in the 550-600 nm range. The 550-600-nm emission, which is relatively sharp as observed in a study of $Zn_{1-x}Mn_xS$ clusters inside a glass matrix [29], originates from Mn^{2+}. The observation that the Mn^{2+} band kept growing indicates that the ion irradiation decreases the density of trapping sites interfering with that band, probably leading to non-radiative recombination.

The temporal enhancement of the 450-nm emission intensity (Figure 6.5 (A)) is reasonably explained by considering a similar process. Further irradiation led to the decrease in the 450-nm emission as shown in Figure 6.5 (B). Therefore, the irradiation has the effect of reducing the concentrations of both defect states responsible for the 450-nm emission and the trapping site hindering that emission. It is possible that the reduction of the non-radiative trapping site is faster than that of the radiative 450-nm state.

In addition to the above explanation, if it is assumed that the kinetics of the two emitting states, the 450-nm and 550-600-nm sites, is determined by the energetics as illustrated in Figure 6.6, the spectral behavior of Figures 6.5 (A) and (B) can be more clearly rationalized. The author considered a simple five-level system consisting of the conduction band, valence band, and three midgap states (two radiative states emitting at 450 nm and 550-600 nm and a non-radiative state hindering the 450-nm emission). For this model system, the probability that the excited state will lead to radiation of the 450-nm luminescence, Φ_{450}, (referred to as "the quantum yield for the emission") is obtained by considering two distinct steps of competing processes as

$$\Phi_{450} = \frac{k_{450}[D_{450}]}{k_{450}[D_{450}] + k_{550-600}[D_{550-600}]} \cdot \frac{k}{k + k_{nr}[D_{nr}]} \qquad (6.3)$$

where $[D_{450}]$, $[D_{550-600}]$, and $[D_{nr}]$ are the concentrations of the corresponding mid-gap states, k_{450}, k_{550}, and k_{nr} are the rate constants for the state-state transitions as shown in Figure 6.6, and k represents the decay rate of the 450-nm emission. Analogously, the author obtained the equation for the probability, $\Phi_{550-600}$, that the excited carriers (i.e., electrons in the conduction band) will be trapped in the radiative 550-600-nm state.

$$\Phi_{550-600} = \frac{k_{550-600}[D_{550-600}]}{k_{450}[D_{450}] + k_{550-600}[D_{550-600}]} \qquad (6.4)$$

In the above discussion, it is considered that both $[D_{450}]$ and $[D_{nr}]$ are reduced by the irradiation. The author has now made the additional assumptions that, (i) $k_{550-600}[D_{550-600}]$, which represents the transition rate to the 550-600-nm site (i.e. Mn^{2+} state), is constant and (ii) both $[D_{450}]$ and $[D_{nr}]$ exponentially decrease with irradiation time, t, according to $[D_{450}] \propto \exp(-t/\tau_{450})$, $[D_{nr}] \propto \exp(-t/\tau_{nr})$, where each time constant satisfies the relation $\tau_{450} > \tau_{nr}$. Based on these assumptions, changes in the intensity of the 450-nm and the 550-600-nm emissions can be fully explained as follows. Equation 6.4 predicts that irradiation leads to the increase in $\Phi_{550-600}$, implying the successive enhancement of the 550-600-nm emission observed in Figures 6.5 (A) and (B). As for the 450-nm emission, the reduction of $[D_{nr}]$ is dominant in equation 6.4 during the early stage, leading to the increase in Φ_{450}. During a long irradiation period, $[D_{nr}]$ reaches a value which is so small that the reduction of $[D_{450}]$ is dominant over that of $[D_{nr}]$. At this time, Φ_{450} starts to decrease as predicted by equation 6.3. This resulted in the intensity of the 450-nm emission temporally increasing to a certain degree of the accumulated dose and then

decreasing. Consequently, the ion irradiation will also provide good surface passivation to the MnS microcrystallites. It should be noted that, as in the above case of the $Cd_{1-x}Mn_xS$ particles, the concentrations of the *deeper* trapping sites are reduced under the condition that the intrinsic Mn^{2+} state is unchanged.

6.3.4. Comparison with Bulk Crystals

An inevitable question then comes to mind: what effects does ion irradiation have on semiconductor bulk crystals? The ion-induced emission spectra of CdS (A) and MnS (B) bulk crystals are displayed in Figure 6.7. Obviously, in Figure 6.7 (A), the bulk CdS shows a broad band centered at 640 nm, which has been ascribed to the sulfur vacancies based on previous studies [24,27]. Strikingly, no change in the spectral features, i.e., the energy or the shape of the emission bands, was observed up to 2250 s of irradiation time. A similar result can be derived from Figure 6.7 (B). From these results, the author has concluded that the ion irradiation has a significant effect only on the Q-sized particles. It is reasonable that this difference between the bulk semiconductors and their microcrystallites is related to the surface-to-volume ratio of the number of atoms. For example, in the 3.0-nm diameter CdS particles, at least 15% of the total atoms are on the surface [30]. Therefore, as mentioned in the introduction, the luminescence from the nanoparticles strongly reflects these surface irregularities in comparison to the bulk. It follows that the surface-treatment effect can be more pronounced in the nanoparticle system.
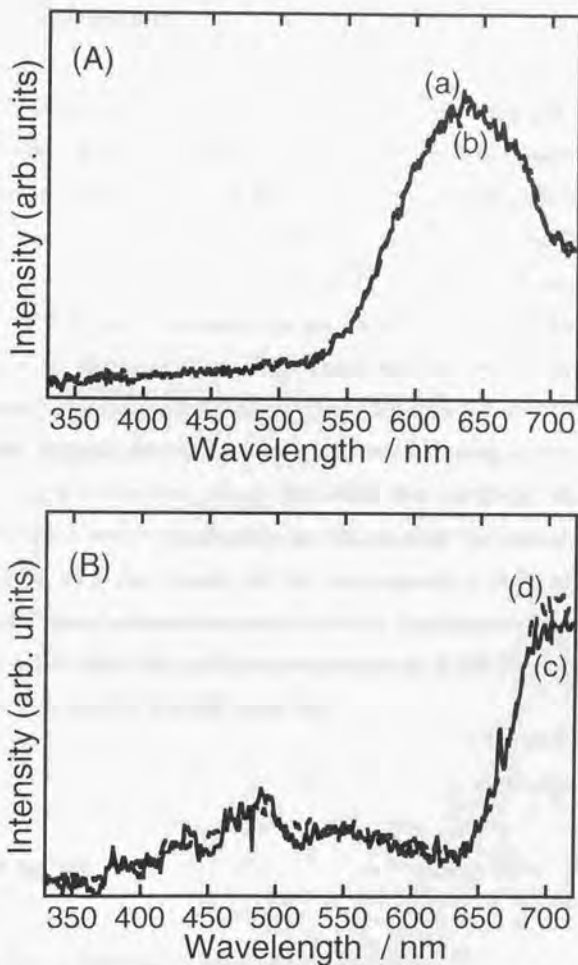
Figure 6.7. Ion-induced emission spectra of CdS (A) and MnS (B) bulk crystals on Si under the same conditions as stated in Figure 6.2. The irradiation times counted from the beginning for each spectrum are (a): 0-500 s, (b): 1750-2250 s (A), (c): 250-500 s, and (d): 2000-3000 s (B).

6.4.   Conclusions

Q-sized CdS particles with different sizes were incorporated into LB films by controlling the temperature of the H_2S treatment. In-situ observation of the high-energy-ion-induced emission provided the author with information about the effect of the ion bombardment on the electronic states of the fine particles. Several emission bands, all attributed to different localized states (defects), were observed at the initial irradiation stage, while after the high-dose irradiation with 1.0 MeV H^+, these emissions disappeared with the appearance of the band-edge emission. This suggests that high-energy ion irradiation would eliminate almost all the trapping sites in the band gap instead of using chemical methods. Also, in the case of the $Cd_{1-x}Mn_xS$ and MnS fine particles, the irradiation established a good surface passivation but did not alter the intrinsic Mn^{2+} state. In conjunction with the results of the corresponding bulk crystals, it is concluded that these surface-treatment effects by irradiation appear only in the fine particles, for which the surface-to-volume ratio of the number of atoms is much larger than that for the bulk materials.

REFERENCES

[1]   A. Henglein, *Top. Curr. Chem.* **1988**, *143*, 113.

[2]   L.E. Brus, *J. Phys. Chem.* **1986**, *90*, 2555.

[3]   L.E. Brus, *J. Chem. Phys.* **1984**, *80*, 4403.

[4]   J.H. Fendler, *Chem. Rev.* **1987**, *87*, 877.

[5] Y. Wang and N. Herron, *J. Phys. Chem.* **1991**, *95*, 525.

[6] A. Nakamura and T. Tokizaki, *Nonlinear Optics – Fundamentals, Materials, and Devices*; Elsevier Science Publishers: Amsterdam, 1992.

[7] E.S. Smotkin, C. Lee, A.J. Bard, A. Campion, M.A. Fox, T.E. Mallouk, S.E. Webber, and J.M. White, *Chem. Phys. Lett.* **1988**, *152*, 265.

[8] R. Zhu, Y. Wei, C. Yuan, S. Xiao, Z. Lu, and H.J. Schmitt, *Solid State Commun.* **1992**, *84*, 449.

[9] D.N. Furlong, R.S. Urquhart, F. Grieser, K. Tanaka, and Y. Okahata, *J. Chem. Soc. Faraday Trans.* **1993**, *89*, 2031.

[10] N.A. Kotov, F.C. Meldrum, C. Wu, and J.H. Fendler, *J. Phys. Chem.* **1994**, *98*, 2735.

[11] T. Dannhauser, M. O'Neil, K. Johansson, and G. Mclendon, *J. Phys. Chem.* **1986**, *90*, 6074.

[12] A. Eychmüller, A. Hässelbarth, L. Katsikas, and H. Weller, *J. Lumin.* **1991**, *48&49*, 745.

[13] A. Eychmüller, A. Hässelbarth, L. Katsikas, and H. Weller, *Ber. Bunsenges. Phys. Chem.* **1991**, *95*, 79.

[14] L.E. Rehn, *Environmental Degradation of Ion and Laser Beam Treated Surfaces*; The Minerals, Metals and Materials Society: Warrendale, 1989.

[15] R. Sizmann, *J. Nucl. Mater.* **1968**, *69&70*, 386.

[16] N. Kouchi, S. Tagawa, H. Kobayashi, and Y. Tabata, *Radiat. Phys. Chem.* **1989**, *34*, 453.

[17] L. Spanhel, M. Haase, H. Weller, and A. Henglein, *J. Am. Chem. Soc.* **1987**, *109*, 5649.

[18] G.D. Papavassiliou, *J. Solid State Chem.* **1981**, *40*, 330.

[19] T.Y. Soera and V.V. Serdyuk, *Opt. Spectrosc.* **1960**, *9*, 210.

[20] K. Asai, T. Yamaki, K. Ishigure, and H. Shibata, *Thin Solid Films* **1996**,

277, 169.

[21] M. Wark, G. Schultz-Ekloff, and N.I. Jaeger, *Catalysis Today* **1991**, *8*, 467.

[22] T. Rajh, O.I. Micic, D. Lawless, and N. Serpone, *J. Phys. Chem.* **1992**, *96*, 4633.

[23] Y. Wang and N. Herron, *J. Phys. Chem.* **1988**, *92*, 4988.

[24] R.A. Street, I.G. Austin, and T.M. Searle, *J. Phys. C: Solid State Phys.* **1975**, *8*, 1293.

[25] A.P. Galushka, I.B. Ermolovich, N.E. Korsunskaya, I.D. Konozenko, and M.K. Sheinkman, *Sov. Phys. Solid State* **1966**, *8*, 831.

[26] W. Tam, R. Bhave, R. Cooper, and D. Edmondson, *Radiat. Phys. Chem.* **1995**, *45*, 187.

[27] K. Asai, K. Ishigure, and H. Shibata, *J. Lumin.* **1995**, *63*, 215.

[28] M. Jain, *Diluted Magnetic Semiconductors*; World Scientific: Singapore, 1991.

[29] Y. Wang, N. Herron, K. Moller, and T. Bein, *Solid State Commun.* **1991**, *77*, 33.

[30] M. O'Neil, J. Marohn, and G. McLendon, *J. Phys. Chem.* **1990**, *94*, 4356.

CHAPTER 7

Third-Order Nonlinear Optical Properties of Surface-Modified Semiconductor Nanoparticles

ABSTRACT

The author observed the degenerate four-wave mixing (DFWM) signal from two different types of cadmium sulfide (CdS) nanoparticles to estimate their third-order optical susceptibility, $\chi^{(3)}$ ($-\omega; \omega, -\omega, \omega$). One is the CdS particle incorporated into Langmuir-Blodgett (LB) multilayers. The sample showed a $\chi^{(3)}$ value on the order of $\sim 10^{-10}$ esu under the off-resonant condition, which is comparable to that of semiconductor-doped glasses. The other is the thin-film sample containing highly surface-modified CdS nanoparticles, which exhibited a strong excitonic band in the emission spectrum. Importantly, the large $\chi^{(3)}$ reaching 10^{-7} esu should make this sample promising for resonant nonlinear optical applications at room temperature.

7.1. Introduction

With the advent of the laser, nonlinear optical phenomena have become of increasing scientific interest and of technological importance. The electric fields associated with high intensity laser beams can be so large that higher order nonlinear terms in the material polarization become significant. Thus, in addition to linear optical effects such as absorption, reflection, scattering, refraction, and dispersion, one must consider the intensity-dependent phenomena such as multiphonon absorption, harmonic generation, self-focusing, self-phase modulation, optical phase conjugation, optical bistability, and stimulated Raman and Brillouin scatterings. These phenomena associated with propagation of intense light through bulk materials have been the subject of extensive studies since the 1960s and have had significant effects on the operation of high power lasers. The past decade has witnessed increased interest in the development of new technologies.

In this context, the study of nonlinear optical materials has also evolved into a truly multidisciplinary area. Materials under investigation (except simple bulk semiconductors) are traditionally divided into three categories: organics, super-lattice structures of semiconductors, and nano-sized particles of semiconductors or metals. Each of these classes of materials has its own merits and limitations and is suited for different types of applications. As for the newest class of materials, namely, semiconductor nanoparticles which the author has focused on, since the pioneer work of Jain and Lind [1], their third-order nonlinear optical effects have been intensively studied from the standpoint of possible applications such as room temperature all-optical switching or modulation. In spite of such many studies, currently available materials do not

match device requirements and so the focus of these studies shifts to the search for nanoparticle materials possessing a larger and/or faster nonlinear response.

A number of experiments and the accompanying theory suggested that the nonlinearity (in the present case the author is interested in the third-order optical susceptibility, $\chi^{(3)}$ ($-\omega$; ω, $-\omega$, ω), for frequencies ω close to the peak of the 1s-1s transition of excitons) arises because of band filling and screening [2]. Assuming this mechanism, then when going from the bulk or weakly confined case where the oscillator strength is distributed over a broad band to the confined case where this oscillator strength is now condensed into discrete lines, one expects an enhancement in the nonlinearity. Actually, the theoretical treatments of Hanamura [3] and Takagahara [4] predicted that the confinement of excitons in cadmium sulfide (CdS) nanoparticles increases $\chi^{(3)}$ upon a decrease in the radius R and the radius dependence is approximately R^{-3}. Consequently, the promise of semiconductor nanoparticles as nonlinear optical materials is based on the fact that the properties can be tailored through size.

As mentioned throughout Chapter 6, another crucial problem regarding the application of semiconductor microcrystallites is their imperfect surfaces, which act as electron and hole traps upon optical excitation. In fact, some previous papers [5] suggested that precise control over the chemistry of the particle surface should provide an increasing potential for nonlinear optical materials. Therefore, there has been a strong motivation for the author to modify the surface state of nanoparticles in order to accomplish the above-mentioned requirements.

To this end, two types of films containing CdS nanoparticles were prepared in the present study. One is a film fabricated by the reaction of the cadmium arachidate LB multilayer with H_2S gas. The preparation and

characterization of this sample were discussed throughout several previous chapters. As mentioned in Chapter 6, the surface of the incorporated CdS nanoparticles was effectively passivated by high-energy ion irradiation. The other is a new film sample prepared by casting CdS colloidal solutions with a chemically-modified surface state. This sample exhibited a sharp excitonic emission with a high quantum yield around its absorption threshold. The author then succeeded in obtaining degenerate four-wave mixing (DFWM) signals to evaluate the third-order optical nonlinearity of both these samples. The present chapter also reports that $\chi^{(3)}$ ($-\omega$; ω, $-\omega$, ω) of the latter sample was large enough for practical applications at room temperature.

7.2. Experimental Section

Cadmium perchlorate ($Cd(ClO_4)_2$) and sodium hexametaphosphate ($(NaPO_3)_6$) were purchased from the Aldrich Chemical Co. and Wako Chemical Co., respectively, and were used as received.

The first sample, the CdS nanoparticle incorporated into an LB film, was synthesized according to the method of Smotkin et al. [6]. As already described, it involves the reaction of cadmium arachidate ($C_{19}H_{39}COO)_2Cd$, which is formed in multilayers on solid substrates, in ambient hydrogen sulfide (H_2S). For details of the preparation procedures, refer to Sections 4.2.1 and 6.2.1. Note that the H_2S treatment of the 51-layered ($C_{19}H_{39}COO)_2Cd$ film on a quartz substrate was carried out at 80 °C.

As for the second sample, fluorescing CdS colloidal solutions were prepared in two steps according to an established procedure [7,8]. (i) The

introduction of 4.0 ml of H_2S gas to a 500-ml aqueous solution containing 2.0×10^{-4} mol dm^{-3} $Cd(ClO_4)_2$ and 2.0×10^{-4} mol dm^{-3} $(NaPO_3)_6$ led to the formation of a transparent CdS colloidal solution. (ii) The solution was activated (or passivated) by first adding 1.0 mol dm^{-3} NaOH and then 1.0 mol dm^{-3} $Cd(ClO_4)_2$ to establish a pH of 10.5 and contain 10% excess Cd^{2+}. The subsequent evaporation of the solvent below 60 °C yielded redispersible CdS powders. The obtained powders readily dissolved in a very small amount of water to give a homogeneous solution. Finally, CdS particles in such a concentrated solution were cast on a quartz substrate and dried under reduced pressure.

Optical absorption of all the samples was measured with a Hitachi U-3200 UV-Vis spectrophotometer for evaluating the size of the generated particles. For the latter sample, emission spectra were obtained with a Hitachi F-3000 spectrophotometer to probe the surface state of the nanoparticles. Liquid sample was measured using a 10-mm optical path quartz cell. These measurements were made at room temperature.

The setup of the present DFWM experiment was arranged in the two-beam self-diffraction configuration [9] illustrated in Figure 7.1. The author used an optical parametric amplifier seeded by an amplified mode-locked $Ti:Al_2O_3$ laser as the light source. The pulse duration and the repetition rate were 120 fs and 100 or 200 kHz, respectively. The pulse from the pump source was divided into two beams with wave vectors k_1 and k_2, which were mutually delayed. The diffracted signal in the $k_3 = 2k_1 - k_2$ direction was simultaneously detected with a calibrated Si PIN photodiode as a function of the delay time. The sample could be held in a vacuum chamber and, if necessary, at a low temperature (8 K) to prevent illumination damage during the measurement.
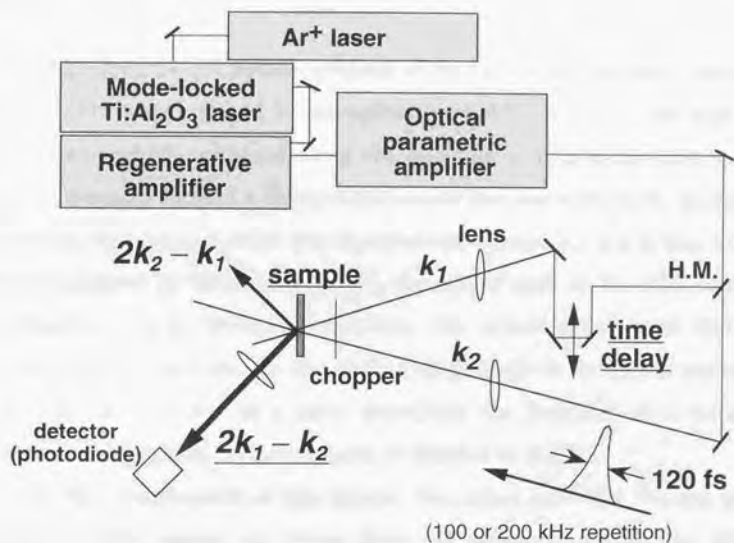
Figure 7.1. Experimental set-up of the DFWM technique using the two-incident-beam configuration.

7.3. Results and Discussion

7.3.1. Third-Order Nonlinearity of CdS Nanoparticles in LB Film Matrices

Figure 7.2 shows the absorption spectrum of the CdS nanoparticles prepared in LB films. The wavelength of an absorption threshold was blue-shifted from the bulk crystal, which is indicative of the quantum confinement effect. The sample, however, showed a gentle slope around the threshold in the spectrum, suggesting that it has a wide size distribution. Therefore, according to the method adopted by Spanhel et al. [7], the author took as the threshold the inflection point of the absorption spectrum. The inflection point was 420-440 nm. From this wavelength, the size of the CdS particles in the film is estimated to be 3.0-3.4 nm based on a curve describing the threshold as a particle-diameter resulting from previous studies of Spanhel et al. [7].

For the measurement of this sample, the author used the 542-nm pulse from the pump source. As found from the comparison with the above absorption spectrum, the wavelength of the laser was off-resonant from the any electronic transitions so that one can ignore the effects of excitons and multiple phonon absorption.

Figure 7.3 (a) shows a typical time-delay dependence of the diffracted signal intensity observed for the sample at 8 K. The signal intensity increased as the incident pump intensity was enhanced with its time evolution almost unchanged in the measured intensity range. The curve was nearly symmetric about the zero-delay line although the signal-to-noise ratio was not very good. This observation is quite natural under the off-resonant condition because the
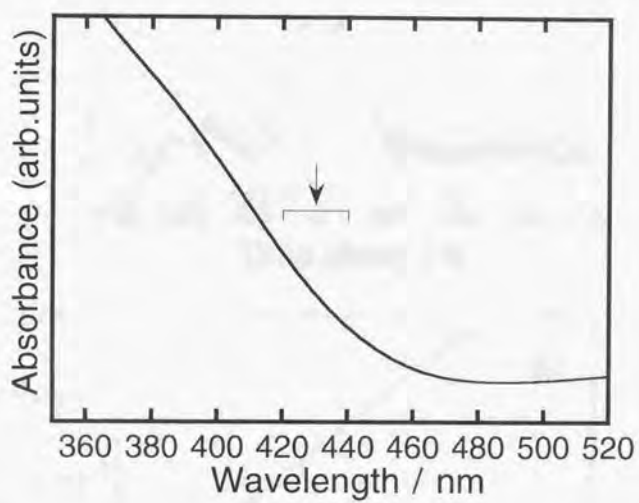
Figure 7.2. Absorption spectrum of CdS nanoparticles prepared in LB films at 80 °C. The arrow marks the threshold wavelength on the spectrum.
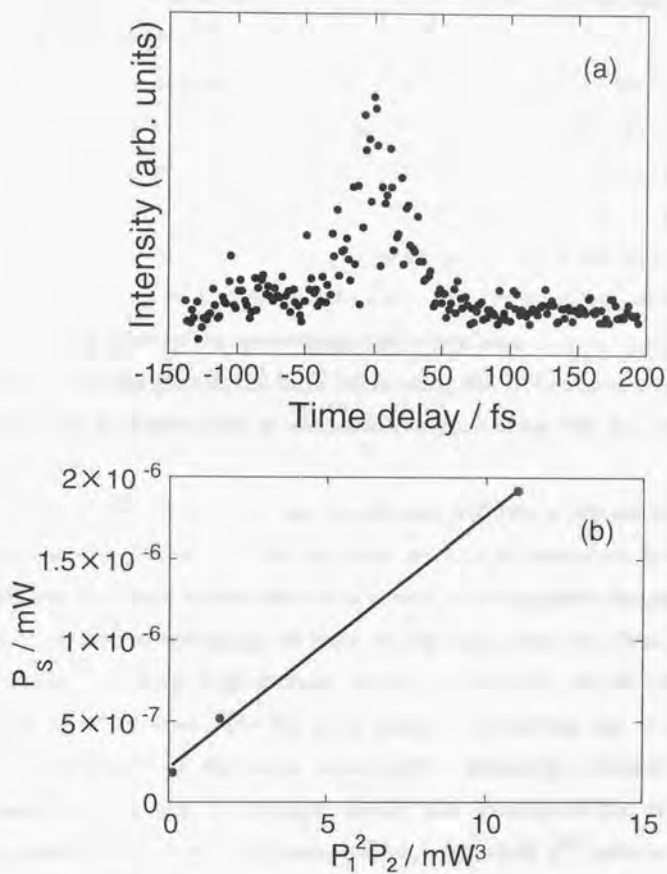
Figure 7.3. (a) Intensity of diffracted signal from CdS nanoparticles in LB films pumped at 542 nm versus time delay measured at 8 K. (b) Diffracted signal intensity versus the product of the pump beam intensities, $P_1^2P_2$, obtained under the same conditions as (a).

nonlinear optical interaction between the incident beams occurs only within the pulse duration time.

The maximum signal intensity, I_S, is known to increase in proportion to the third power of the incident pump intensity. Thus, the magnitude of $|\chi^{(3)}|$ was determined by plotting P_S versus the product of the intensities of the pump beams, $P_1^2 P_2$, as shown in Figure 7.3 (b). The absolute value of $|\chi^{(3)}|$ was of the order of 10^{-10} esu with the largest experimental error due to the bad S/N ratio. Since, to the best of the author's knowledge, no paper has been published on a DFWM study of the nonresonant optical nonlinearity in semiconductor fine particles, the comparison has been made using the THG measurement results. The $\chi^{(3)}$ value obtained here is comparable to those of the $CdS_x Se_{1-x}$ doped glass systems [10].

The measurement, however, became too difficult to provide enough data for systematic discussion. This was considered to be caused by the following problems. It is well-known that the preparation of nanoparticles using the LB technique has an advantage of their incorporation into the films in a high concentration. Such high-density doping of particles should enhance the scattering of incident light from the sample, preventing one to detect the diffracted signal on the same wavelength efficiently. Furthermore, the measurement using the present set-up was limited to the off-resonant wavelength range of the CdS nanoparticles, where their $\chi^{(3)}$ value is extremely small. This might make it more difficult to carry out the DFWM experiments on the LB-film samples.

Accordingly, the following discussion is only focused on another sample, i.e., the film cast from the surface-modified CdS colloidal solutions.

7.3.2. Stabilizing Effect for CdS Nanoparticles in the Film Cast from Colloidal Solutions

Figure 7.4 (a) shows the absorption and emission spectra of the colloidal solution. The absorption threshold blue-shifted from the bulk crystal led to the assessment of about 6 nm for the mean diameter of the CdS particles, based on the above-mentioned method. The sample exhibited a sharp emission at 495 nm due to excitons and a broad band around 670-690 nm which originates from the radiative recombination of charge carriers trapped at surface defects ascribed to sulfur vacancies. The appearance of the former band indicates the achievement of good particle-surface passivation. In general, CdS particles in solutions and in solid matrices show only a broad, low-energy emission due to the radiative recombination via trapping sites.

From the spectra of the film prepared from the solution (Figure 7.4 (b)), the position of the absorption threshold was found to be invariant between the CdS particles in the aqueous solutions and in the solid films, although baseline absorbance increased possibly due to scattering or reflection of light. This indicates that any film fabrication process did not alter the CdS crystal size or induce cluster coalescence. In contrast, the emission properties of the CdS particles were sensitive to the environment. The excitonic emission in the films was enhanced compared to that in solution. Apparently, the formation of solid films provided a sufficient microenvironmental change that increased the emission in the excitonic range at the expense of the low-energy emission. This behavior may be rationalized by assuming that the efficiency of a surface passivation is dominated by the density of activator molecules (or passivating species) surrounding the particle. The concentration of CdS colloidal suspensions in a solid form increases the efficiency of the surface passivation,
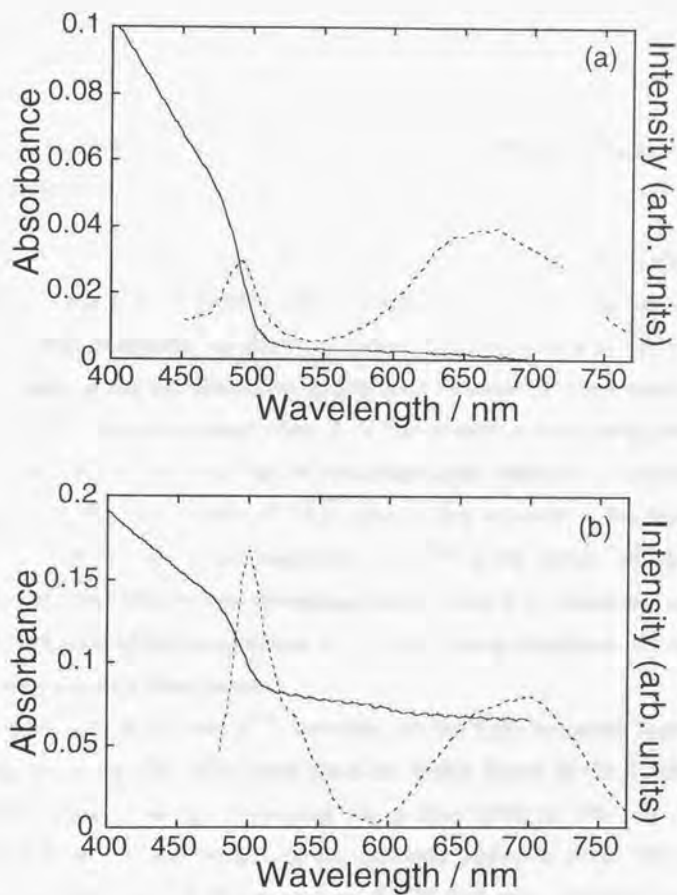
Figure 7.4. The absorption (solid line) and emission (dashed line) spectra of (a) the CdS colloidal solution and (b) the solid film prepared from it. The emission spectra were taken with sample excitation at (a) 350 and (b) 450 nm.

thereby removing a larger number of surface traps and increasing excitonic recombinations.

7.3.3. Third-Order Nonlinearity of Surface-Modified CdS Nanoparticles in the Cast Film

From a nonlinear optical experiment using the second sample, the author also obtained a time-delay dependence of the intensity of the diffracted signal with various pump intensities. As shown in Figure 7.5, the signal intensity reaches the maximum at the zero time delay and exhibits a symmetric shape about it due to a very short phase relaxation time, T_2, of the system at room temperature. It is expected for a $\chi^{(3)}$ process that the maximum signal intensity, I_S, increased in proportion to the third power of the incident pump intensity in the measured range (< 300 W/cm^2). The magnitude of $|\chi^{(3)}|$ at the pump wavelengths between 480 and 500 nm was determined from a plot of P_S versus the product of the intensities of the pump beams, $P_1^2 P_2$, after having taken into account the absorption and refraction losses.

Figure 7.6 shows the $|\chi^{(3)}|$ spectrum of the film prepared from CdS colloidal solutions. The absorption spectrum is also shown by the dashed line for comparison. The $|\chi^{(3)}|$ spectrum has a clear peak at 495 nm, which corresponds to the wavelength of the excitonic emission peak. This is in contrast to the result of Roussignol et al. [2] and many research groups showing that the absorption and $\chi^{(3)}$ bear a linear relationship to each other. As already introduced, they also proposed a simple two-level saturation model based on band filling effects for the dependence on absorption. The mechanism determining the resonant behavior, which was observed here, has not been
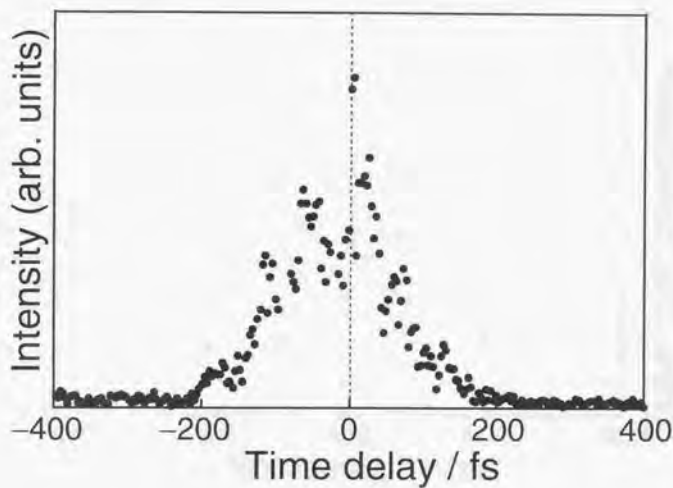
Figure 7.5. Intensity of diffracted signal from the solid film containing chemically surface-modified CdS nanoparticles, for the excitation near-resonant to the lowest exciton, versus time delay measured at room temperature.
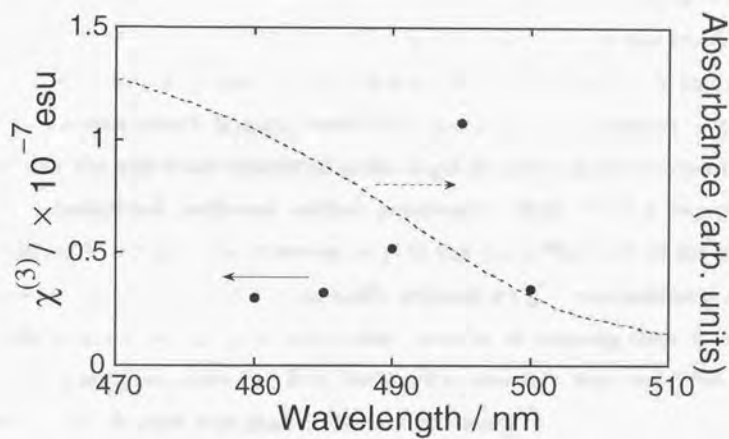
Figure 7.6. $|\chi^{(3)}|$ and absorption spectra of the CdS film prepared from the surface-modified colloidal solution.

clarified so far. The author is now trying to clarify it in connection with the good surface modification achieved in the samples.

The major point to note here is that the maximum $|\chi^{(3)}|$ value was as large as 10^{-7} esu. This value seems to be larger than those of CdS_xSe_{1-x} microcrystallites in glasses, which give rise to a value on the order of 10^{-10}-10^{-9} esu [2]. In composite materials, $\chi^{(3)}$ values are proportional to the volume fraction of the embedded colloids in the matrix. The large volume fraction for the present sample, which was estimated to be more than $0.5 \sim 1\%$ for typical semiconductor-doped glasses, would have led to the enhancement in $\chi^{(3)}$. In addition, the author has considered as the origin of such a large nonlinearity, the above-mentioned sufficient surface passivation effect. This is reasonably predicted by the previous observation [11] that the reflectivity of the optical phase conjugation, which quadratically depends on $\chi^{(3)}$, was enhanced in the highly luminescing samples with a small number of trapping sites. If so, the present paper describes the first finding that quantum dots stabilized by a surface modification procedure exhibit such a large $\chi^{(3)}$.

7.4. Conclusions

The aim of this chapter was to discuss how to improve and/or to arbitrarily control the nonlinear optical properties of semiconductor nanoparticles by modifying their surface states. Two different types of CdS nanoparticle samples were employed: (i) a particle incorporated into LB films, and (ii) a CdS-containing thin film prepared by casting the colloidal solutions. The $\chi^{(3)}$ $(-\omega; \omega, -\omega, \omega)$ value for each sample was estimated based on the DFWM technique.

For sample (i), $\chi^{(3)}$ of the order of ~ 10^{-10} esu, which is comparable to that of semiconductor-doped glasses, was obtained. However, due to an instrumental limitation and sample problem, the measurement became too difficult to provide enough data for a systematic discussion. In sample (ii), the formation of CdS films on a substrate, without any change in the particle size, enhanced the quantum yield of an excitonic band by removing a large number of surface traps. This film showed a large $\chi^{(3)}$ value near ~ 10^{-7} esu around the exciton resonance at room temperature. This was possibly brought about by an effective surface passivation as well as a high CdS microcrystallite concentration.

REFERENCES

[1] R.K. Jain and R.C. Lind, *J. Opt. Soc. Am.* **1983**, *73*, 647.

[2] P. Roussignol, D. Ricard, J. Lukasik, and C. Flytzanis, J. Opt. Soc. Am. B **1987**, *4*, 5.

[3] E. Hanamura, *Phys. Rev. B* **1988**, *37*, 1273.

[4] T. Takagahara, *Phys. Rev. B* **1989**, *39*, 10206.

[5] For review, L. Brus, *Appl. Phys. A* **1991**, *53*, 465.

[6] E.S. Smotkin, C. Lee, A.J. Bard, A. Campion, M.A. Fox, T.E. Mallouk, S.E. Webber, and J.M. White, *Chem. Phys. Lett.* **1988**, *152*, 265.

[7] L. Spanhel, M. Haase, H. Weller, and A. Henglein, *J. Am. Chem. Soc.* **1987**, *109*, 5649.

[8] Y. Tian, C. Wu, and J.H. Fendler, *J. Phys. Chem.* **1994**, *98*, 4913.

[9] P. Horan, W. Blau, H. Byrne, and P. Berglund, *Appl. Opt.* **1990**, *29* (1), 31.

[10] Y. Wang and N. Herron, *Inter. J. Nonlinear Opt. Phys.* **1992**, *1*, 683.

[11] P. Roussignol, D. Ricard, K.C. Rustagi, and C. Flytzanis, *Opt. Commun.* **1985**, *55*, 143.

CHAPTER 8

Concluding Remarks

In the present work the author reported the preparation of two different low-dimensional semiconductor systems, polysilanes and semiconductor nanoparticles, and then the possibility of systematically controlling the characteristic properties based on their intrinsic electronic structure. To organize the low-dimensional elements for device applications, the methods of interface chemistry such as the LB molecular handling technique were employed.

The first system was a polysilane polymer regarded as a one-dimensional material based on the σ-conjugation in the Si-Si skeletons. The author expected that the molecular interaction would become one of the controllable factors in such a system.

Chapter 2 demonstrated that it was possible to introduce ammonium moieties into the side chains of the polysilanes as hydrophilic groups. Application of the LB technique for these polysilanes was able to modulate the molecular arrangement which cannot be attained using a simple casting method. These materials might be of interest in the fields of microelectronics and microoptics.

In Chapter 3, as a first step for such applications, the author examined the

molecular interaction in the polysilanes. Based on detailed spectroscopic measurements of the samples, it was found that the molecular interactions could be controlled both intra- and intermolecularly. Interestingly, the present study observed, for the first time, the emission from the excited complexes formed in the polysilanes.

The second system was a Q-sized semiconductor particle to further decrease the dimensions to zero-dimensional structures. In this system, the size and shape of the microcrystallites are important factors related to their electronic properties, which are also related to the physics of *quantum size effects*. It should be emphasized that the author considered here, as another factor, the equally important surface effects, which have been neglected in most previous studies on nanoparticles.

Chapter 4 described the investigation of the growth of CdS microcrystallites in the LB films. RBS measurements indicated that the Q-sized CdS produced in the assemblies was not two-dimensional (disk-shaped) but spherical, as described in previous reports. The example presented here demonstrated that RBS was useful for an analysis of the structural changes in LB films accompanied by the formation of Q-sized particles.

Chapter 5 provided the first example of DMS fine particles incorporated into the LB films. It was shown that $Cd_{1-x}Mn_xS$ (x = 0.45, 0.27, and 0.20) fine particles with about a 3-nm diameter could be prepared in a manner modified from that used for preparing binary CdS particles.

As shown in Chapter 6, the high-energy-ion irradiation would remove almost all the mid-gap traps existing on the surface of the CdS particles. Anyway, the technique presented here established a good surface passivation instead of using conventional chemical methods although the determining mechanism is still unclear at the present.

Chapter 7 was concerned with the nanoparticle applications for possible electronic devices when its surface states were modified. A very effective surface passivation was achieved by preparing the cast films from CdS colloidal solutions. This film showed a large $\chi^{(3)}$ value near $\sim 10^{-7}$ esu around the exciton resonance at room temperature.

Consequently, from the overall descriptions, it was found that the methodologies employed in this study are useful to synthesize the novel artificial materials and to appropriately design the desired properties.

In spite of the extremely fast-paced progress in the research of low-dimensional semiconductors, exploitation of the results to practical functioning economic devices has been disappointingly slow. The author is confident that he shall witness a rapid progress in this direction in the very near future. The key lies, the author believes, in using the low-dimensional materials as molecular elements and constructing, or preferentially self-assembling, functional networks with the desired composition and topology. In this context, it is expected that the present work will contribute to the development of the methods for producing these materials and to the success secured by the future entry of nanostructured devices into industry.

List of Publications

1. Scientific Papers

[1] S. Seki, M. Ando, T. Yamaki, Y. Nakashiba, K. Asai, K. Ishigure, and S. Tagawa
"Molecular Interaction in Langmuir-Blodgett Films of Amphiphilic Polysilanes"
J. Photopolym. Sci. Technol. **1995**, *5*, 89-100.

[2] K. Asai, T. Yamaki, S. Seki, K. Ishigure, and H. Shibata
"Ion Bombardment Effect on Electronic States in CdS Fine Particles"
Thin Solid Films **1996**, *277*, 169-174.

[3] K. Asai, T. Yamaki, S. Seki, K. Ishigure, and H. Shibata
"Surface Treatment Effect of Ion-irradiation on Size-Quantized Semiconductor Particles Incorporated into L.B. Films"
Thin Solid Films **1996**, *284-285*, 541-544.

[4] 八巻 徹也、浅井 圭介、石樽 顕吉
「高エネルギーイオンビーム照射による半導体超微粒子の表面処理効果」
東京大学工学部・工学系研究科紀要(A)研究報告、**1996**, *34*, 68-69.

[5] T. Yamaki, K. Asai, K. Ishigure, and H. Shibata
"Changes in the Surface Electronic States of Semiconductor Fine Particles Induced by High Energy Proton Irradiation"
Radiat. Phys. Chem. **1997**, *50*, 199-205.

[6] T. Yamaki, K. Asai, and K. Ishigure
  "RBS Analysis of Langmuir-Blodgett Films Bearing Q-Sized CdS Particles"
  Chem. Phys. Lett. **1997**, *273*, 376-380.

[7] T. Yamaki, Y. Nakashiba, K. Asai, K. Ishigure, S. Seki, S. Tagawa, and H. Shibata
  "Exciplex Emission from Amphiphilic Polysilanes Bearing Ammonium Moieties"
  J. Nucl. Mater. **1997**, *248*, 369-373.

[8] T. Yamaki, T. Yamada, K. Asai, K. Ishigure, and H. Shibata
  "Ion Irradiation Effect on Diluted Magnetic Semiconductor Fine Particles Incorporated into L.B. Films"
  Thin Solid Films **1998**, *327-329*, 581-585.

[9] T. Yamaki, T. Yamada, K. Asai, and K. Ishigure
  "Diluted Magnetic Semiconductor Nanoparticles Fabricated by L.B. Technique"
  Thin Solid Films **1998**, *327-329*, 586-590.

[10] T. Yamaki, Y. Nakashiba, K. Asai, K. Ishigure, S. Seki, S. Tagawa, and H. Shibata
  "Intramolecular Exciplex Formation in Ammonium-Type Amphiphilic Polysilanes"
  Polym. Prepr. (Am. Chem. Soc., Div. Polym. Chem.) **1998**, *39*, 767.

[11] T. Yamaki, K. Asai, K. Ishigure, K. Sano, and K. Ema
  "DFWM Study of Thin Films Containing Surface-Modified CdS Nanoparticles"
  Synth. Met. in press.

[12] T. Yamaki, K. Asai, K. Ishigure, K. Ema, and H. Yaguchi
   "Quantum Size Effect of Lead Iodide Nanoparticles Formed by a Langmuir-Blodgett Technique"
   Mol. Cryst. Liq. Cryst., in press.

2. Conference Proceedings and Abstracts

[1] 八巻 徹也、高橋 克、小川 誠、菅原 義之、黒田 一幸
   「層状ジケイ酸塩から誘導されたメソポーラスシリカ多孔体中でのCdS微粒子の合成」
   日本化学会第67春季年会、東京、1994年3月29日-4月1日
   講演要旨集: p. 254

[2] 八巻 徹也、浅井 圭介、関 修平、石榑 顕吉、柴田 裕実
   「高エネルギーイオン照射によるサイズ量子化された半導体超微粒子の表面電子状態変化」
   第3回東京大学原子力研究総合センターシンポジウム、東京、1994年12月5-6日
   UTNST-SMP-3: p. 184-189

[3] 八巻 徹也、浅井 圭介、石榑 顕吉、柴田 裕実
   「高エネルギーイオン照射によるサイズ量子化された半導体超微粒子の電子状態変化」
   日本化学会第69春季年会、京都市 (京都)、1995年3月27-30日
   講演要旨集: p. 245

[4] 八巻 徹也、浅井 圭介、関 修平、石榑 顕吉、柴田 裕実
「半導体及び高分子材料の電子物性に対するイオン照射効果」
「MeVイオンビームによる材料照射効果研究の現状と将来」研究会、
東海村 (茨城)、1995年8月25日

[5] K. Asai, T. Yamaki, S. Seki, K. Ishigure and H. Shibata
"Surface Treatment Effect of Ion-irradiation on Size-Quantized Semiconductor Particles Incorporated into L.B. Films"
The 7th International Conference on Organized Molecular Films, Numana (Ancona, Italy), September 10-15, 1995
Abstracts: p. 85

[6] 八巻 徹也、浅井 圭介、石榑 顕吉、柴田 裕実
「高エネルギーイオン照射による半導体超微粒子表面の電子状態変化」
第48回コロイドおよび界面化学討論会、札幌市 (北海道)、1995年10月
12-14日
講演要旨集: p. 238-239

[7] 中柴 行雄、八巻 徹也、安藤 将人、関 修平、浅井 圭介、石榑 顕
吉、柴田 裕実、田川 精一
「ポリシランLB膜へのイオンビーム照射による電子構造評価」
第48回コロイドおよび界面化学討論会、札幌 (北海道)、1995年10月
12-14日
講演要旨集: p. 240-241

[8] 八巻 徹也、中柴 行雄、安藤 将人、関 修平、浅井 圭介、石榑 顕
吉、柴田 裕実、田川 精一
「ポリシランLB膜中における分子間相互作用」
第14回固体・表面光化学討論会、東京、1995年11月28-29日
講演要旨集: p. 248-249

[9] 渡邊 崇、八巻 徹也、山田 健郎、中柴 行雄、浅井 圭介、石榑 顕吉
「RAPIDを用いた Langmuir-Blodgett 膜のキャラクタリゼーション」
第4回東京大学原子力研究総合センターシンポジウム、東京、1995年12月4-5日
UTNST-SMP-4: p. 151-156

[10] 八巻 徹也、中柴 行雄、安藤 将人、関 修平、浅井 圭介、石榑 顕吉、柴田 裕実、田川 精一
「ポリシランＬＢ膜中における分子相互作用」
第4回東京大学原子力研究総合センターシンポジウム、東京、1995年12月4-5日
UTNST-SMP-4: p. 226-228

[11] T. Yamaki, K. Asai, K. Ishigure and H. Shibata
"Changes in the Surface Electronic States of Semiconductor Fine Particles Induced by High Energy Ion Irradiation"
The 7th International Symposium on Advanced Nuclear Energy Research, Recent Progress in Accelerator Beam Application, Takasaki (Gunma, Japan), March 18-20, 1996
Abstracts: p. 76
Proceedings: JAERI-Conf 97-003, p.331-336

[12] T. Yamaki, Y. Nakashiba, K. Asai, K. Ishigure, S. Seki, S. Tagawa and H. Shibata
"Exciplex Emission from Amphiphilic Polysilanes Bearing Ammonium Moieties"
International Workshop on Interfacial Effects in Quantum Engineering Systems (IEQES-96), Mito (Ibaraki, Japan), August 21-23, 1996
Abstracts: p. 97

[13] T. Yamaki, K. Asai, K. Ishigure and H. Shibata
"Changes in the Surface Electronic States of Semiconductor Fine Particles Induced by High Energy Ion Irradiation"
International Workshop on Interfacial Effects in Quantum Engineering Systems (IEQES-96), Mito (Ibaraki, Japan), August 21-23, 1996
Abstract Book: p. 98

[14] 中柴 行雄、八巻 徹也、浅井 圭介、石榑 顕吉、関 修平、田川 精一
「アンモニウム側鎖基を有する両親媒性ポリシランの可視発光特性」
日本化学会第71秋季年会、福岡市 (福岡)、1996年10月6-9日
講演要旨集: p. 30

[15] 八巻 徹也、浅井 圭介、石榑 顕吉
「RBSを用いた半導体超微粒子-LB膜コンポジットの構造評価」
日本化学会第71秋季年会、福岡市 (福岡)、1996年10月6-9日
講演要旨集: p. 39

[16] 江馬 一弘、川原 秀之、上野 佳宏、阿部 奈苗、岸野 志保、陸川 政弘、田渕 裕子、緒方 直哉、八巻 徹也、山田 健郎、浅井 圭介
「構造制御された導電性高分子における3次の非線形光学効果」
文部省科学研究費・重点領域研究「有機非線形光学材料による光波マニピュレーション」平成8年度第2回研究会 (担当B班：位相・振幅のマニピュレーション)、浜松市 (静岡)、1996年11月13-14日
講演論文集: p. 71-74

[17] 八巻 徹也、浅井 圭介、石榑 顕吉、柴田 裕実
「高エネルギーイオン照射による半導体超微粒子の電子構造制御」
第5回東京大学原子力研究総合センターシンポジウム、東京、1996年12月2日

UTNST-SMP-5: p. 65-69

[18] 江馬 一弘、川原 秀之、上野 佳宏、阿部 奈苗、岸野 志保、浅井 圭介、八巻 徹也、山田 健郎、中田 弘太郎、陸川 政弘、田渕 裕子、緒方 直哉、近藤 高志、早瀬 茂規、岩本 敏、伊藤 良一
「有機薄膜中の過渡回折格子を利用した超高速波形マニピュレーション」
平成9年度文部省科学研究費重点領域研究「有機非線形光学材料による光波マニピュレーション」第4回全体会議研究発表会、和光市 (埼玉)、1997年1月21-22日
講演予稿集: p. 70-71

[19] 江馬 一弘、上野 佳宏、岸野 志保、陸川 政弘、田渕 裕子、緒方 直哉、浅井 圭介、八巻 徹也、近藤 高志、伊藤 良一
「有機薄膜中の過渡回折格子を利用した超高速波形マニピュレーション」
文部省科学研究費・重点領域研究「有機非線形光学材料による光波マニピュレーション」平成9年度第1回研究会全体会議、仙台市 (宮城)、1997年6月11-12日
研究会講演資料: Vol. 3 (No. 1) p. 61-62

[20] T. Yamaki, T. Yamada, K. Asai, K. Ishigure and H. Shibata
"Ion Irradiation Effect on Diluted Magnetic Semiconductor Fine Particles Incorporated into L.B. Films"
The 8th International Conference on Organized Molecular Films, Asilomar (California, U.S.A.), August 24-29, 1997
Abstracts: 7-P-33

[21] T. Yamaki, T. Yamada, K. Asai and K. Ishigure
"Diluted Magnetic Semiconductor Nanoparticles Fabricated by L.B. Technique"
The 8th International Conference on Organized Molecular Films, Asilomar

(California, U.S.A.), August 24-29, 1997
　Abstracts: 7-P-34

[22] 山崎 和彦、八巻 徹也、浅井 圭介、石樽 顕吉、柴田 裕実
「高エネルギーイオンビームによる CdS 超微粒子の形成」
日本化学会第73秋季年会、盛岡市 (岩手)、1997年9月26-29日
講演要旨集: p. 200

[23] 堀内 祥平、藤井 宏行、八巻 徹也、山田 健郎、浅井 圭介、石樽 顕吉
「LB法を用いた希薄磁性半導体超微粒子の作製とその磁気特性評価」
　第50回コロイドお　よび界面化学討論会、佐賀市 (佐賀)、1997年10月8-10日
講演要旨集: p. 74

[24] 八巻 徹也、浅井 圭介、石樽 顕吉
「半導体超微粒子を担持したLB膜のラザフォード後方散乱分析」
　第50回コロイドおよび界面化学討論会、佐賀市 (佐賀)、1997年10月8-10日
講演要旨集: p. 75

[25] 中柴 行雄、八巻 徹也、浅井 圭介、石樽 顕吉、柴田 裕実、関 修平、田川 精一
「アンモニウム側鎖型の両親媒性ポリシランにおける分子内相互作用」
　第50回コロイドおよび界面化学討論会、佐賀市 (佐賀)、1997年10月8-10日
講演要旨集: p. 219

[26] 山崎 和彦、八巻 徹也、浅井 圭介、石樽 顕吉、柴田 裕実
「チオールへの放射線照射効果を用いた CdS 超微粒子の新規作製法」

第50回コロイドおよび界面化学討論会、佐賀市 (佐賀)、1997年10月
8-10日
講演要旨集: p. 252

[27] 中柴 行雄、八巻 徹也、浅井 圭介、石榑 顕吉、柴田 裕実、関 修
平、田川 精一
「イオンビーム照射によるポリシラン励起状態の緩和過程の研究」
日本原子力学会1997年秋の大会、宜野湾市 (沖縄)、1997年10月14-17日
予稿集: 第I分冊, p. 253

[28] 山崎 和彦、八巻 徹也、浅井 圭介、石榑 顕吉、柴田 裕実
「チオールへの放射線照射による CdS 超微粒子の作製」
日本原子力学会1997年秋の大会、宜野湾市 (沖縄)、1997年10月14-17日
予稿集: 第I分冊, p. 253

[29] 八巻 徹也、浅井 圭介、石榑 顕吉
「半導体超微粒子を担持した有機超薄膜の構造解析におけるラザフォー
ド後方散乱の適用」
日本原子力学会1997年秋の大会、宜野湾市 (沖縄)、1997年10月14-17日
予稿集: 第I分冊, p. 254

[30] T. Yamaki, Y. Nakashiba, K. Asai, K. Ishigure, S. Seki, S. Tagawa and H.
Shibata
"Exciplex Emission from Ammonium-type Amphiphilic Polysilanes"
5th Pacific Polymer Conference, Kyongju (Korea), October 26-30, 1997
Preprints: p. 240

[31] 中柴 行雄、八巻 徹也、浅井 圭介、石榑 顕吉、柴田 裕実、関 修
平、田川 精一
「アンモニウム側鎖型両親媒性ポリシランにおけるエキサイプレックス

発光」
第2回ケイ素化学協会シンポジウム、守山市 (滋賀)、1997年11月20-21
日
UTNST-SMP-6: p. 246-249

[32] 堀内 祥平、八巻 徹也、浅井 圭介、石榑 顕吉、柴田 裕実
「LB 法により作製した希薄磁性半導体超微粒子へのイオン照射効果」
第6回東京大学原子力研究総合センターシンポジウム、東京、1997年12
月3日
UTNST-SMP-6: p. 246-249

[33] 堀内 祥平、八巻 徹也、浅井 圭介、石榑 顕吉、柴田 裕実
「LB 法により作製した希薄磁性半導体超微粒子へのイオン照射効果」
日本化学会第74春季年会、京田辺市 (京都)、1998年3月27-30日
講演予稿集: p. 285

[34] T. Yamaki, K. Asai, K. Ishigure, K. Sano and K. Ema
"DFWM Study of Thin Films Containing Surface-modified CdS
Nanoparticles"
International Conference on Science and Technology of Synthetic Metals
(ICSM '98), Montpellier (France), July 12-18, 1998
Book of Abstracts: p. 73

[35] T. Yamaki, Y. Nakashiba, K. Asai, K. Ishigure, S. Seki, S. Tagawa and H.
Shibata
"Intramolecular Exciplex Formation in Ammonium-type Amphiphilic
Polysilanes"
216th ACS (American Chemical Society) National Meeting, Boston
(Massachusetts, U.S.A.), August 23-27, 1998
Book of Abstracts: Part 3, Paper No. 376

[36] T. Yamaki, K. Asai, K. Ishigure, K. Ema, and H. Yaguchi
"Quantum Size Effect of Lead Iodide Nanoparticles Formed by a Langmuir-Blodgett Technique"
The 2nd Asian Symposium on Organized Molecular Films for Electronics ad Photonics (ASOMF'2), Beijing (China), November 1-4, 1998
Abstract Book: p. 203

[37] 堀内 祥平、山崎 和彦、八巻 徹也、浅井 圭介、石榑 顕吉
「放射線誘起反応を利用したCdS超微粒子の作製」
第7回東京大学原子力研究総合センターシンポジウム、東京、1998年11月16-17日
UTNST-SMP-7: 印刷中

[38] 堀内 祥平、山崎 和彦、八巻 徹也、浅井 圭介、石榑 顕吉
「低次元半導体の電子物性に対する高エネルギーイオン照射効果」
第7回東京大学原子力研究総合センターシンポジウム、東京、1998年11月16-17日
UTNST-SMP-7: 印刷中

[39]八巻 徹也、浅井 圭介、石榑 顕吉、柴田 裕実
「高エネルギーイオン照射による量子サイズ半導体超微粒子の表面電子状態変化」
第9回粒子線の先端的応用技術に関するシンポジウム、東京、1998年11月25-26日
講演要旨集: p. 159-162